

REPORT  
177

# CRUSTAL AND UPPERMOST MANTLE STRUCTURE OF THE EAST ALBANY–FRASER OROGEN FROM PASSIVE SEISMIC DATA

by C Sippl, H Tkalčić, B Kennett, CV Spaggiari,  
K Gessner, LJ Brisbout, and R Murdie



Australian  
National  
University

ANSIR NATIONAL RESEARCH  
FACILITY FOR  
EARTH SOUNDING



Geological Survey of Western Australia



Government of **Western Australia**  
Department of **Mines, Industry Regulation and Safety**

**REPORT 177**

# **CRUSTAL AND UPPERMOST MANTLE STRUCTURE OF THE EAST ALBANY–FRASER OROGEN FROM PASSIVE SEISMIC DATA**

by

**C Sippl<sup>1</sup>, H Tkalčić<sup>1</sup>, BLN Kennett<sup>1</sup>, CV Spaggiari, K Gessner, LJ Brisbout,  
and R Murdie**

<sup>1</sup> Research School of Earth Sciences, Australian National University, Canberra ACT 2600

**PERTH 2018**



**Geological Survey of  
Western Australia**

**MINISTER FOR MINES AND PETROLEUM**  
**Hon Bill Johnston MLA**

**DIRECTOR GENERAL, DEPARTMENT OF MINES, INDUSTRY REGULATION AND SAFETY**  
**David Smith**

**EXECUTIVE DIRECTOR, GEOLOGICAL SURVEY OF WESTERN AUSTRALIA**  
**Jeff Haworth**

#### **REFERENCE**

**The recommended reference for this publication is:**

Sippl, C, Tkalčić, H, Kennett, B, Spaggiari, CV, Gessner, K, Brisbourn, LJ and Murdie, R 2018, Crustal and uppermost mantle structure of the east Albany–Fraser Orogen from passive seismic data: Geological Survey of Western Australia, Report 177, 51p.

**National Library of Australia Card Number and ISBN 978-1-74168-772-9**



A catalogue record for this book is available from the National Library of Australia

Grid references in this publication refer to the Geocentric Datum of Australia 1994 (GDA94). Locations mentioned in the text are referenced using Map Grid Australia (MGA) coordinates, Zone 51. All locations are quoted to at least the nearest 100 m.



**ANSIR** NATIONAL RESEARCH  
FACILITY FOR  
EARTH SOUNDING

#### **Disclaimer**

This product was produced using information from various sources. The Department of Mines, Industry Regulation and Safety (DMIRS) and the State cannot guarantee the accuracy, currency or completeness of the information. Neither the department nor the State of Western Australia nor any employee or agent of the department shall be responsible or liable for any loss, damage or injury arising from the use of or reliance on any information, data or advice (including incomplete, out of date, incorrect, inaccurate or misleading information, data or advice) expressed or implied in, or coming from, this publication or incorporated into it by reference, by any person whosoever.

**Published 2018 by the Geological Survey of Western Australia**

This Report is published in digital format (PDF) and is available online at <[www.dmp.wa.gov.au/GSWApublications](http://www.dmp.wa.gov.au/GSWApublications)>.



© State of Western Australia (Department of Mines, Industry Regulation and Safety) 2018

With the exception of the Western Australian Coat of Arms and other logos, and where otherwise noted, these data are provided under a Creative Commons Attribution 4.0 International Licence. (<http://creativecommons.org/licenses/by/4.0/legalcode>)

**Further details of geological publications and maps produced by the Geological Survey of Western Australia are available from:**

Information Centre  
Department of Mines, Industry Regulation and Safety  
100 Plain Street  
EAST PERTH WESTERN AUSTRALIA 6004  
Telephone: +61 8 9222 3459 Facsimile: +61 8 9222 3444  
[www.dmp.wa.gov.au/GSWApublications](http://www.dmp.wa.gov.au/GSWApublications)

**Cover photograph:** Photograph of a datalogger of ALFREX seismic station FB08, set up against a tree stump.  
Photo taken by Armando Arcidiaco

# Contents

Abstract .....	1
Introduction .....	1
Regional setting .....	1
Previous geophysical studies .....	3
Data collection .....	6
Methods and processing techniques .....	6
Receiver functions .....	6
Processing — receiver function retrieval .....	6
Methods .....	10
H–K stacking .....	10
Common conversion point stacking .....	10
Interpreting receiver function results .....	14
Autocorrelations .....	14
Ambient noise tomography .....	17
Surface waves and ambient noise .....	17
Processing — determination of group and phase velocities .....	18
Group velocity retrieval .....	18
Phase velocity retrieval .....	18
Methods — tomographic inversion .....	18
Interpreting ambient noise tomography results .....	18
Results .....	20
Crustal thickness and $V_P/V_S$ maps .....	20
CCP profiles .....	23
Upper crustal seismic velocities .....	23
Synthetic tests .....	23
Phase and group velocity maps .....	28
Interpretation .....	28
Craton edge geometry imaged with passive seismic methods .....	28
Gravity forward models .....	36
Upper crustal structure .....	38
Inferences on tectonic processes that formed the Albany–Fraser Orogen .....	39
Subduction zone scenario .....	40
Crustal wedge indentation scenario .....	40
Implications for the tectonic evolution of the Albany–Fraser Orogen .....	41
Geometry of the Fraser Zone and its role in tectonic processes .....	42
Conclusions .....	42
Acknowledgements .....	42
References .....	42

## Appendix

Synthetic tests and raypath coverage plots for ambient noise tomography .....	47
---	----

## Figures

1. Simplified pre-Mesozoic bedrock map of the east Albany–Fraser Orogen .....	2
2. ALFREX station locations on a regional Bouguer gravity anomaly image .....	4
3. ALFREX station locations on an image of total magnetic intensity .....	5
4. Photographs of seismic station setup .....	8
5. Example of a typical $P$ wave receiver function .....	9
6. Distribution of teleseismic events initially used for calculating receiver functions .....	9
7. Comparison of receiver function characteristics for different filtering parameters .....	10
8. Details of receiver functions for the ALFREX array .....	11
9. Examples of H–K stacks from three seismic stations .....	12
10. Schematic sketch illustrating the principle of CCP stacking .....	14
11. Examples of ambient noise autocorrelations from three seismic stations .....	15
12. Aspects of the retrieved receiver function data .....	16
13. Example of an ambient noise spectrum .....	17
14. Seismic tomography using ambient noise as a source .....	19
15. Group and phase velocity sensitivity kernels .....	20
16. Total number of raypaths used for different periods .....	20
17. Summary plot for residual distributions before and after tomographic inversion .....	21
18. Bouguer gravity image of the study area with contoured isolines .....	22
19. Comparison of interpolated Moho depth and $V_P/V_S$ ratios .....	22
20. Inner quartile ranges of handpicked $P_S$ - $P$ times .....	24
21. Crustal thickness map .....	25



22.	Tectonic map showing locations of three CCP profiles .....	26
23.	Three profiles obtained from CCP stacking of receiver functions .....	27
24.	Box and whisker plots of median dispersion curves for the entire ALFREX array .....	29
25.	Group velocity maps for periods of 2–9 s .....	30
26.	Group velocity maps for periods of 10–20 s .....	31
27.	Phase velocity maps for periods of 2–9 s .....	32
28.	Phase velocity maps for periods of 10–20 s .....	33
29.	Moho depth from the interpolated map overlain onto interpreted active seismic profiles .....	34
30.	Three-dimensional view of the Moho trough .....	35
31.	Crustal density forward models along the active seismic and CCP profiles .....	37
32.	Average and selected phase velocity dispersion curves for the ALFREX array .....	39

## Tables

1.	ALFREX stations deployed in phase 1 .....	7
2.	New ALFREX stations deployed in phase 2 .....	8
3.	Crustal thickness and $V_p/V_s$ ratios obtained for all usable seismic stations .....	12

# Crustal and uppermost mantle structure of the east Albany–Fraser Orogen from passive seismic data

by

C Sippl<sup>1</sup>, H Tkalić<sup>1</sup>, B Kennett<sup>1</sup>, CV Spaggiari, K Gessner, LJ Brisboud and R Murdie

## Abstract

A 70-station passive seismic array was deployed in the east Albany–Fraser Orogen from November 2013 to January 2016. Recorded passive seismic data were evaluated using receiver function and ambient noise tomography approaches, yielding maps of crustal thickness and bulk crustal  $V_P/V_S$  ratios, profiles of Moho geometry, and upper crustal surface-wave velocity maps. A belt of significantly thicker crust that follows the northeasterly trend of the east Albany–Fraser Orogen was imaged. The Moho geometry changes from a V-shaped trough in the north of the study area, to a one-sided, discontinuous geometry in the southwest. The maximum crustal thickness near the tip of the V is approximately 50 km, compared to 35–40 km in the eastern Yilgarn Craton to the northwest, and below the eastern Nornalup Zone to the southeast, where the Moho is horizontal. Within the upper crust, the Fraser Zone exhibits elevated  $V_P/V_S$  ratios (~1.8) as well as a prominent high-wavespeed surface-wave velocity anomaly, both indicative of the presence of dense metamorphic rocks overlying the Moho trough in its northern part. The Fraser Zone extends to greater depths near its southern termination, compared to where it has been imaged with active seismic methods to the north. The transition from a more symmetrical Moho trough to a one-sided geometry coincides with the location of the Ida Fault and, together with the presence of dense lower crust defined by the Gunnadorrah Seismic Province, these features can explain the observed gravity pattern. In conjunction with constraints from active seismic and gravity data, these findings imply that the imaged Moho structure could be due to incomplete crustal wedge indentation during a compression event. That event was likely Stage I of the Mesoproterozoic Albany–Fraser Orogeny, triggered by the accretion of the Loongana Arc to the east. The imaged lower crustal geometry may explain the presence and extent of exhumed rocks of mid- to lower-crustal affinity of the Fraser Zone, as well as the westward cessation of voluminous granite intrusions.

**KEYWORDS:** craton margin, passive-source seismology, crustal seismic velocities, Moho

## Introduction

The Albany–Fraser Orogen in Western Australia has long been interpreted to have formed by collision between the West Australian Craton and the Mawson Craton during the Proterozoic (e.g. Myers, 1990, 1993, 1996). More recent investigations, however, have shown that such a collision has not occurred, and that the Albany–Fraser Orogen is better described as a predominantly extensional orogen with a prolonged Proterozoic history including at least one accretionary event (Spaggiari et al., 2015). Since no major tectono-thermal activity has occurred in the Albany–Fraser Orogen after the Mesoproterozoic orogenic events defined as the Albany–Fraser Orogeny, the crustal signatures of these orogenic processes have not been obscured by later overprinting events and are still remarkably well preserved. Thus, the present architecture of the orogen provides direct clues to its formation, which also contributes to the broad understanding of craton margin processes.

This report summarizes the work undertaken and results obtained from the Australian Research Council Linkage Project LP130100413 titled ‘Craton modification and growth: the east Albany–Fraser Orogen in 3D’, a collaborative project between the Australian National University (ANU seismology group) and the Geological

Survey of Western Australia (GSWA). The main objective of the project was to investigate the crustal and uppermost mantle structure of the east Albany–Fraser Orogen by using passive seismic methods, thereby complementing results and interpretations recently obtained from active seismic profiles (Spaggiari and Tyler, 2014). To achieve this the ALFREX (ALbany–FRaser EXperiment) project was established using 70 stations that recorded data in two phases, from November 2013 to January 2016. Although passive seismic methods cannot achieve the fine-scale resolution of seismic reflection profiling, its inherent advantage lies in areal coverage, which can be used to investigate the orogen in all three dimensions, providing information, for example, about along-strike changes in structure that 2D profiles cannot capture. Moreover, passive seismic data can resolve parameters such as absolute  $V_s$  or  $V_P/V_S$  ( $S$ - and  $P$ -wave velocities and their ratios), which cannot be obtained from standard active seismic methods.

## Regional setting

The Albany–Fraser Orogen (AFO), a region of extensive reworking of Yilgarn Craton crust during the Paleo- and Mesoproterozoic (Kirkland et al., 2011; Spaggiari et al., 2014a,b, 2015), defines the southern to southeastern margin of the Archean Yilgarn Craton, which is part of the West Australian Craton (Fig. 1). Regional Paleoproterozoic tectonism during 1815–1480 Ma was dominated by extension within a continental rift setting that led to

<sup>1</sup> Research School of Earth Sciences, Australian National University, Canberra ACT 2600

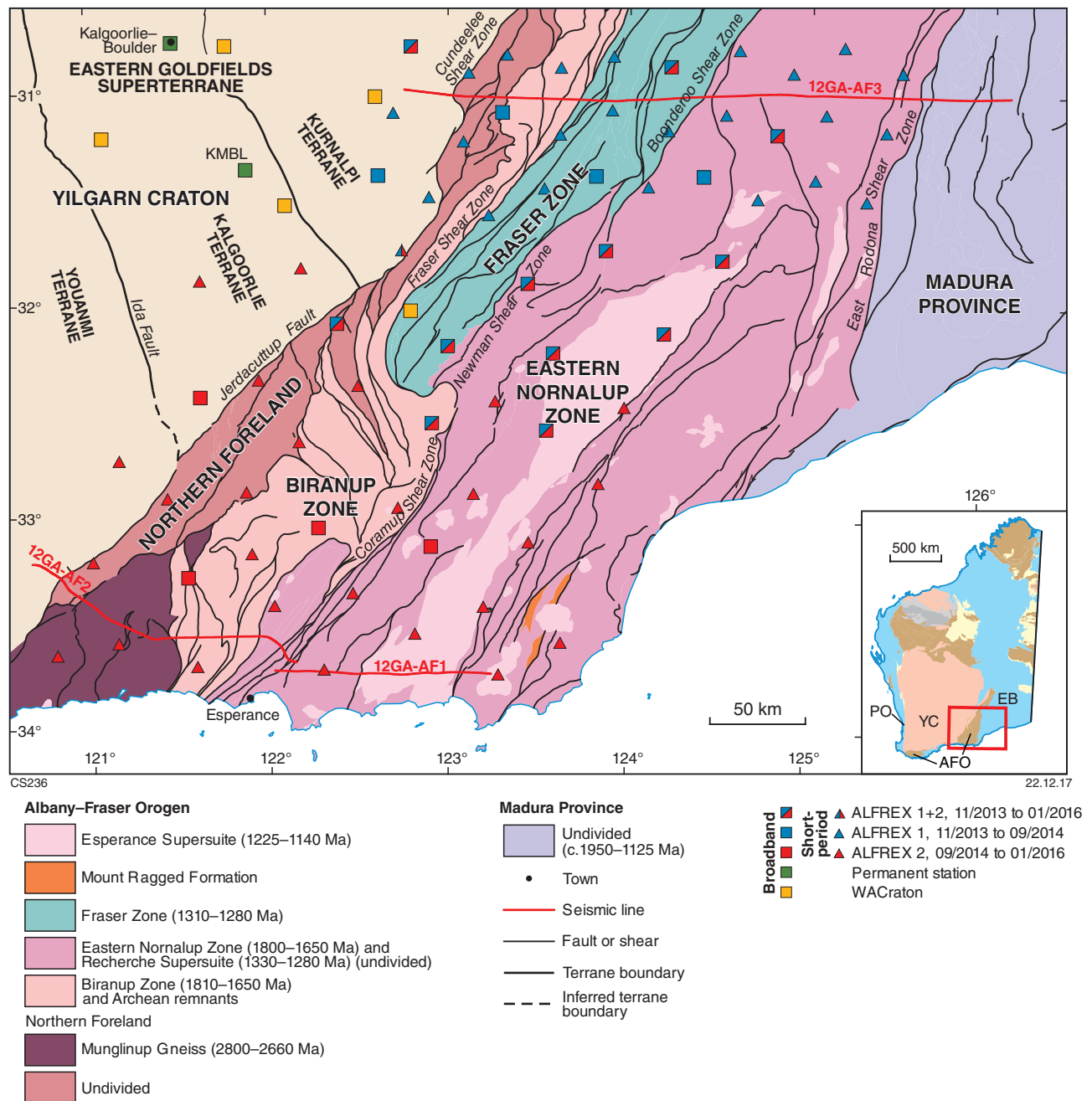


**Figure 1.** Simplified pre-Mesozoic bedrock map of the east Albany–Fraser Orogen (modified from Spaggiari, 2016) showing locations of ALFEX seismic stations (red and blue symbols), and other seismic stations (green and orange symbols) used in this study. The three active seismic lines shot in 2012 are shown as red lines. The inset is a simplified geological map of Western Australia, showing Archean basement (pink), Proterozoic orogens (brown), and Proterozoic and younger basins (yellow and blue, respectively). Abbreviations: AFO, Albany–Fraser Orogen; EB, Eucla Basin; PO, Pinjarra Orogen; YC, Yilgarn Craton

the formation of an ocean–continent transition, with the craton edge as a passive margin (Spaggiari et al., 2014c, 2015; Spaggiari and Smithies, 2015). During the Mesoproterozoic, two distinct tectono-thermal stages are defined as the Albany–Fraser Orogeny (Clark et al., 2000; Spaggiari et al., 2014a; Smithies et al., 2015): Stage I, between 1330 and 1280 Ma, is interpreted to have been triggered by the accretion of an oceanic arc (the Loongana Arc) to the east (Spaggiari et al., 2015), whereas Stage II is generally interpreted as an intracratonic reactivation and voluminous magmatic event.

The AFO is separated from the adjacent Madura Province to the east by the Rodona Shear Zone, which represents the suture between modified Archean Yilgarn crust and exotic (oceanic and oceanic-arc type) basement rocks under cover. To the west, it is truncated by the Darling Fault and the Meso- to Neoproterozoic Pinjarra Orogen. The AFO is interpreted to be continuous into the Wilkes Land region of eastern Antarctica (Fitzsimons, 2003, and references therein; Aitken et al., 2016; Morrissey et al., 2017).

Internally, the northeasterly trending belt of the east AFO is subdivided into the Northern Foreland and the Kepa Kurl Booya Province (Fig. 1; Spaggiari et al., 2014a). The former is less modified Archean Yilgarn Craton, and forms a narrow sliver along most of the interface between the Yilgarn Craton and the Kepa Kurl Booya Province. Major structures separating the Northern Foreland from un-reworked Yilgarn Craton are the Jerdacuttup Fault and the Cundeelee Shear Zone (Spaggiari et al., 2014c).

The Kepa Kurl Booya Province is subdivided into the Biranup, Nornalup, Fraser and Tropicana Zones, the last of which lies to the north outside our study area. The Biranup Zone, located directly southeast of the Northern Foreland, is dominated by deformed orthogneisses with ages between c. 1810 and 1625 Ma, and includes Archean granitic rocks with Yilgarn Craton affinity (Kirkland et al., 2011; Spaggiari et al., 2014a; Smithies et al., 2015). The Fraser Zone, an approximately 450 km long, northeasterly trending belt of high-density, metagabbroic granulite-facies rocks that does not extend along the entire east AFO, lies between the Biranup and the eastern Nornalup Zone. The Fraser Zone is bound to the west and south by the Fraser Shear Zone, and to the east by the Boonderoo and Newman Shear Zones (Fig. 1). Metagabbroic rocks interlayered with granitic and sedimentary gneisses of the Fraser Zone formed between c. 1310 and 1280 Ma and were exhumed from mid-crustal depths during Stage I of the Albany–Fraser Orogeny (Clark et al., 2014; Kirkland et al., 2014; Spaggiari et al., 2014a; Maier et al., 2016). The basement lithologies of the eastern Nornalup and Biranup Zones are similar, but they are separated by a major shear zone network that contains the Coramup Shear Zone, and the Fraser Zone itself (Spaggiari et al., 2014c). The eastern Nornalup Zone has been extensively intruded by the granitic and gabbroic rocks of the 1330–1280 Ma Recherche Supersuite and the 1200–1140 Ma Esperance Supersuite (Smithies et al., 2015). The northeastern part of the eastern Nornalup Zone is covered by Cretaceous

shale and siltstone of the Madura Formation and Eocene limestone successions of the Eucla Basin (Lowry, 1970).

## Previous geophysical studies

Significant progress has been made in recent years in mapping the upper crustal geology of the east AFO, although linking this to middle and lower crustal levels remains ambiguous. Most of the current knowledge about the deep crustal architecture of the orogen comes from four active seismic reflection profiles (12GA-AF1, 12GA-AF2, 12GA-AF3, 12GA-T1) that were shot in 2012 in a collaborative project between GSWA, Geoscience Australia, AuScope, and AngloGold Ashanti Ltd (Spaggiari and Tyler, 2014). These profiles make up two east–west cross-sections through the central (12GA-AF3) and southern (12GA-AF1 and 12GA-AF2) parts of the east AFO (Fig. 1). The ALFREX passive seismic array was designed to fill the space between the two east–west transects. To the northeast, outside the study area, a shorter seismic reflection profile was acquired in the Tropicana Zone (12GA-T1).

The other main geophysical observables available for the study area are potential field datasets of Bouguer gravity and total magnetic intensity (Figs 2, 3). Although the aeromagnetic datasets are typically dominated by shallow to very shallow features, the Bouguer gravity data contain information about the entire crust, and possibly even below that, and are therefore considered more useful for this project. The gravity map of the east AFO shows a distinct pair of parallel anomalies of high amplitude that follow the northeasterly trend of the orogen. The eastern anomaly is a gravity high that is clearly associated with the dominantly mafic metamorphic rocks of the Fraser Zone, and consequently disappears at the southwestern termination of the Fraser Zone. Directly west of this gravity high, the Rason Regional Gravity Low (Fraser and Pettifer, 1980) forms an along-strike continuous, prominent low-gravity signal that also fades out towards the southwest of the study area, but extends somewhat beyond the termination of the adjacent gravity high (Fig. 2). Farther southwest, close to the coastline, a gravity high replaces the Rason Regional Gravity Low. These gravity features, as well as depth constraints, are discussed in more detail below (see **Gravity forward models**).

In a recent study, peaks in the resonance spectrum of passive seismic sensors across the Eucla Basin have been used to derive depths to basement (Scheib et al., 2016). Calibrating the results obtained with ground truth information from drilling programs, the authors obtained cover thicknesses between 0 and 600 m, with the thickest basin cover located to the east of our study area. In the region of the ALFREX deployment, which was only marginally affected by the presence of Eucla Basin successions in its northeasternmost part, cover thickness reaches a maximum of about 300 m.



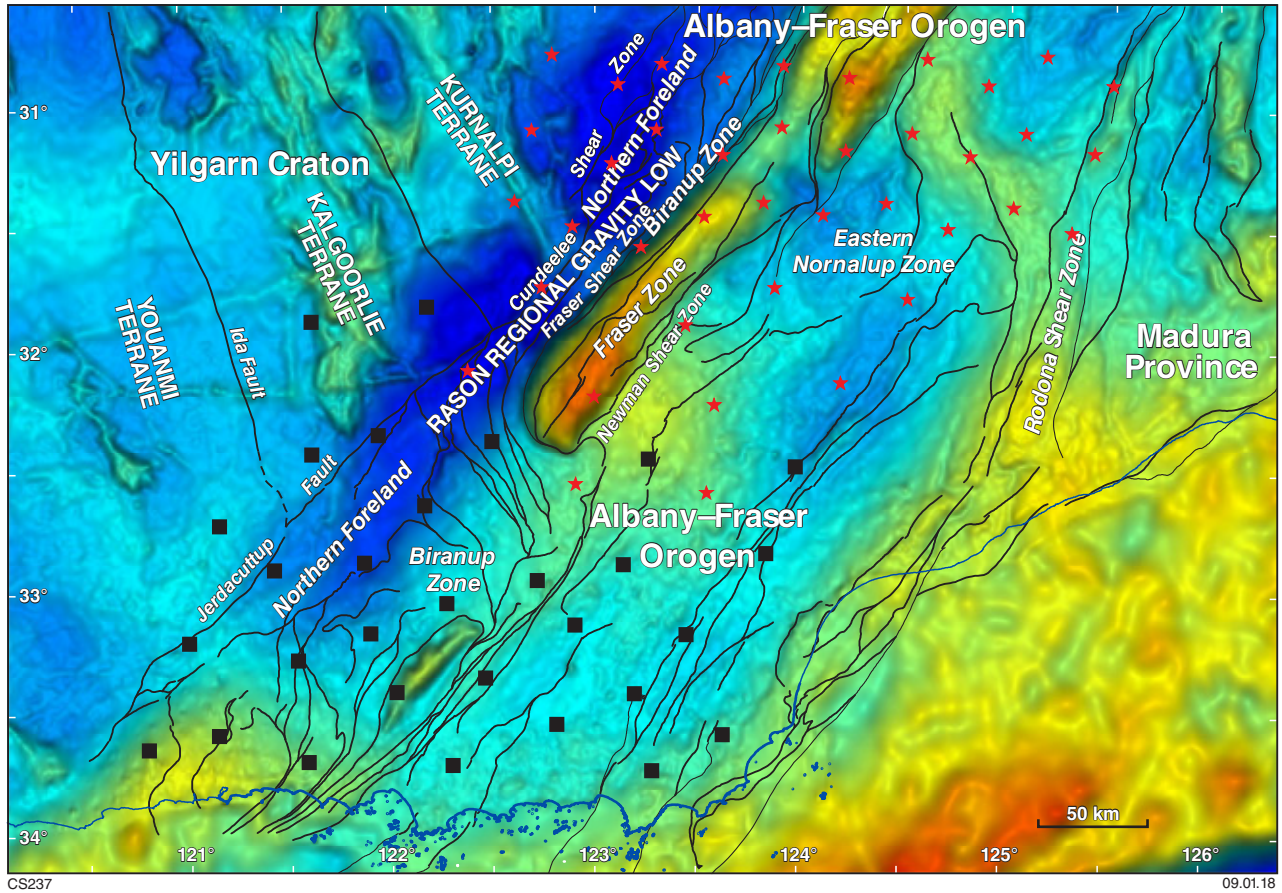


**Figure 2.** ALFREX station locations on a regional Bouguer gravity anomaly image. Red and blue denote positive and negative gravity anomaly values, respectively. Greenstone belts of the Yilgarn Craton are defined as northwesterly trending, moderate to strong gravity anomalies. Stations installed in ALFREX phase 1 are shown as red stars and those of phase 2 as black squares. Major faults and shear zones are marked as black lines (from Fig. 1). The coastline is shown as a blue line. A simplified gravity anomaly map showing actual physical units and contoured gravity isolines is provided in Figure 18



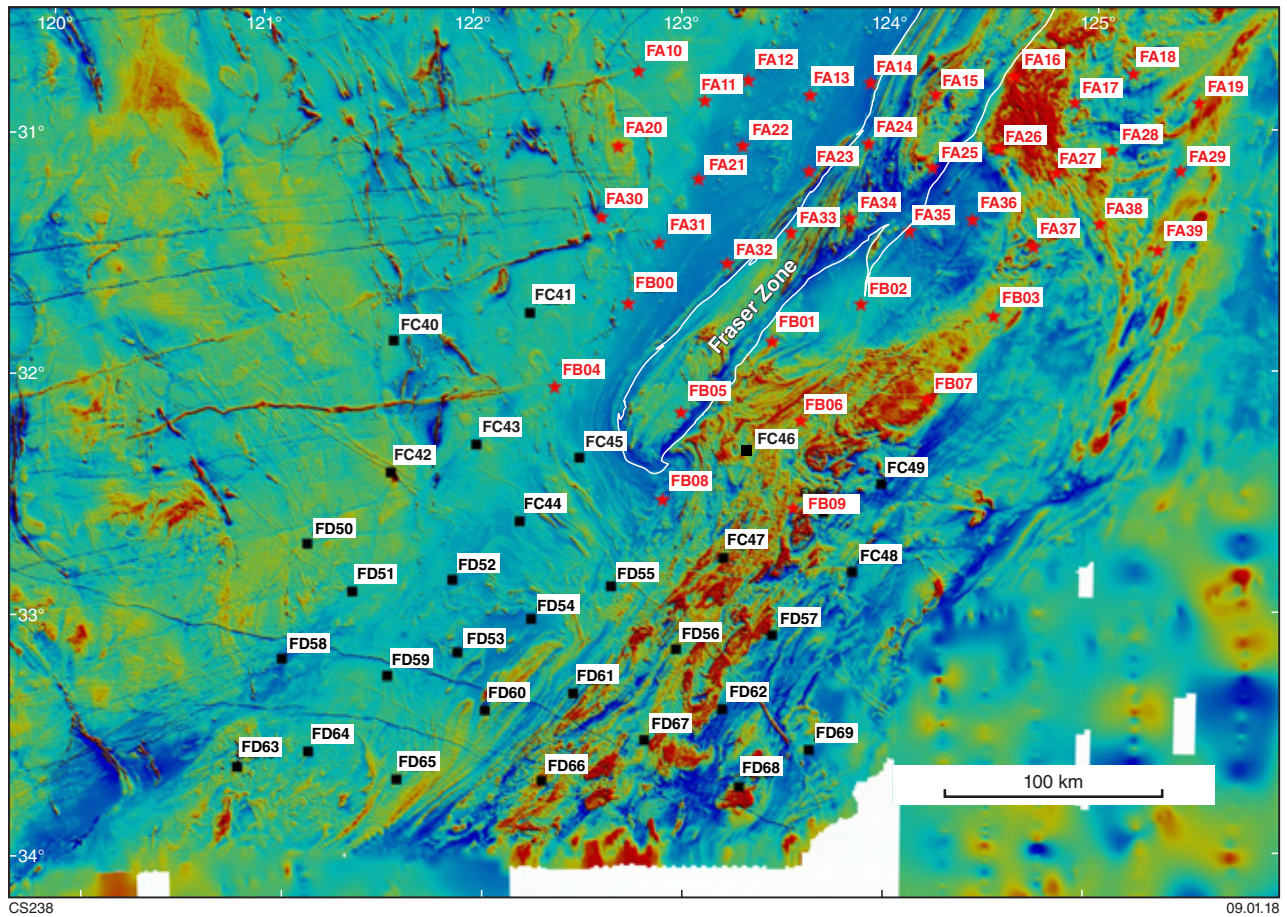


Figure 3. ALFREX station locations (red stars, phase 1; black squares, phase 2) and their names on an image of total magnetic intensity. For structural detail refer to Figure 2 and Spaggiari (2016)

## Data collection

Seismic recording kits were deployed throughout the study area in two phases (Tables 1, 2). In phase 1, in November 2013, 40 stations were deployed in the northern part of the study area. Phase 2 was initiated in October 2014, and 27 of these stations were moved to the southern part of the study area and three additional stations were deployed (Fig. 1).

Each ALFLEX site consisted of a seismometer (either Lennartz 3D-lite or Trillium Compact) that was buried underground to a depth of about 0.5 m, and an ANU seismic recording unit that was left above ground, but wrapped into sturdy tarps to protect it from rainfall and animals (Fig. 4). To ensure precise timing, a small GPS antenna mounted on a nearby tree or on the recorder itself was connected to the datalogger. The ALFLEX array (Sippl et al., 2015) was designed to extend across all of the northeasterly trending tectono-stratigraphic units that make up the east AFO with a roughly uniform station spacing of about 40 km, which was achievable where access permitted (Fig. 1). A denser corridor of stations was deployed along the line of the active seismic profile 12GA-AF3 to allow for calibration of the passive seismic results by comparison with the active seismic reflection images.

Passive seismic data were recorded with a sampling frequency of 50 Hz onto SD cards in the dataloggers. Because the stations were operated on battery power, service trips about every 3.5 months were necessary to exchange and recharge batteries and retrieve the recorded data. These trips were also used for maintenance work if a station had stopped recording or if there were problems with data quality.

## Methods and processing techniques

As for most of the Australian continent, the study area is currently not highly seismically active, so local earthquakes were not available as seismic sources for the determination of the regional crustal structure. Thus, teleseismic signals from distant earthquakes and the constant background reverberations caused by the interaction of land and ocean were used. Because these techniques, which are well known in the passive-source seismology community, are generally less well known in the broader geoscience community, detailed explanations of their principles and short summaries of their strengths and limitations are provided.

### Receiver functions

The receiver function technique makes use of the fact that seismic waves are not only reflected and/or refracted at subsurface wavespeed discontinuities, but that a fraction of their energy is also converted to a different wave type, from  $P$  to  $S$ , or from  $S$  to  $P$  (Fig. 5). Because the motion of  $S$  waves occur in a plane that is perpendicular to the plane of motion of  $P$  waves, it is possible to isolate (and discriminate) them by a coordination transformation

into the ZRT system, i.e. using the horizontal directions along (radial – R) and perpendicular to (transverse – T) the raypath, instead of north–south and east–west directions. This coordinate transformation, together with a process called deconvolution, which removes source and propagation path effects from the waveforms by (spectrally) subtracting the vertical waveform from the horizontal traces, is used to construct the receiver function (Vinnik, 1977; Langston, 1979; Ammon, 1991). A typical example of a radial component  $P$  wave receiver function is shown in Figure 5. Each wave arrival produces a distinct spike, the width of which is dependent on the sharpness of the velocity contrast in the subsurface.

The primary conversion phase from the Moho, called  $P_s$ , arrives after the direct  $P$  pulse, since  $S$  waves travel more slowly than  $P$  waves. The time separation between direct  $P$  and  $P_s$  depends on the depth of the discontinuity (here crustal thickness) as well as on the  $V_p/V_s$  ratio (see **H–K stacking**). Later arriving phases can be due to crustal multiples (shown schematically in Fig. 5) or from deeper discontinuities. Likewise, strong intracrustal velocity discontinuities can also create a set of corresponding phases ( $P_s$ , multiples) at earlier arrival times compared to the Moho-related arrivals ( $P_m$ ).

A fundamental assumption that is made when analysing receiver functions is that layering in the subsurface is horizontal. Most receiver function methods use stacks of many teleseismic arrivals at one seismic station for receiver function retrieval. Because all of these arrivals originate from different earthquakes at different global locations, their raypaths near the seismic stations are different, i.e. they penetrate the Moho or other discontinuities at different locations. Thus, most receiver function analyses represent averages over a cone in space that widens with depth.

### Processing — receiver function retrieval

We first retrieved a global catalogue of large earthquakes (magnitude  $>5.5$ ) that occurred during the time the array was operating and extracted from it data segments containing the  $P$  arrival for all events that fell within the distance range  $30^\circ$  to  $95^\circ$  (Fig. 6). The horizontal traces of these events are then rotated into the ZRT coordinate system (see above), and deconvolved using an iterative time-domain approach (Ligorria and Ammon, 1999). Within the deconvolution algorithm, a Gaussian filter was applied to limit the bandwidth of the resulting receiver functions. Because the main objective of the study was to illuminate the crust and uppermost mantle, we chose a rather short-period Gaussian filter parameter of  $a = 2.5$ , which is well suited to image structures in this depth range, but performs worse than longer period filters for deeper discontinuities (Fig. 7).

All retrieved receiver functions were automatically pre-selected by convolving the radial receiver function with the Z component of the data and comparing the result to the actual R waveform. For a good receiver function, the achieved fit should be 90% or better; we thus discarded all traces that produced a fit of less than 85%. In a second step, all receiver functions were checked visually and traces considered to be too noisy were discarded.

**Table 1. ALFREX stations deployed in phase 1**

<i>Station name<sup>(a)</sup></i>	<i>Sensor type<sup>(b)</sup></i>	<i>Lat (°)</i>	<i>Long (°)</i>	<i>Elevation (m)</i>	<i>Period of operation</i>
FA10*	Trillium Compact (BB)	–30.78730	122.79515	349	06/11/2013–18/12/2015
FA11	Lennartz 3Dlite (SP)	–30.91068	123.11295	377	08/11/2013–19/06/2014
FA12	Lennartz 3Dlite (SP)	–30.82537	123.32329	375	08/11/2013–10/10/2014
FA13	Lennartz 3Dlite (SP)	–30.88637	123.62059	270	09/11/2013–03/09/2014
FA14	Lennartz 3Dlite (SP)	–30.83259	123.91017	272	17/11/2013–11/10/2014
FA15*	Trillium Compact (BB)	–30.87924	124.22452	209	16/11/2013–26/12/2015
FA16	Lennartz 3Dlite (SP)	–30.79964	124.59934	192	15/11/2013–11/10/2014
FA17	Lennartz 3Dlite (SP)	–30.90593	124.89545	190	15/11/2013–01/09/2014
FA18	Lennartz 3Dlite (SP)	–30.78173	125.17411	190	14/11/2013–10/10/2014
FA19	Lennartz 3Dlite (SP)	–30.89797	125.49374	185	15/11/2013–10/10/2014
FA20	Lennartz 3Dlite (SP)	–31.10069	122.69717	315	07/11/2013–08/10/2014
FA21	Lennartz 3Dlite (SP)	–31.23685	123.08333	266	08/11/2013–20/06/2014
FA22	Trillium Compact (BB)	–31.09847	123.29749	291	08/11/2013–03/09/2014
FA23	Lennartz 3Dlite (SP)	–31.20256	123.61760	229	09/11/2013–11/10/2014
FA24	Lennartz 3Dlite (SP)	–31.08654	123.90257	247	09/11/2014–10/10/2014
FA25	Lennartz 3Dlite (SP)	–31.18328	124.21138	157	16/11/2013–15/09/2014
FA26	Lennartz 3Dlite (SP)	–31.10626	124.52934	176	16/11/2013–09/10/2014
FA27*	Trillium Compact (BB)	–31.19939	124.81074	176	15/11/2013–29/11/2015
FA28	Lennartz 3Dlite (SP)	–31.10220	125.07824	173	15/11/2013–11/10/2014
FA29	Lennartz 3Dlite (SP)	–31.18085	125.41021	165	14/11/2013–24/09/2014
FA30	Trillium Compact (BB)	–31.39572	122.61315	287	07/11/2013–25/09/2014
FA31	Lennartz 3Dlite (SP)	–31.49796	122.89263	284	07/11/2013–09/10/2014
FA32	Lennartz 3Dlite (SP)	–31.58405	123.22395	304	10/11/2013–12/10/2014
FA33	Lennartz 3Dlite (SP)	–31.45780	123.53100	265	10/11/2013–12/10/2014
FA34	Trillium Compact (BB)	–31.39780	123.81655	205	09/11/2014–11/09/2014
FA35	Lennartz 3Dlite (SP)	–31.44826	124.10362	171	16/11/2013–09/10/2014
FA36	Trillium Compact (BB)	–31.39832	124.40873	154	16/11/2013–09/10/2014
FA37	Lennartz 3Dlite (SP)	–31.50306	124.70716	168	14/11/2013–11/10/2014
FA38	Lennartz 3Dlite (SP)	–31.40955	125.02450	156	15/11/2013–11/10/2014
FA39	Lennartz 3Dlite (SP)	–31.50914	125.30928	126	14/11/2013–10/10/2014
FB00*	Lennartz 3Dlite (SP)	–31.75010	122.74270	312	12/11/2013–13/01/2016
FB01*	Trillium Compact (BB)	–31.90722	123.44156	201	12/11/2013–27/12/2015
FB02*	Trillium Compact (BB)	–31.75068	123.87299	159	11/11/2013–29/12/2015
FB03*	Trillium Compact (BB)	–31.79418	124.51704	141	13/11/2013–14/12/2015
FB04*	Trillium Compact (BB)	–32.09641	122.38266	353	10/11/2013–30/12/2015
FB05*	Trillium Compact (BB)	–32.20242	122.99788	252	12/11/2013–10/12/2015
FB06*	Trillium Compact (BB)	–32.23617	123.58321	192	11/11/2013–30/12/2015
FB07*	Trillium Compact (BB)	–32.14236	124.19761	136	13/11/2013–12/12/2015
FB08*	Trillium Compact (BB)	–32.56565	122.90781	253	12/11/2013–09/12/2015
FB09*	Trillium Compact (BB)	–32.60013	123.54704	159	11/11/2013–12/12/2015

**NOTES:** (a) Stations that also operated during phase 2 are marked with an asterisk  
(b) BB, broadband; SP, short period



**Table 2. New ALFEX stations deployed in phase 2**

Station name	Sensor type <sup>(a)</sup>	Lat (°)	Long (°)	Elevation (m)	Period of operation
FC40	Lennartz 3Dlite (SP)	−31.89020	121.62320	337	14/10/2014–14/01/2016
FC41	Lennartz 3Dlite (SP)	−31.83229	122.18470	328	11/02/2015–14/01/2016
FC42	Trillium Compact (BB)	−32.44056	121.61932	282	14/10/2014–15/08/2015
FC43	Lennartz 3Dlite (SP)	−32.36202	121.94400	301	17/10/2014–13/01/2016
FC44	Lennartz 3Dlite (SP)	−32.65427	122.16816	201	16/10/2014–09/06/2015
FC45	Lennartz 3Dlite (SP)	−32.39024	122.49789	301	17/10/2014–13/01/2016
FC46	Lennartz 3Dlite (SP)	−32.46453	123.26135	210	07/02/2015–12/09/2015
FC47	Lennartz 3Dlite (SP)	−32.90163	123.14108	188	07/02/2015–04/01/2016
FC48	Lennartz 3Dlite (SP)	−32.85240	123.83847	161	07/02/2015–18/01/2016
FC49	Lennartz 3Dlite (SP)	−32.49238	123.98003	130	12/02/2015–01/01/2016
FD50	Lennartz 3Dlite (SP)	−32.73706	121.16190	253	17/10/2014–14/12/2015
FD51	Lennartz 3Dlite (SP)	−32.91770	121.42920	237	16/10/2014–13/01/2016
FD52	Lennartz 3Dlite (SP)	−32.89060	121.87020	233	17/10/2014–14/01/2016
FD53	Lennartz 3Dlite (SP)	−33.18230	121.89800	211	16/10/2014–01/01/2016
FD54	Trillium Compact (BB)	−33.05920	122.27341	263	16/10/2014–17/12/2015
FD55	Lennartz 3Dlite (SP)	−32.96689	122.71786	241	04/02/2015–03/01/2016
FD56	Trillium Compact (BB)	−33.14964	122.90257	207	15/10/2014–22/12/2015
FD57	Lennartz 3Dlite (SP)	−33.13003	123.44891	148	06/02/2015–25/05/2015
FD58	Lennartz 3Dlite (SP)	−33.21350	121.00660	220	16/10/2014–15/01/2016
FD59	Trillium Compact (BB)	−33.29090	121.53960	179	16/10/2014–23/05/2015
FD60	Lennartz 3Dlite (SP)	−33.42680	122.02370	168	15/10/2014–15/01/2016
FD61	Lennartz 3Dlite (SP)	−33.36900	122.46420	212	15/10/2014–17/01/2016
FD62	Lennartz 3Dlite (SP)	−33.43472	123.19717	117	15/10/2014–17/01/2016
FD63	Lennartz 3Dlite (SP)	−33.65110	120.79654	149	09/02/2015–16/01/2016
FD64	Lennartz 3Dlite (SP)	−33.59851	121.14342	125	09/02/2015–12/01/2016
FD65	Lennartz 3Dlite (SP)	−33.71188	121.58604	62	09/02/2015–08/01/2016
FD66	Lennartz 3Dlite (SP)	−33.73030	122.29900	101	15/10/2014–11/12/2015
FD67	Lennartz 3Dlite (SP)	−33.56130	122.81270	143	15/10/2014–10/09/2015
FD68	Lennartz 3Dlite (SP)	−33.75409	123.28192	94	06/02/2015–11/09/2015
FD69	Lennartz 3Dlite (SP)	−33.60278	123.63065	115	06/02/2015–14/01/2016

**NOTE:** (a) BB, broadband; SP, short period

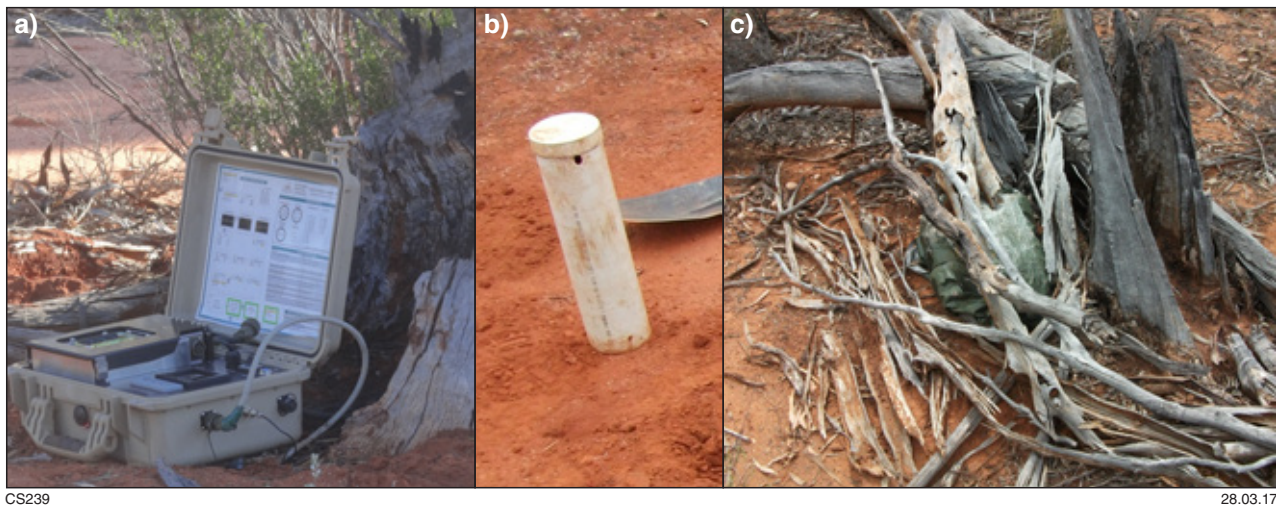


**Figure 4.** Photographs of a typical seismic station setup: a) datalogger containing a battery pack. This unit is connected to the buried seismometer (thick cable) and to a GPS antenna for timing (thin black cable). The datalogger was not buried so that it could be easily accessed during service trips for battery exchange and data retrieval; b) plastic tube used to protect buried seismometers (short-period sensor at this station); c) typical installation in the field. Dataloggers were wrapped in green tarps to protect them from moisture; branches were placed around them to hide them from view and to keep animals away

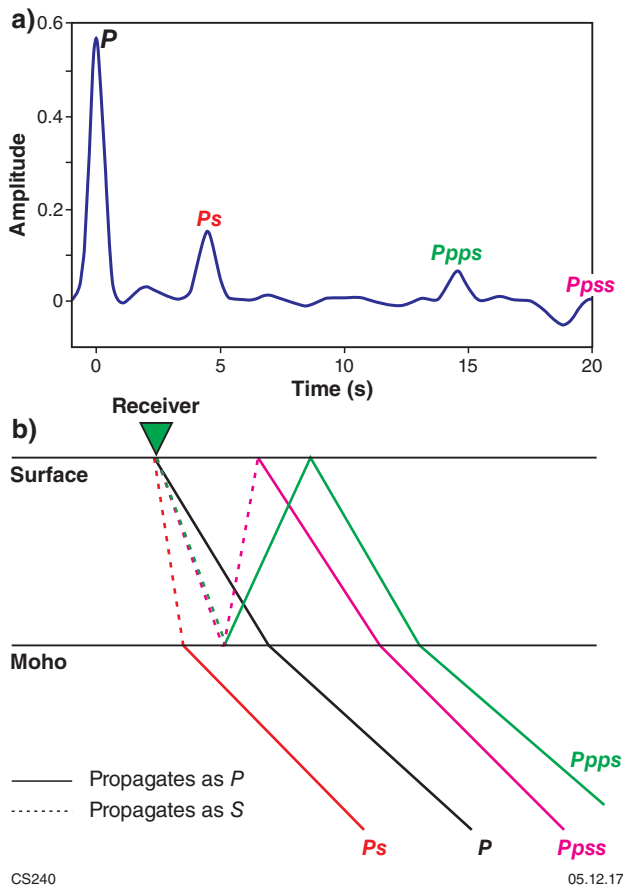


Figure 5. Example of a typical *P* wave receiver function and schematic raypath diagram: a) typical *P* wave receiver function (radial trace; real data example). The different phases, *P* (direct wave), *Ps* (*P*-to-*S* conversion at Moho), and the multiples (*Ppps* and *Ppss*) are clearly visible; b) schematic diagram showing approximate raypaths for the different phases. Distances traversed as *S* phase (dotted lines) cause time delays because the *S* wavespeed is always significantly slower than *P* wavespeed. Reflections (without wave-type conversion) from a faster medium incur a phase change of 180°, which explains the negative sign of the *Ppss* phase. *Ppps* is reflected off the free surface (slower medium), and hence does not switch sign

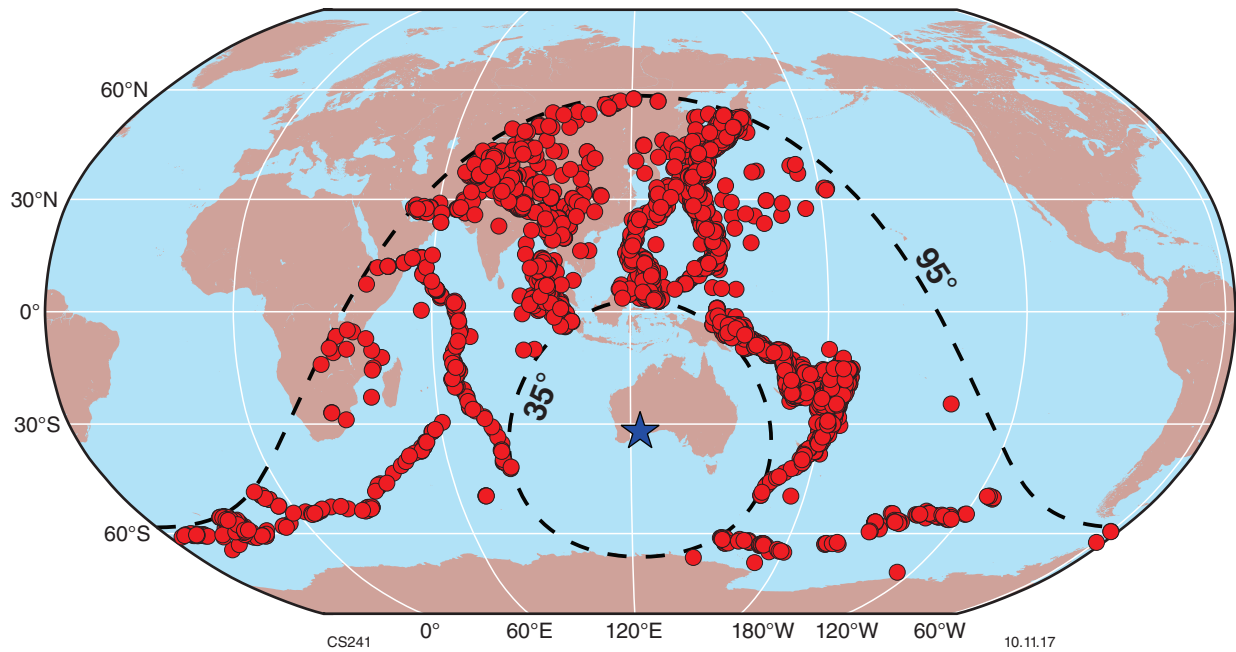
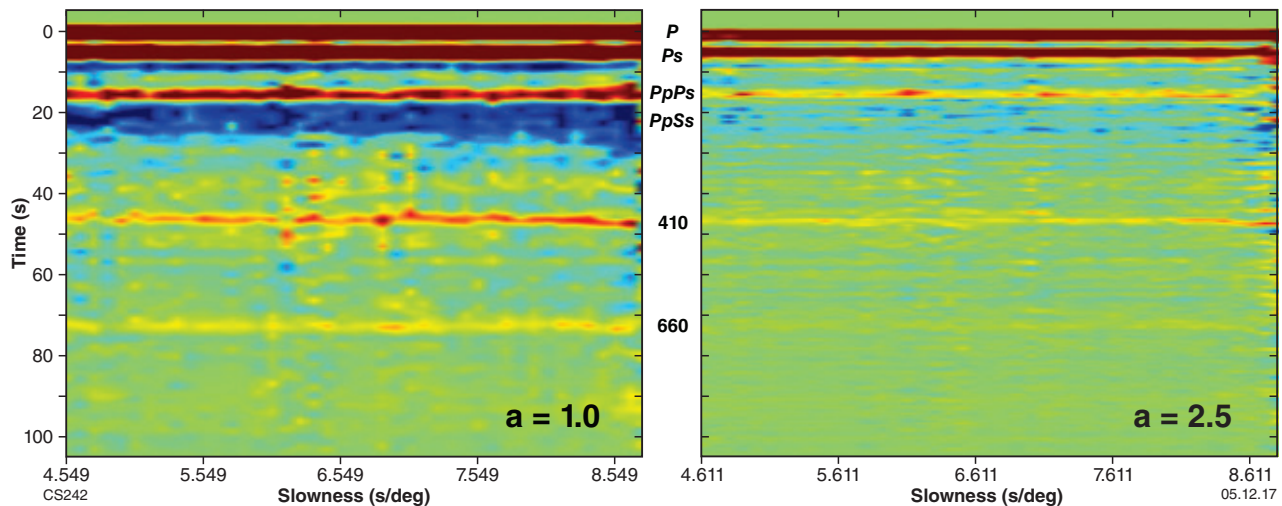


Figure 6. Distribution of teleseismic events that were initially used to calculate receiver functions in this study (red dots). The blue star marks the centre of the ALFREX array, which was used to calculate source–receiver distances. Receiver functions from all these events were subjected to automatic and visual selection processes, with the implication that not all of the earthquakes shown were used in the final model





**Figure 7.** Comparison of receiver function characteristics for different filtering parameters. In both images, all selected receiver functions for the entire ALFLEX network are plotted as binned and normalized stacks against the raypath parameter (equivalent to the distance of the earthquake in a horizontally layered earth). The positions of incoming phases are indicated in the centre, between the two panels. It is clear that although the higher-frequency receiver functions (right panel) provide sharper direct  $P$  and  $P_s$  peaks, they are less well suited to resolve deeper structure (e.g. the phase associated with conversion at the 660 horizon is nearly invisible for higher frequency receiver functions). Because this plot samples receiver functions from the entire network, more subtle features, such as moveout with raypath parameter, are not evident due to scatter in the phases between different stations

Figure 8 shows a compilation of all retrieved receiver functions from ALFLEX stations, stacked using an approach that searches for groups of coherent traces in the data (Tkalčić et al., 2011).

## Methods

### H–K stacking

A set of receiver functions from one seismic station can be used to determine the crustal thickness and the bulk crustal  $V_p/V_s$  ratio beneath that station with a grid search approach called H–K stacking (Chevrot and Van der Hilst, 2000; Zhu and Kanamori, 2000). As mentioned above, the time separation between direct  $P$  pulse and  $P_s$  phase alone can be used as a proxy for crustal thickness. However, since this property also depends on  $V_p/V_s$  ratio, different combinations of crustal thickness and  $V_p/V_s$  can lead to the same time difference (i.e. non-uniqueness). This conundrum can be solved by including the crustal multiples into the analysis. The H–K stacking approach isolates time windows and stacks phase amplitudes for  $P_s$  as well as the two types of crustal multiples (Fig. 5) for different combinations of  $V_p/V_s$  and crustal thickness. Only in the vicinity of the correct values will all three phases be encountered in their correct time windows; thus stacked amplitudes will be maximal. A prerequisite for the application of this method is the knowledge of an adequate  $V_p$  velocity model for the immediate vicinity of the investigated station.

The algorithm of Chen et al. (2010) was applied, allowing the crustal thickness to vary between 25 and 65 km in increments of 0.1 km, and  $V_p/V_s$  between 1.6 and 1.9 in increments of 0.005. The average crustal  $P$  wave velocity

from the nearest node of the Australian Seismological Reference (AusREM) velocity model (Salmon et al., 2013) was used for  $V_p$  for each station. Amplitudes of all three phases ( $P_s$ ,  $PpSs$ ,  $PpPs$ ) were weighted equally. Three examples of the resulting H–K stacking are shown in Figure 9, and results from this approach are summarized in Table 3. For the few cases where stations showed multiple maxima (such as station FA23 in Fig. 9), we selected the one that was most consistent with adjacent stations. In all of these cases, the double maximum occurred along a single  $P_s$  strand, i.e. representing different solutions because of uncertainty in the multiples, not different  $P_s$  phases that might indicate a ‘double Moho’.

### Common conversion point stacking

Another approach is to use receiver functions for direct imaging purposes. A popular technique is common conversion point (CCP) stacking (Dueker and Sheehan, 1997), where the amplitudes of receiver functions are added into bins along their raypaths (Fig. 10). This technique yields an actual image of structures in the subsurface that does not rely on interpolation or the assumption of horizontal layering. However, to convert from time to depth, an assumption of the background velocity model needs to be made. For the AFO, we divided the subsurface into  $2 \times 2$  km bins down to 200 km depth along three profile lines and used a modified version of the global velocity model ak135 (Kennett et al., 1995) for the depth conversions. Since the crustal velocities in this model most likely underestimate the values of the AFO, the retrieved absolute depths may be exaggerated by up to 5 km. However, this exaggeration should be consistent for closely located stations, which means that it does not affect the imaged geometries, just their depth placement.

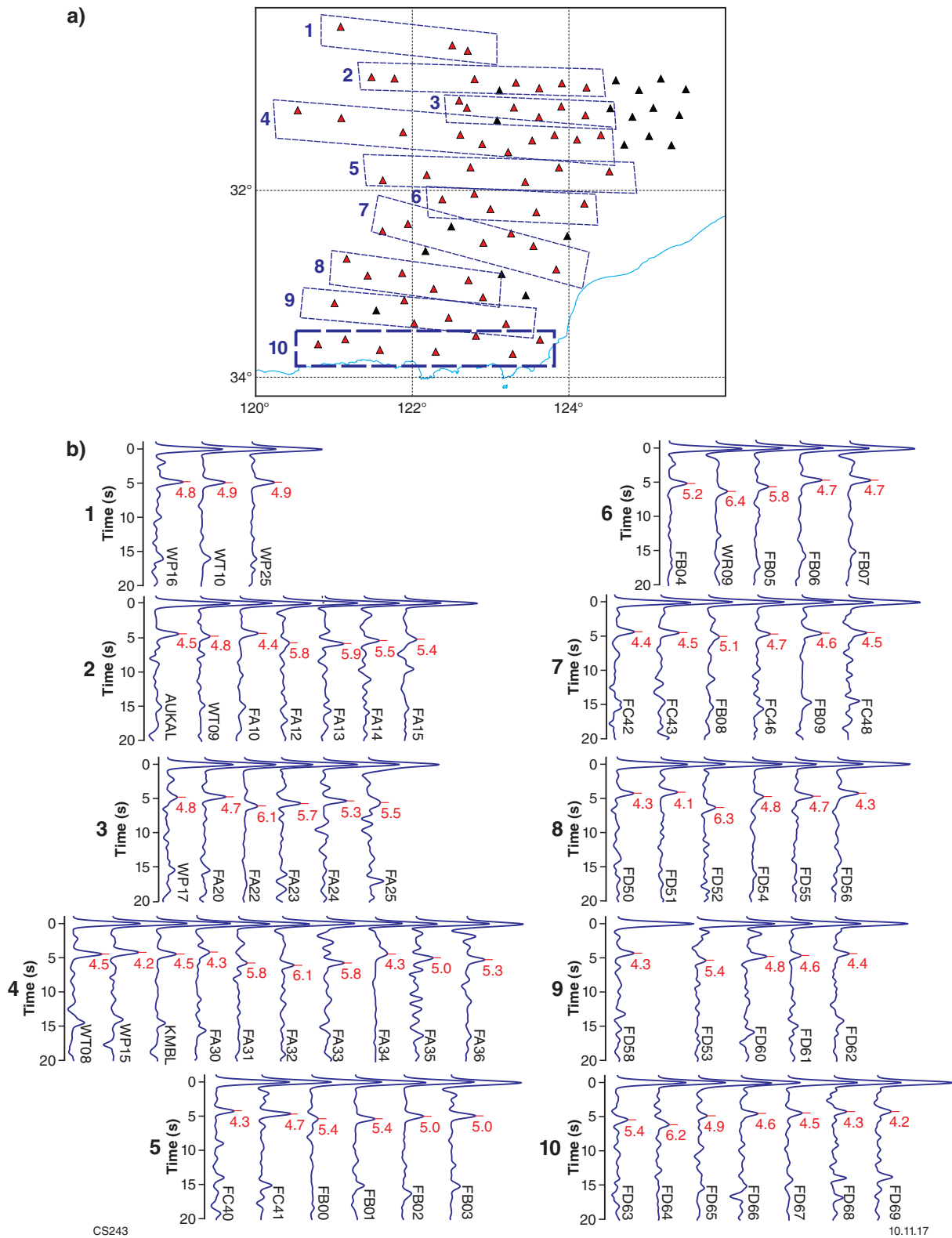


**Figure 8.** Details of receiver functions for the ALFREX array: a) map showing ALFREX stations that yielded usable data (red triangles) and unusable data (black triangles). The coastline is also shown (blue line). The stations were divided into ten roughly east–west profiles; b) averaged receiver functions for the ten profiles after application of a coherency criterion according to Tkalčić et al. (2011). For each receiver function, the  $P_s$  peak is marked with a red bar and the associated  $P_s$ – $P$  time is annotated. Even in this raw data, a trend of systematically longer  $P_s$ – $P$  times is discernible towards the centre of most of the profiles

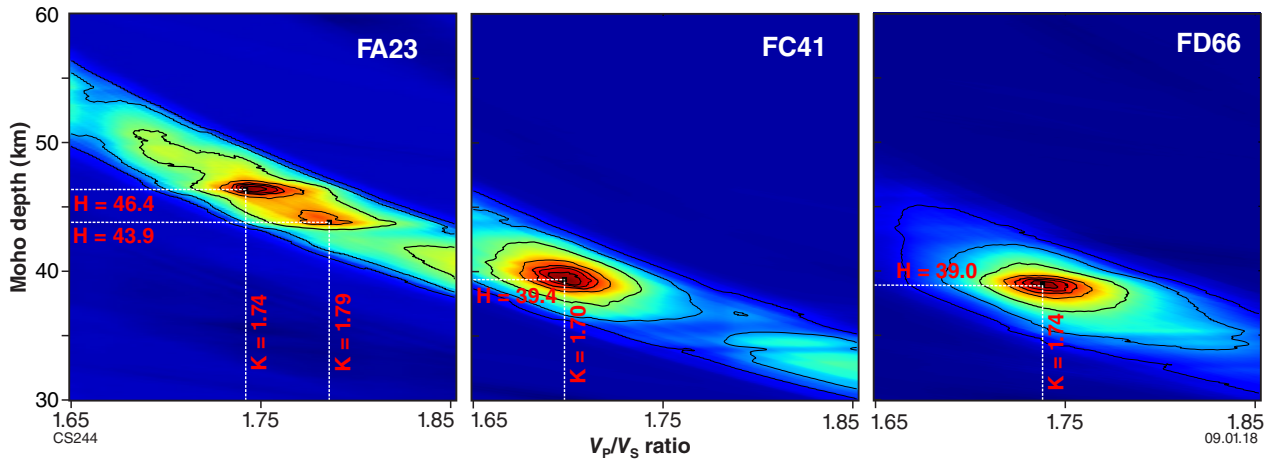


Figure 9. Examples of H–K stacks from three seismic stations. Stacked combined amplitudes of  $P_s$ ,  $PpPs$ , and  $PpSs$  phases are plotted and colour-coded in a grid of crustal thickness ( $H$ ) and  $V_p/V_s$  ratio ( $K$ ). The H–K pair with the maximum amplitude was picked; where several maxima were present each of them was picked initially. Results from this approach are summarized in Table 3

Table 3. Crustal thickness and  $V_p/V_s$  ratios obtained for all usable seismic stations

Station <sup>(a)</sup>	Lat (°)	Long (°)	No. of events used	Moho depth <sup>(b)</sup> (km)	$V_p/V_s$	Quality
KMBL	–31.36690	121.88210	53	36.4	1.75	A
AUKAL	–30.76370	121.47889	22	38.3	1.72	A
FA10	–30.78730	122.79515	31	40.4	1.65	B
FA12	–30.82537	123.32329	26	47.5	1.75	D
FA13	–30.88637	123.62059	33	45.8	1.79	C
FA14	–30.83259	123.91017	35	43.9	1.75	B–
FA15	–30.87924	124.22452	17	45.1	1.72	B
FA17*	–30.90593	124.89545	–	38.8	–	C
FA18*	–30.78173	125.17411	–	37.0	–	C
FA19*	–30.89797	125.49374	–	40.3	–	C
FA20	–31.10069	122.69717	39	39.1	1.73	A
FA22	–31.09847	123.29749	14	45.9	1.77	B–
FA23	–31.20256	123.61760	20	46.4	1.74	B
FA24	–31.08654	123.90257	34	45.0	1.71	B
FA25	–31.18328	124.21138	17	42.9	1.79	C
FA26*	–31.10626	124.52934	–	44.4	–	C
FA27*	–31.19939	124.81974	–	39.6	–	C
FA28*	–31.10220	125.07824	–	39.0	–	C
FA29*	–31.18085	125.41021	–	39.0	–	C
FA30	–31.39572	122.89263	13	40.0	1.68	C
FA31	–31.49796	122.89263	39	44.4	1.78	B
FA32	–31.58405	123.22395	35	47.1	1.80	C
FA33	–31.45780	123.53100	36	45.0	1.79	B
FA34	–31.39780	123.81655	25	44.0	1.72	B
FA35	–31.44826	124.10362	27	43.2	1.71	A
FA36	–31.39832	124.40873	9	42.2	1.76	B–
FA37*	–31.50306	124.70716	–	41.0	–	C
FA38*	–31.40955	125.02450	–	40.2	–	C
FA39*	–31.50914	125.30928	–	39.5	–	C
FB00	–31.75010	122.74270	82	44.1	1.75	D

Table 3. continued

Station <sup>(a)</sup>	Lat (°)	Long (°)	No. of events used	Moho depth <sup>(b)</sup> (km)	$V_p/V_s$	Quality
FB01	–31.90722	123.44156	30	44.2	1.73	C
FB02	–31.75068	123.87299	35	42.8	1.72	A
FB03	–31.79418	124.51704	33	38.3	1.79	B–
FB04	–32.09641	122.38266	23	42.8	1.74	C
FB05	–32.20242	122.99788	25	44.4	1.81	C
FB06	–32.23617	123.58321	33	39.1	1.75	B
FB07	–32.14236	124.19761	35	39.9	1.72	A
FB08	–32.56565	122.90781	43	40.4	1.75	B
FB09	–32.60013	123.54704	32	37.4	1.75	B
FC40	–31.89020	121.62320	39	36.8	1.69	A
FC41	–31.83229	122.18470	50	39.4	1.70	A
FC42	–32.44056	121.61932	7	39.7	1.67	C–
FC43	–32.36202	121.94400	28	37.5	1.74	A
FC46	–32.46453	123.26135	29	39.8	1.73	A
FC48	–32.85240	123.83847	15	36.5	1.75	B
FC49*	–32.49238	123.98003	–	39.2	–	C
FD50	–32.73706	121.16190	45	37.5	1.70	B
FD51	–32.91770	121.42920	36	35.1	1.73	B
FD52	–32.89060	121.87020	41	44.1	1.76	C–
FD53	–33.18230	121.89800	27	43.8	1.77	C
FD54	–33.05920	122.27341	11	39.5	1.77	C
FD55	–32.96689	122.71786	20	39.5	1.74	B
FD56	–33.14964	122.90257	16	36.4	1.73	B
FD58	–33.21350	121.00660	41	35.5	1.75	B
FD60	–33.42680	122.02370	13	40.7	1.72	A–
FD61	–33.36900	122.46420	40	39.7	1.73	C
FD62	–33.43472	123.19717	51	37.7	1.71	A
FD63	–33.65110	120.79654	28	43.7	1.73	D
FD64	–33.59851	121.14342	43	48.3	1.73	D
FD65	–33.71188	121.58604	32	40.2	1.70	A
FD66	–33.73070	122.29900	28	39.0	1.74	A
FD67	–33.56130	122.81270	29	37.0	1.74	A
FD68	–33.75409	123.28192	6	35.1	1.74	B
FD69	–33.60278	123.63065	11	37.2	1.69	B
WP08	–29.28230	121.25720	4	41.0	1.76	B
WP15	–31.21350	121.09320	9	34.9	1.75	A
WP16	–30.21130	121.08480	5	40.4	1.74	B
WP17	–31.02280	122.59850	9	38.5	1.75	B
WP18	–29.96920	122.54630	6	42.2	1.73	B
WP25	–30.47550	122.70780	6	38.2	1.77	B–
WP29	–29.76380	121.72430	12	41.4	1.70	B
WR09	–32.03640	122.79210	28	51.5	1.75	A
WT08	–30.41657	122.51029	25	37.3	1.73	B
WT09	–30.78070	121.77260	9	38.2	1.76	B
WT10	–30.41657	122.51029	19	41.6	1.71	A

Note: (a) Stations for which receiver functions were unusable are marked with an asterisk  
(b) Moho depth estimates for these stations were obtained from autocorrelograms

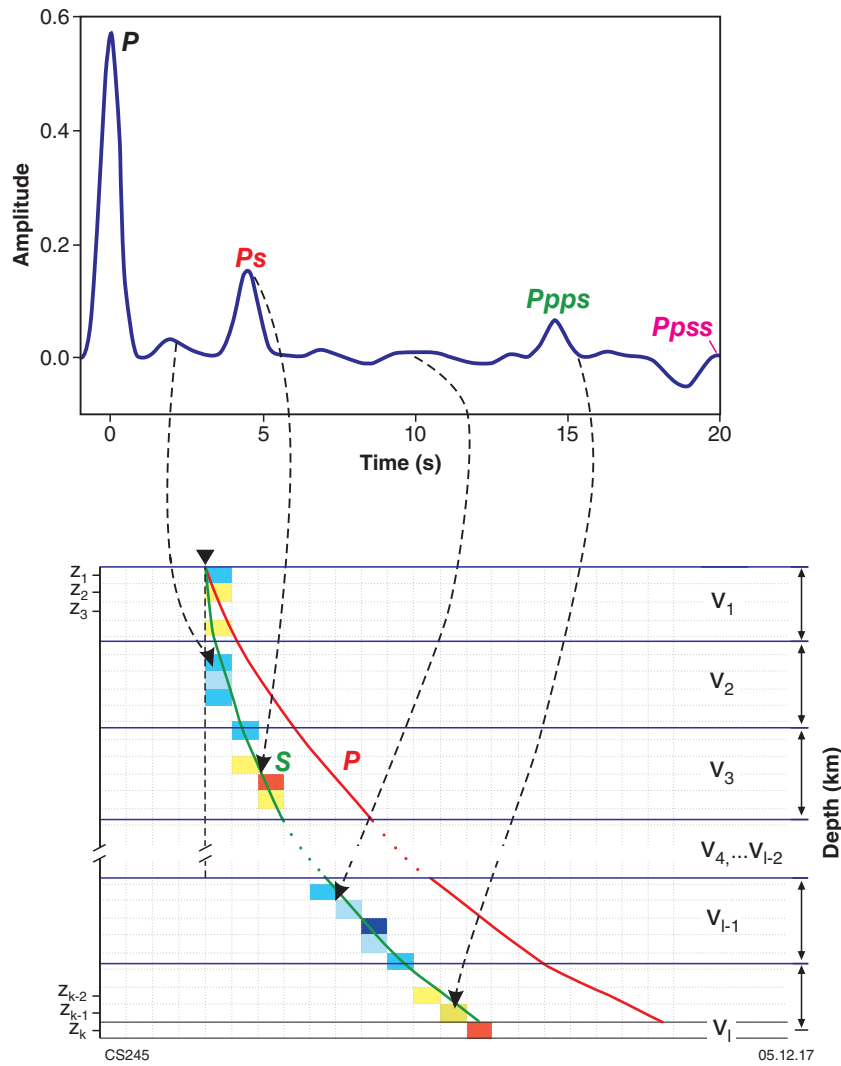


**Figure 10.** Schematic sketch illustrating the principle of CCP stacking. Receiver function amplitudes, like those shown in the upper panel, are summed along their raypaths into discrete bins, represented by the different colours. This procedure is repeated for a large number of receiver functions and stations, and each bin is normalized according to the number of contributing receiver functions. Modified from Schneider (2014)

## Interpreting receiver function results

The main information contained in receiver functions is the depth to and strength of seismic velocity discontinuities in the subsurface. Thus, the retrieved information is to the first order comparable to active seismic images, but different from volumetric methods like seismic tomography. However, there are several major differences between receiver function and reflection seismic results that should be kept in mind when comparing results.

Receiver functions are sensitive to different wavenumbers and different properties, and show discontinuities or rapid variations in  $S$  wavespeed. In contrast, active seismic methods image the reflectivity of  $P$  waves. Because waves from distant sources are used, receiver functions are dominated by waves of significantly lower frequency than seismic waves from active sources. This implies that fine structure cannot be imaged by receiver functions, and only prominent and large-scale velocity discontinuities are visible in the results. In many cases, only the Moho is

imaged. Care must be taken to avoid projection artefacts when imaging strong, short-wavelength features because the sources (i.e. the earthquakes) are usually not evenly distributed in azimuth. However, the nature of the receiver function data allows the calculation of profiles of arbitrary orientation.

## Autocorrelations

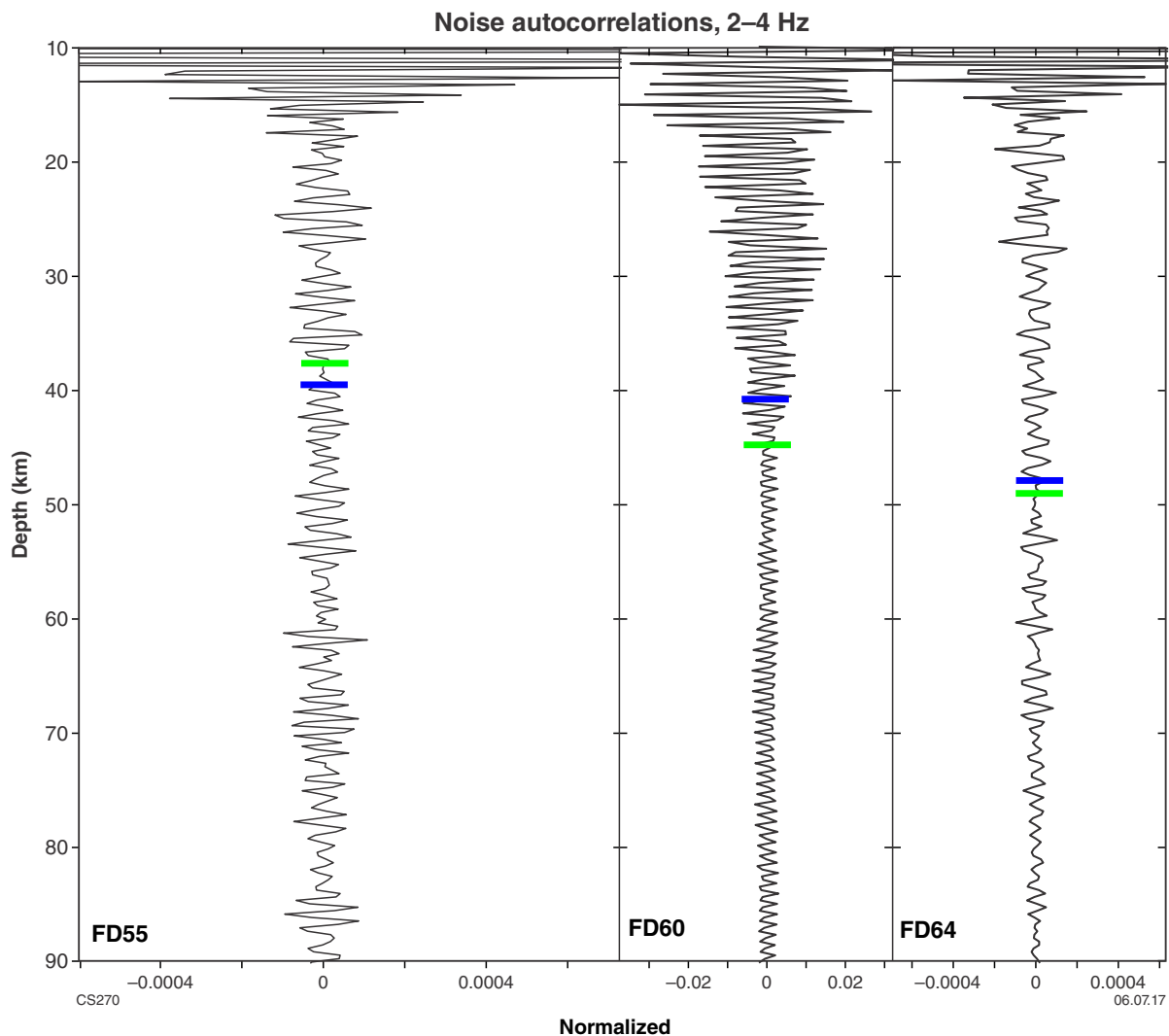
The retrieval of information about the depth to subsurface discontinuities from ambient noise or teleseismic coda autocorrelations is a currently emerging field (Gorbatov et al., 2013; Kennett et al., 2015), and there is not yet consensus about the ideal processing or approach. The principle of the method relies on the fact that reverberations from subsurface discontinuities resemble the original waveform in character, but their arrival is delayed in time. This means that by correlating such a waveform with itself, these arrivals should stand out as side-peaks next to the main peak at zero time delay. However, the studies



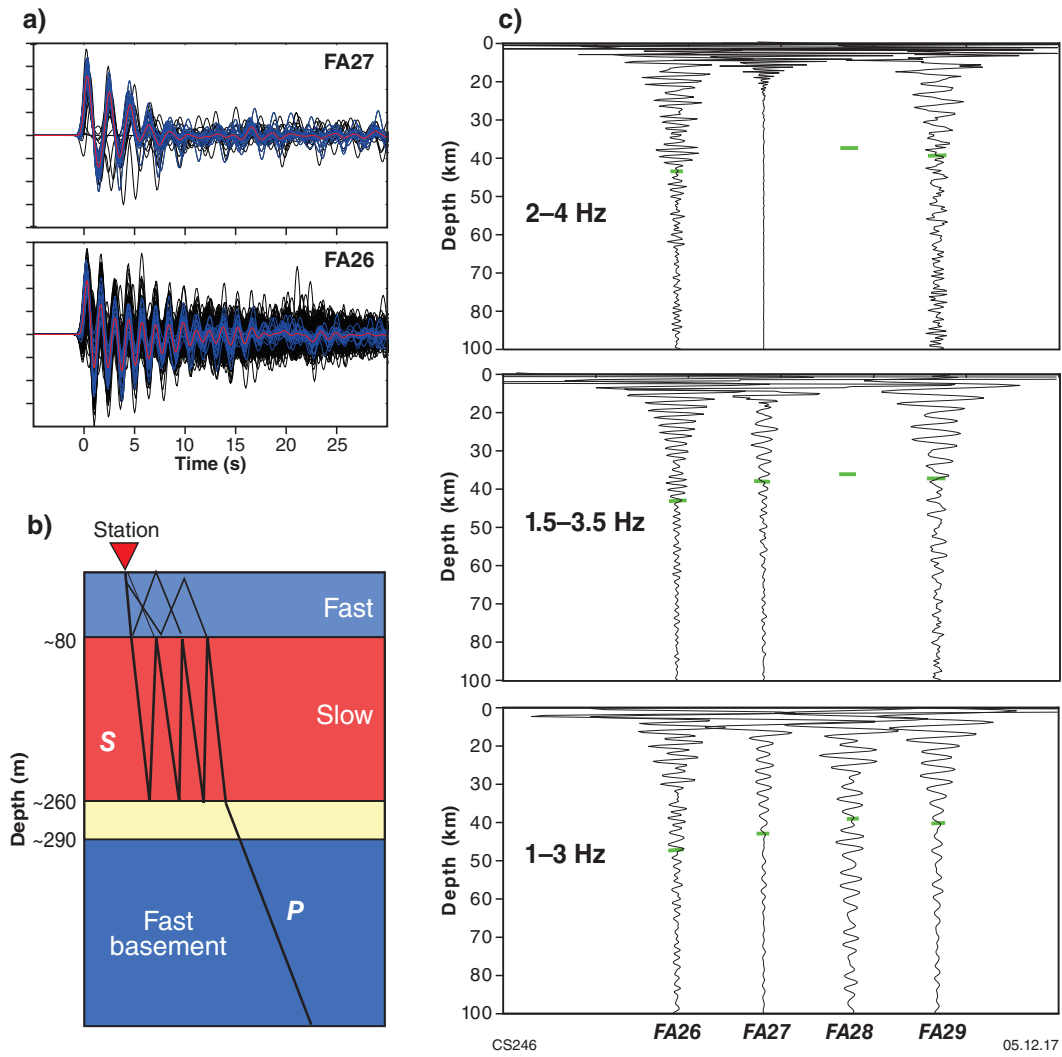
referred to above have shown that there appears to be no uniform appearance of the Moho, although commonly it is visible as a decrease in amplitude, most likely related to the termination of  $P$  wave reflectivity, as imaged with reflection seismic methods.

Figure 11 shows examples of noise autocorrelograms at three seismic stations, with the Moho picks shown in green and the H–K stacking derived Moho depths shown as blue lines. There is a fair correspondence between the values; however, it should be noted that in most cases it is not feasible to uniquely pick the Moho on an autocorrelogram because several options are normally apparent. In practice, we took the crustal thickness from AusMoho (Kennett et al., 2011) as an initial estimate, then searched for a significant decrease in amplitude of the autocorrelogram in its vicinity.

The results of the autocorrelation approach were only used for nine stations located in the northeastern part of the array, where receiver function analysis did not yield any usable results. Within that part of the array, seismically fast limestone successions of the Eucla Basin overlie significantly slower material and the faster basement, which caused substantial reverberations that rendered the receiver functions unusable (Fig. 12). Autocorrelations, which image  $P$  wave reflectivity and not  $S$  wave velocity discontinuities, are not affected by this problem, and thus the Moho depth for these nine stations were picked using this approach (Table 3). To compensate for the frequency dependence of the waveforms, we picked the Moho on autocorrelograms of ambient noise and teleseismic codas (Fig. 12), and averaged over different frequency ranges to arrive at the final Moho depth estimates.



**Figure 11.** Examples of ambient noise autocorrelations from three seismic stations. The traces shown have been bandpass filtered between 2 and 4 Hz. Depths were calculated assuming a crustal velocity of 6 km/s. The blue markers show the Moho depth estimates from H–K stacking for the three stations (Table 3), and the green markers show the Moho pick set for these traces. With the exception of station FD60, picking a Moho signal is non-unique and can only be performed using an adequate initial estimate



**Figure 12.** Aspects of the retrieved receiver function data: a) retrieved receiver functions (black, single traces; blue, subpopulation of highly similar traces; red, average receiver function) for two stations from the far northeast of the ALFEX array. No  $P_s$  peaks or multiples (see examples in Figure 8) are visible as they are obscured by strong reverberations rendering these receiver functions unusable; b) simplified sketch showing how reverberations are created. Seismically fast basement is overlain by significantly slower material (siltstones and shales of the Madura Formation) and a faster limestone 'lid'. Seismic energy propagates into the low-velocity material, where it is 'trapped', and waves bounce multiple times, releasing only a small amount of energy after each bounce. Thus, instead of a single, focused arrival as in the general case (Fig. 5), a continuous wave-train of overlapping arrivals is recorded, forming the patterns seen in panel a); c) autocorrelations from teleseismic  $P$  codas for four of the northeastern stations, plotted for different frequency bands. Although sometimes hard to see, the Moho is usually evident as an amplitude reduction, sometimes accompanied by a frequency change. Picking these for a large variety of frequency bands and seeking consistent solutions for adjacent stations yielded the values presented in Table 3

## Ambient noise tomography

It has long been known that seismic background noise (i.e. the ubiquitous reverberations recorded by seismic sensors in the absence of earthquakes) arises mainly from ocean waves and swells coupling with the solid earth (e.g. Peterson, 1993). Seismic background noise is dominated by surface waves, but smaller-amplitude body wave energy is also contained in so-called ‘microseismic noise’, which has a typical spectrum with most energy content around a characteristic peak centred at periods of 7–8 s (Fig. 13).

As recent as the early 2000s, seismologists found that these background oscillations could be exploited to retrieve surface-wave travel-times between station pairs, and that it was thus possible to perform tomography using continuous recordings of seismic noise (Shapiro and Campillo, 2004; Shapiro et al., 2005). This technique has a great advantage in that it is almost universally applicable, as no specific type of earthquake source is needed. This also means that the resolution of the tomography (i.e. raypath coverage) is defined solely by the station distribution. Contrary to methods relying on distant earthquake sources, the shallow subsurface (upper crust) can be illuminated in detail, but resolution at deeper depths is limited or absent.

## Surface waves and ambient noise

Although the technique is little more than a decade old, seismic tomography using ambient noise as a source (e.g. Shapiro and Campillo, 2004) is now one of the most commonly applied passive seismic methods. Unlike other passive seismic methods, it does not rely on the occurrence of local or distant earthquakes, but makes use of the

ubiquitous and (to a first order) constant background noise created by the interaction between the oceans and the solid earth (Fig. 13).

By cross-correlating traces of background noise from pairs of seismic stations, computing their similarity depending on an applied time shift, a so-called Empirical Green’s Function (EGF) is obtained, which is equivalent to the waveform of the surface wave travelling from one station to the other (Fig. 14a). The EGFs can then be filtered to determine group and phase velocities for different periods between station pairs, and these velocities (or travel-times) can be inverted for maps of group and phase velocities at different periods.

Surface waves at different periods are sensitive to  $S$  wavespeeds at different depths, with longer period waves sensing deeper velocities. Figure 15 shows sensitivity kernels for group and phase velocities at 2, 5, 10 and 20 s, calculated using the codes of Herrmann (2013) and taking the AusREM velocity model (Salmon et al., 2013) as a background. The surface waves always sample a depth interval, with the depth of maximum sensitivity (in km) commonly corresponding to the period of the same number. It is also apparent that the sampled depth interval grows with increasing period, which is due to the longer wavelengths utilized. Group velocity kernels are always a bit shallower than the corresponding phase velocity kernels at the same period. The resolvable depth range is, however, also limited by other factors. At the shallow end, the extraction of surface waves at periods of 1 s or shorter is usually not possible, since the signal-to-noise ratio is unfavourable at such short periods (the natural microseismic background noise is strongest between about 4 and 12 s), and the extraction techniques (see below) no longer allow clear travel-time identification.

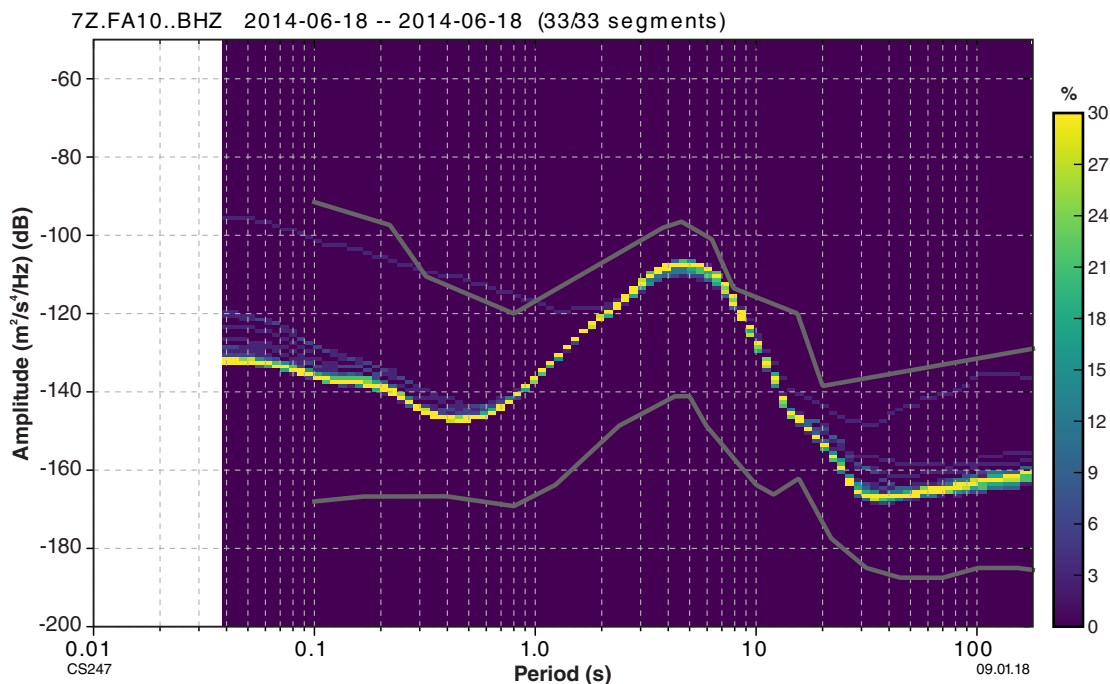


**Figure 13.** Example of an ambient noise spectrum for one day of vertical component seismic background noise at station FA10, calculated using the Probabilistic Power Spectral Density method. Relative power in dB is plotted against period. The grey lines mark the upper and lower bounds normally obtained for seismic stations globally. The most prominent feature is the so-called ‘microseismic peak’, which usually occurs at periods of 6–8 s (here at somewhat shorter periods). The signal is generally strongest between about 2 and 10 s

Towards longer periods, there are two factors that limit the usable period range; instrumentation and array footprint. Because the ALFREX array partly consists of short-period sensors, the use of periods longer than 20 s is not feasible (Fig. 14). Moreover, a long-standing rule states that only rays that travelled at least three wavelengths should be used in the analysis in order to avoid near-field effects (e.g. Bensen et al., 2008). Using an approximate surface-wave velocity of 3.5 km/s, this implies that for the 20 s period, only station pairs with a separation of more than 210 km should be analysed. The ALFREX array has a footprint of about 350 x 350 km (Fig. 1), which means that regardless of instrumentation, the long-period limit imposed by array size is likewise at about the 20 s period (see also the plots of raypath coverage in the Appendix).

## Processing — determination of group and phase velocities

EGFs for fundamental mode Rayleigh waves were obtained by cross-correlating the vertical components of all available waveform data for all station pair combinations. Traces were downsampled from 50 to 10 Hz and bandpass filtered to between 0.01 and 1 Hz before the correlation step. Amplitudes were normalized by multiplying the traces by the inverse of a moving-window amplitude average (Bensen et al., 2007), and spectral whitening was also applied. The cross-correlation was performed with a time-domain routine contained in the ObsPy software package (Beyreuther et al., 2010) on hourly data segments; 24 of these hourly segments were added to form daily stacks, which were also used to check for timing errors.

### Group velocity retrieval

Group velocity represents the propagation speed of wave packages, and as such is determined by looking at an envelope over the entire wavetrain, and not at specific phases within the wavetrain, which travel with phase velocity (Fig. 14). Frequency-time analysis (FTAN, e.g. Levshin et al., 1992) was applied and a phase-matched filtering approach (Arroucau et al., 2010; Levshin and Ritzwoller, 2001; Young et al., 2011) was used for the extraction of group velocities from the symmetric component (i.e. averaged causal and acausal parts) of the EGFs. The period range utilized was 2–20 s, in steps of 1 s below 10 s and 2 s above (Fig. 14c). As described above, only station pairs separated by at least three wavelengths were used for the retrieval of dispersion curves (Bensen et al., 2008; Lin et al., 2008).

### Phase velocity retrieval

A semi-automated approach that picks phase velocity dispersion curves from plots of phase velocity versus period (Yao et al., 2006) was applied to the symmetric component stacks. The code attempts to pick the maximum positive phase amplitudes for all periods within a pre-defined range of possible phase velocities. All resulting dispersion curves (an example is shown in Fig. 14c) were visually checked and, if necessary, modified. This most often involved correcting the picked phase velocity for the shortest periods, where the algorithm occasionally picked the wrong branch, inconsistent with the longer-period picks. As with the group velocity determination, we applied

the criterion of only using rays containing at least three wavelengths, resulting in most observations lying in the period range of 4–7 s (Fig. 16).

## Methods — tomographic inversion

To obtain two-dimensional maps of the distribution of group and phase velocities, we applied the iterative non-linear tomographic inversion code FMST (Rawlinson and Sambridge, 2004, 2005), which utilizes a subspace method. The study area was parameterized as a regular, rectangular grid of 60 x 60 nodes, and a total of 10 iterations were performed for each dataset (phase and group velocities, each period). A homogeneous velocity model set to the average observed phase or group velocity at each period was used as the starting model for the inversion. The forward method, i.e. the calculation of theoretical travel-times, was performed with an eikonal solver included in the FMST package. The optimal values for smoothing and damping were chosen by L-curve analysis (Eberhart-Phillips, 1986), separately for each inversion problem. We also excluded travel-time observations that deviated substantially (more than two standard deviations and absolute residual >1.5 s) from the mean of all observations from the analysis, but the amount of discarded picks only amounted to about 2% of all observations. The obtained residual reductions lay between 67 and 19% compared to the starting models, with the shorter-period inversions achieving higher reductions than the longer-period inversions. A summary plot of residual reductions is provided in Fig. 17.

## Interpreting ambient noise tomography results

The outputs from the procedures described above are maps of phase and group velocities of fundamental mode Rayleigh waves. These are directly related to shear wave velocities, and anomalies in one correspond to anomalies in the other (absolute values, however, do not correspond). Although these maps are 2D, carrying out the inversion at different periods introduces some constraint on the depths of anomalies. Both group and phase velocities have known sensitivity kernels, i.e. the relative contributions of different depth regions to one period are known. As a rule of thumb, the maximum sensitivity of a period is located at about the same depth in kilometres (e.g. a period of 10 s means maximum sensitivity at around 10 km depth), with group velocity sensitivity always located somewhat shallower than phase velocity sensitivity. In reality, surface waves sample  $V_s$  over a range of depths, and this range increases with increasing period (Fig. 14). The previously stated rule of thumb refers to the maximum of sensitivity. The range of periods used in this study primarily sample the upper crust, with a smaller contribution of lower crustal depths at the longest periods, and little to no sensitivity at mantle depths (Fig. 14).

Lateral resolution within each phase or group velocity map depends on the available ray geometry, which is spatially variable. For interpretation purposes, anomalies must be checked against synthetic tests (see **Results** and the **Appendix**), which demonstrate the presence or absence of good resolving capability in a particular area. In general, shorter periods nearly always exhibit better



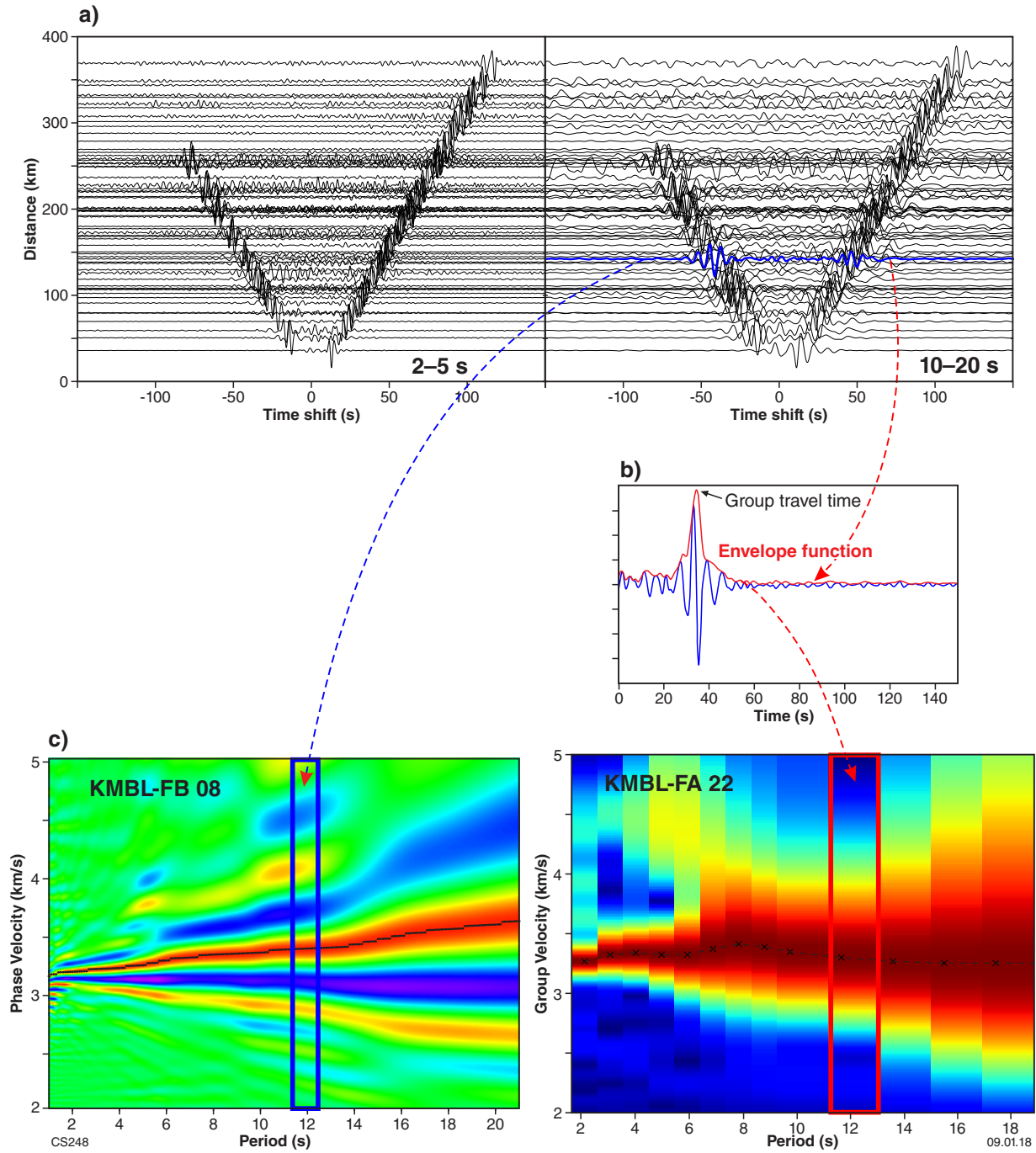
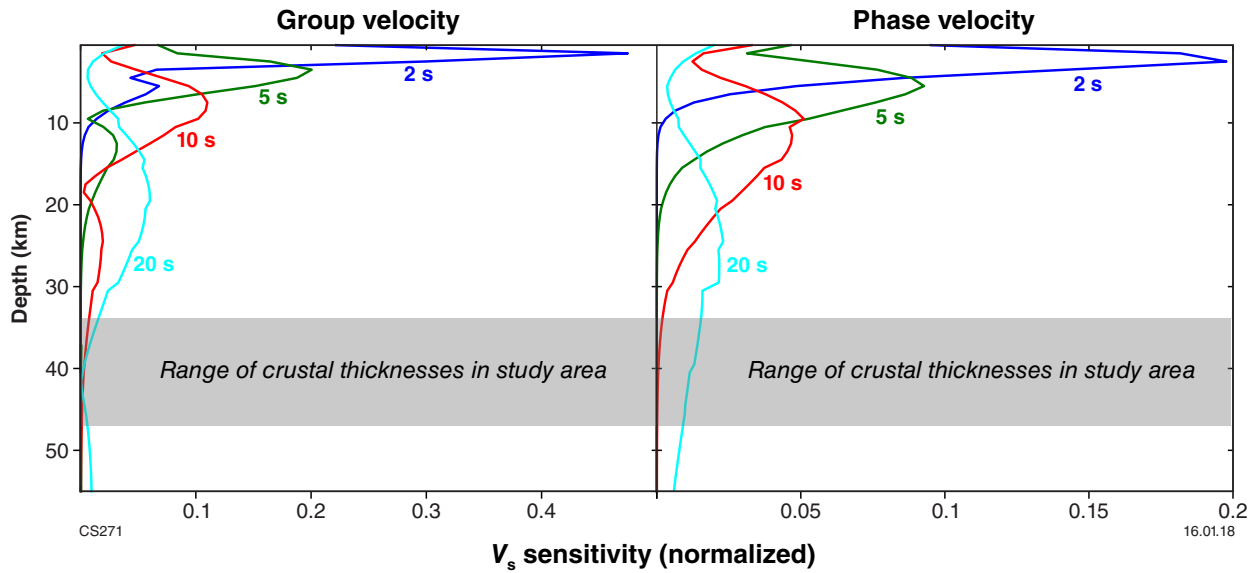
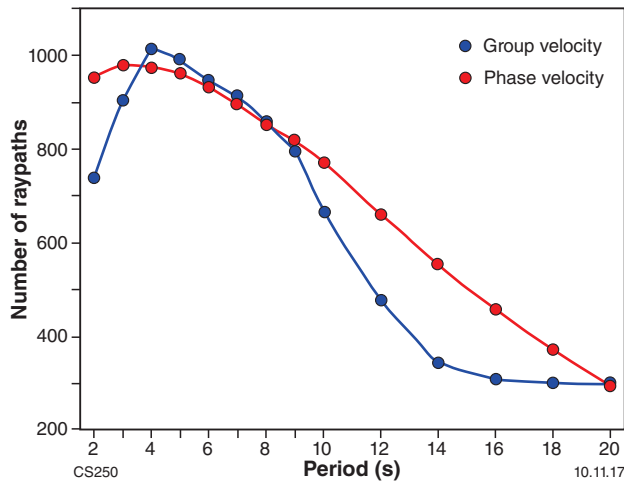


Figure 14. Seismic tomography using ambient noise as a source: a) examples of EGFs for all station-pair combinations that include station FA10. Each trace corresponds to the cross-correlation of data from station FA10 with one other station; traces are sorted by inter-station distance. The horizontal axis shows the cross-correlation time shift, corresponding to the inter-station travel-time of the imaged surface waves. The result is a V-shaped pattern, which corresponds to surface waves travelling from station FA10 to the other stations (left branch; negative time shifts) and from the other stations to FA10 (right branch; positive time shifts). In the uppermost part of the V, i.e. for the most distant stations in the far south of the network, the pattern is asymmetric because there was considerably more energy propagating from the 'source' of the background noise, i.e. the stations that were close to the ocean. For the calculation of phase and group travel-times, single traces (like the one highlighted in blue) were analysed in narrower frequency (or period) windows; b) for group velocity retrieval, the envelope function of the symmetric component (the sum of both branches of panel a) of the different traces was analysed; c) examples of phase and group velocity picks for one station pair. Symmetric component traces (for phase velocity; left) or their envelopes (for group velocity; right) are plotted against period; picked maxima are shown with black lines. A trace like the one highlighted in panel a) corresponds to a vertical column of this plot (a period window). Note that traces are plotted not against time, but against velocity





**Figure 15.** Group and phase velocity sensitivity kernels for periods of 2, 5, 10 and 20 s, calculated using the codes of Herrmann (2013) and assuming AusREM as a background 1D crustal model (Salmon et al., 2013). These plots show that surface waves of longer period sample increasingly deeper depths, and that the sampled range becomes wider with increasing period. For our study, the period range utilized mostly samples of the upper crust. A contribution from lower crustal depths occurs at the longest periods.



**Figure 16.** Total number of raypaths used for different periods. For a plot of raypath geometries, see Figures A3, A4

lateral resolution than longer ones. This is partly due to the wavelength criterion mentioned above, which limits the number of available raypaths for longer periods. However, a second reason is that longer wavelengths are intrinsically less sensitive to the presence of smaller-scale heterogeneity, and the determination of group and phase velocities from ambient noise recordings has higher uncertainties for longer periods (e.g. Fig. 14b,c).

## Results

### Crustal thickness and $V_p/V_s$ maps

Values of crustal thickness and bulk crustal  $V_p/V_s$  ratios for all ALFLEX stations, for some adjacent stations from the WACRATON deployments (Reading et al., 2003; Goleby et al., 2006), and for two permanent stations in Kambalda and Kalgoorlie (the latter is part of the ‘Seismometers in Schools’ project: Balfour et al., 2014) are supplied in Table 3. Figure 18 shows a Bouguer gravity image with contoured isolines that are overlain onto interpolated maps of the two parameters over the entire study area (Fig. 19).

The most prominent feature in the derived crustal thickness map (Fig. 19a) is a belt-like region of significantly thickened crust (~45 km thick) that extends from northeast to southwest through the study area. As indicated by the gravity isolines (Figs 18, 19), this belt is situated slightly west of the Fraser Zone, but extends southwest beyond its limits, albeit at apparently diminished amplitude. The deepest Moho (51.5 km) was obtained from station WR09, which was located close to the southwestern termination of the Fraser Zone, and slightly west of the associated maximum amplitude gravity high. The observed slight westward difference between the location of the Fraser Zone gravity high and the thickest crust obtained with this method is likely a geometrical artefact. Although a wide variety of teleseismic earthquake azimuths were tentatively used (Fig. 6), most of the usable receiver functions came from eastern and northern azimuths. This means that the measurements of H and K values projected onto the station locations (Fig. 19a) actually represent the crust somewhat north and west of each station.

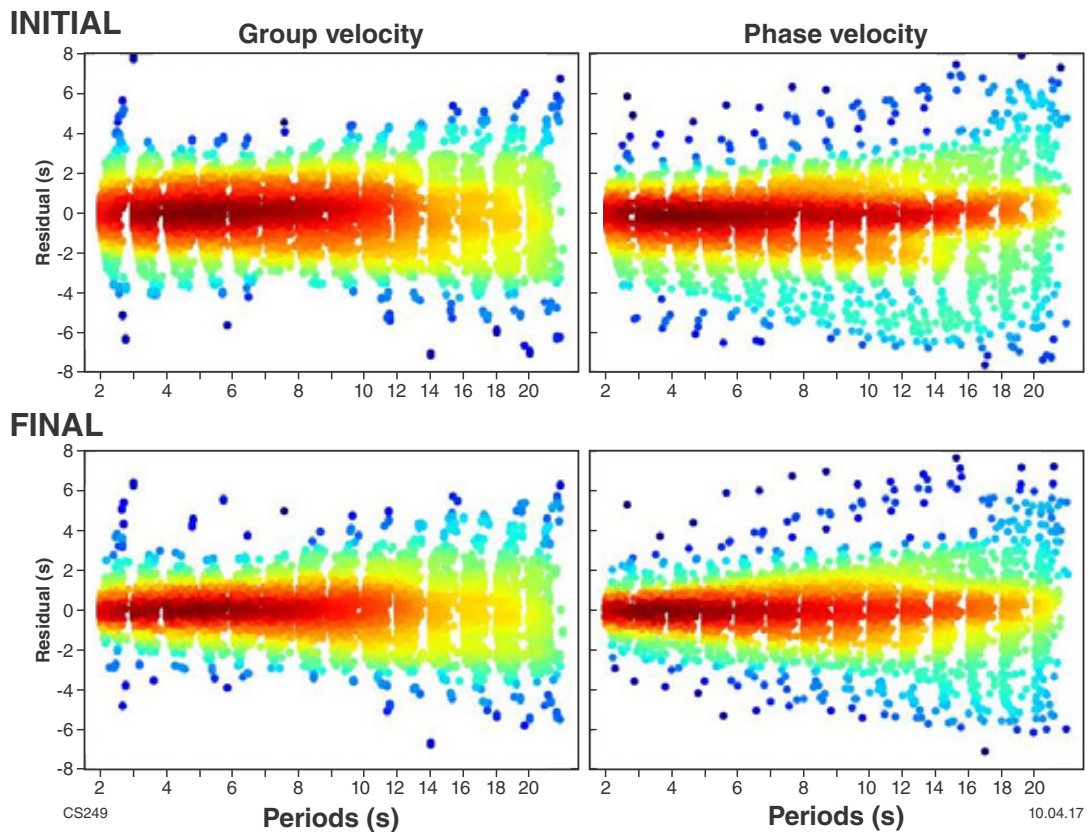


**Figure 17.** Summary plot for residual distributions before (upper row) and after (lower row) tomographic inversion with FMST. Each imaged dot corresponds to one travel-time residual (i.e. theoretical minus retrieved travel-time). Colour coding is with respect to logarithmic point density. Warmer colours imply higher density than cooler colours. Residuals are plotted against period, and for each period against absolute travel-time

The imaged belt of thicker crust lies parallel to the gravity isolines in the southwest, but to the northeast it deviates northwards, and also widens. East and west of the central belt of thickened crust, retrieved Moho depths are relatively uniform, with values of about 35–40 km. To the east, over the Eucla Basin, crustal thicknesses for the stations where Moho depths were determined from autocorrelations (marked with thicker circles in Fig. 19a), are consistent with those from adjacent areas.

The distribution of retrieved  $V_P/V_S$  ratios is patchier than that of crustal thicknesses, which may be due in part to the inherently higher uncertainties. Nonetheless, some general trends can be recognized (Fig. 19b). The highest  $V_P/V_S$  ratios ( $\sim 1.8$ ) correlate with the position of the Fraser Zone metamorphic rocks in the upper crust. The region of strongly elevated  $V_P/V_S$  ends at the southwestern termination of the Fraser Zone, but an elongate region of slightly higher than average  $V_P/V_S$  ( $\sim 1.75$ ) extends farther southwest with the same northeasterly trend as the Fraser Zone. Directly west of the belt with high  $V_P/V_S$  ratios is a region of very low  $V_P/V_S$  ( $< 1.7$ ). Northwest of this, in the Yilgarn Craton,  $V_P/V_S$  values of around 1.73 are obtained, which represent intermediate to felsic rocks. Similar values were obtained for most of the southern part of the east AFO. The easternmost stations of the array, on the western margin of the Eucla Basin, show elevated  $V_P/V_S$  ratios that appear to coincide with the western edge of a northwesterly

trending gravity anomaly (Figs. 2, 18). Whether this implies that the crust under this part of the Eucla Basin (where reverberations rendered receiver functions unusable; Fig. 12a) contains predominantly mafic rocks cannot be determined because of the paucity of data points.

As previously discussed, H–K stacking relies on the assumption of horizontal converters (here, a horizontal Moho) as it averages measurements from different azimuths. However, suggestions of substantial short-wavelength variations in Moho topography are evident in Figure 19, which raises the question as to whether this assumption is violated in this case. To check for this,  $P_s$  phases in the receiver functions, which are a primary proxy for Moho depth, were picked manually. The inner quartile range of the distribution of  $P_s$ – $P$  time differences for all stations (Fig. 20) is a good indicator of the variability or spread of observed values. The plotted inner quartile range is systematically larger in areas of highly variable Moho topography (suggested by the contour lines in Fig. 19a), and smaller in the areas of flat Moho to the northwest and southeast of the study area. Some stations along the western edge of the thickened crust, defined as a ‘Moho trough’, exhibited the highest inner quartile ranges, and were investigated in further detail. Figure 20b shows directional plots of the picked  $P_s$  times. Each dot is positioned at the azimuth and distance from the station at which the associated ray pierces the Moho. The colour

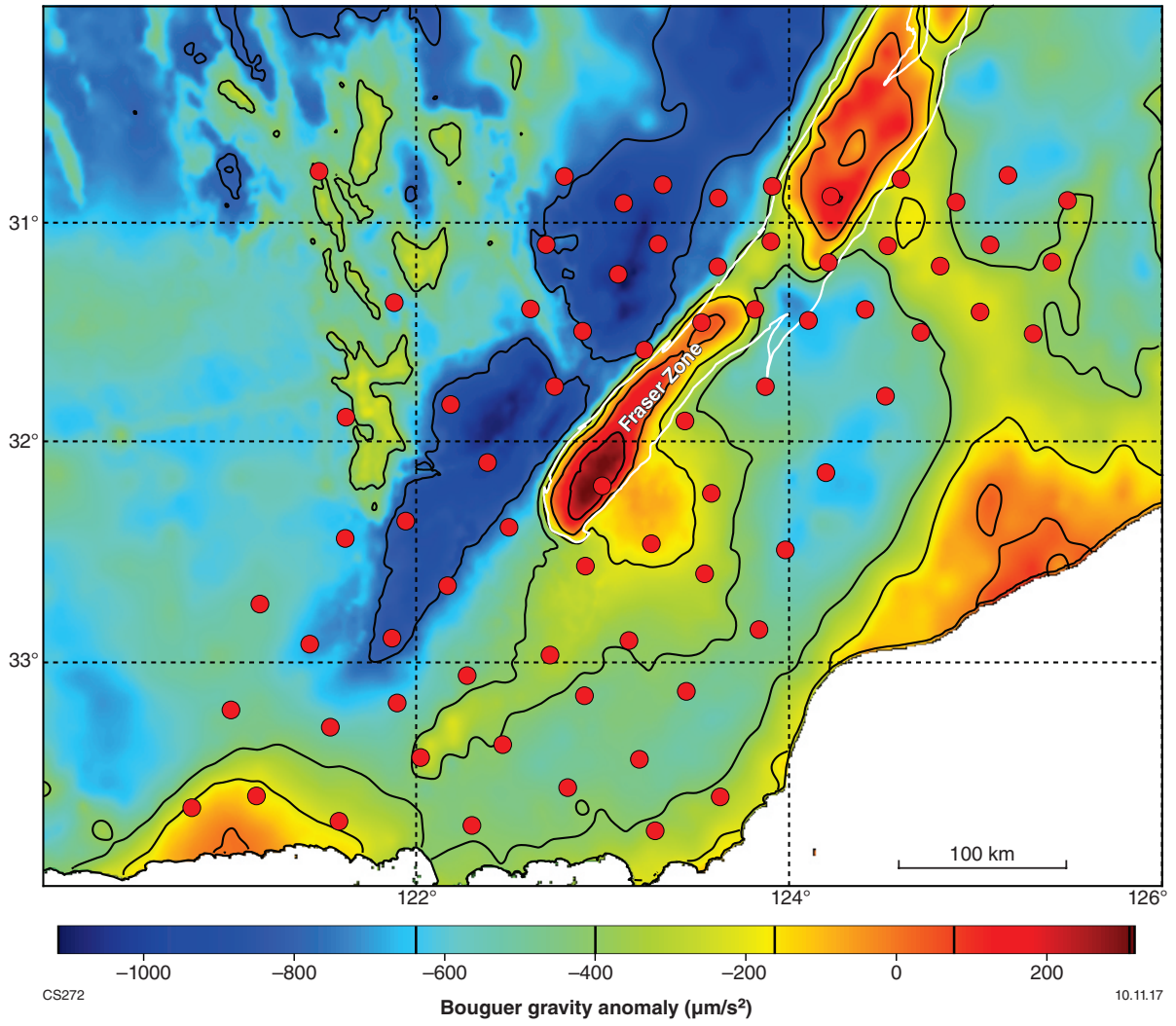


Figure 18. Bouguer gravity image of the study area, showing the contoured gravity isolines shown in Figures 19 and 25–28

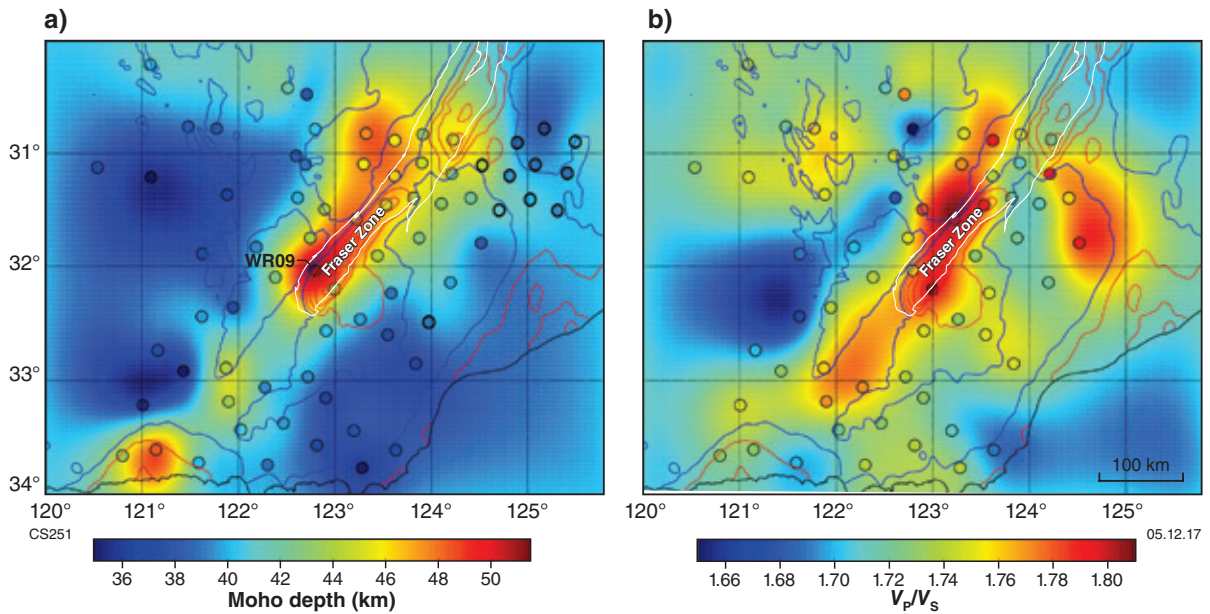


Figure 19. Comparison of interpolated Moho depth and  $V_p/V_s$  ratios: a) interpolated Moho depth map. Circles with a thick black outline denote stations for which the Moho depth estimate was calculated using autocorrelations rather than receiver functions; these stations do not have corresponding  $V_p/V_s$  ratio values; b)  $V_p/V_s$  ratio map. Coloured dots represent values obtained from seismic stations (Table 3). Colours of the background map are an interpolation between these values. Bouguer gravity anomaly isolines (from Figure 18) are superimposed as blue (representing negative gravity anomalies) and red (representing positive anomalies) lines



code is the observed time difference between direct  $P$  arrival and the  $P_s$  phase. In both cases, there is a very clear and abrupt change of  $P_s$ - $P$  time with direction, which suggests a very steeply dipping Moho, or possibly a Moho offset.

To improve the resolution of the Moho depth observations, individual  $P_s$ - $P$  times were converted to depths using a crustal  $V_p$  of 6.4 km/s and a  $V_p/V_s$  ratio of 1.73 (Fig. 21a). Although this conversion provides a superior spatial resolution to the H–K stacking results, which had only one measurement per station, the ability to differentiate between the effects of variations of crustal thickness and those of  $V_p/V_s$  changes was lost. However, there is good agreement between the Moho picks from the active seismic profiles and the point measurements derived by depth conversion (Fig. 21a). A smoothed interpolation of crustal thickness through all of these points (Fig. 21b) shows most of the features of the narrower southwestern part of the Moho trough more prominently than in Figure 19a. Maximum crustal thicknesses in most of that area are similar to crustal thickness values to the northeast, in the vicinity of the Fraser Zone. Also of note is that the slight westward shift of the crustal thickness maxima relative to the location of the Fraser Zone gravity high (Fig. 19a) is not observed because the crustal thickness values were obtained at the actual piercing points of the raypaths through the Moho.

## CCP profiles

CCP profiles provide a more direct view of Moho topography and its along-strike variation beneath the east AFO than that discussed in the preceding section. Three CCP profiles oriented perpendicular to the strike of the east AFO were constructed (Fig. 22), and the locations of tectonic units and upper crustal features such as faults and shear zones were marked along the top of each profile (Fig. 23). In each of these profiles, the Moho is readily identified as the most prominent phase of positive receiver function amplitudes, which imply an upward velocity decrease, denoted in shades of red in Figure 23. These profiles show a clear along-strike progression from northeast to southwest.

To the northeast, in profile A–A', the Moho trough is wide and has a symmetric V-shaped geometry with gentle troughward dips on either side of a depth maximum that is situated under the central part of the southern Fraser Zone. Beneath the Yilgarn Craton to the northwest, and beneath the eastern Nornalup Zone in the southeastern part of the profile, a clear horizontal Moho is imaged.

Profile B–B', situated close to the southwestern termination of the Fraser Zone, shows a steeper-sided, narrower and deeper asymmetric Moho trough. The dip of the eastern flank of the Moho trough is gentle and continuous at the same angle, whereas the dip of western flank is steeper, with its dip angle increasing towards the trough axis. At the trough axis the western flank of the Moho trough appears to impinge onto, or is truncated by, the eastern flank. The crustal thickness maximum is situated near the interface between the Northern Foreland and the Biranup Zone.

In contrast, the geometry of the Moho along Profile C–C' resembles a Moho step, rather than a trough. The western

flank is roughly horizontal whereas the eastern flank dips moderately westwards. At the deepest point of the Moho on this profile, crustal thickness is equivalent to the maximum crustal thickness in the Moho trough farther north. It is worth noting that there is no evidence for a second Moho discontinuity; rather, there appears to be a gap in the Moho above the northwest-dipping flank of the Moho trough.

It should also be noted that absolute Moho depths from these profiles are systematically greater than those derived from the Moho mapping described above (see **Crustal thickness and  $V_p/V_s$  maps**). This is due to the assumption of a global background velocity model that leads to an underestimation of crustal velocities and thus an overestimation of depth. However, this assumption should have minimal effect on the differences of depth between adjacent stations (i.e. on the imaged geometry).

## Upper crustal seismic velocities

Group and phase velocity anomalies obtained for all periods between 2 and 20 s are described in this section. Synthetic 'checkerboard' resolution tests and raypath coverage diagrams, referred to below, are provided in the Appendix.

## Synthetic tests

It is standard practice to assess the resolution capability of a tomographic inversion by performing a synthetic 'checkerboard' test as follows. Using the same event–station geometry as for the real data, synthetic travel-times are determined by use of a model with alternating velocity anomalies of  $\pm 7.5\%$  for each node superimposed onto the mean velocity for each period. To account for the uncertainty in determining group or phase velocities, Gaussian noise was added to the synthetic travel-times. We chose standard deviations between 0.5 (for the short periods up to 7 s) and 1.0 s (for the longest periods), because the uncertainty in travel-time determination is larger for longer periods. All other inversion settings chosen (e.g. smoothing and damping) were identical to the real data inversion runs. The retrieved images (Figs A1, A2) show adequate reconstructions of the input checkerboard pattern for the shorter periods, whereas considerable smearing of anomalies occurs from 12 s onwards, especially for the group velocity maps. This is due to both the longer-period waves being less sensitive to small-scale variations and the smaller number of utilized raypaths (see ray distribution in Figs A3, A4) due to the wavelength criterion described above. Group velocities at longer periods are typically less well determined, which is clearly shown by comparison of the two images in Figure 14c. At shorter periods, however, the checkerboard tests show that resolution is generally good within the station network, with some reduction in amplitude but good retrieval of the shape of anomalies. Group velocities appear to be marginally better resolved than phase velocities. Low resolution and strong smearing in the northwestern corner of the network occurs because all raypaths in this area travelled to or from a single station. Anomalies in this part of the array were therefore omitted from the interpretation of the data.



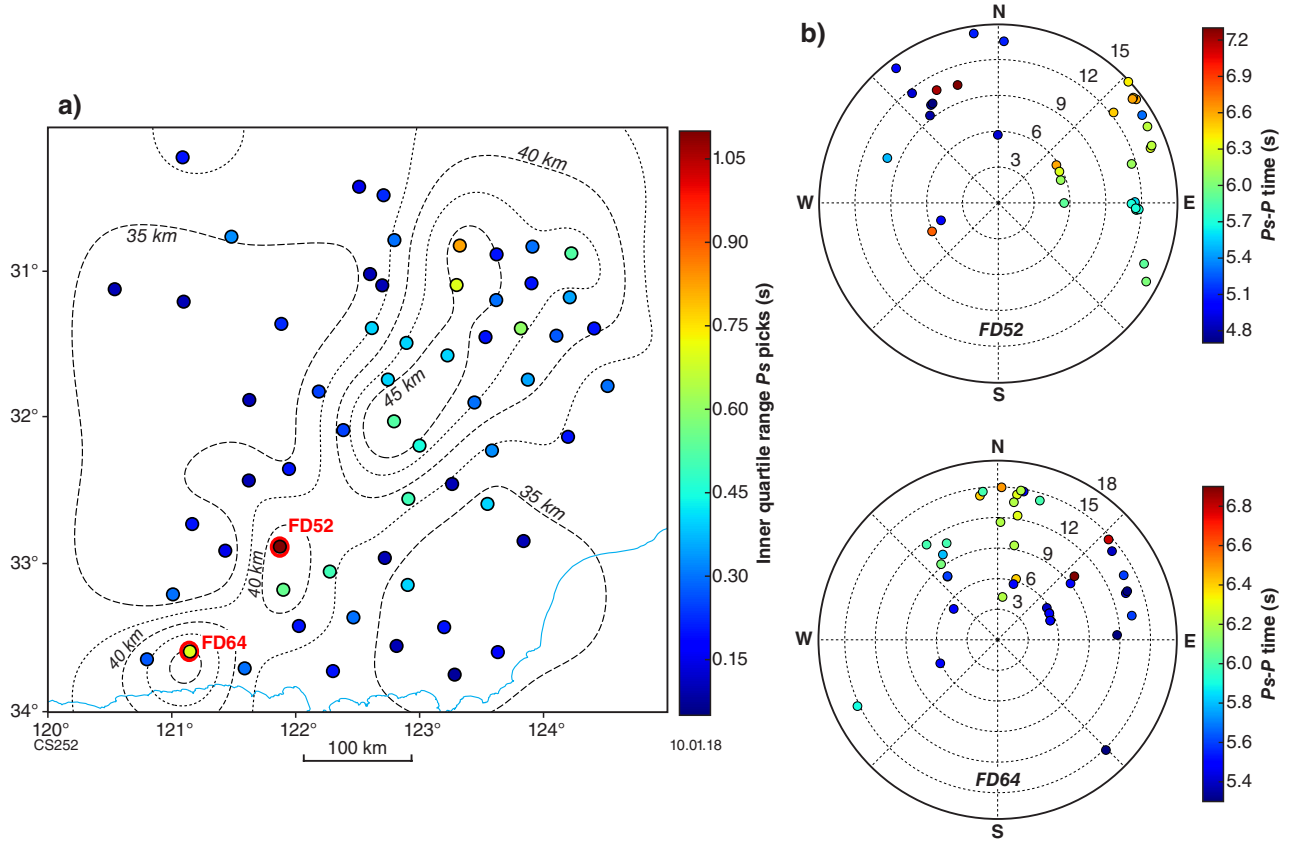


**Figure 20.** Inner quartile ranges of handpicked  $P_s$ - $P$  times: a) map showing inner quartile ranges of handpicked  $P_s$ - $P$  times for all investigated seismic stations. The crustal thickness isolines from Fig. 19a are superimposed to show that high values are obtained where a significant crustal thickness gradient is present. Two examples of exceptionally high inner quartile ranges are shown by red dots; b)  $P_s$ - $P$  times of the individual receiver functions for stations FD52 and FD64, shown with red dots in panel a). The locations of the Moho piercing points of the receiver functions are shown in polar plots (azimuth and distance from station in kilometres). In both cases, there are clear variations of  $P_s$ - $P$  times with direction, which suggests substantial topographic variability of the Moho directly beneath the station

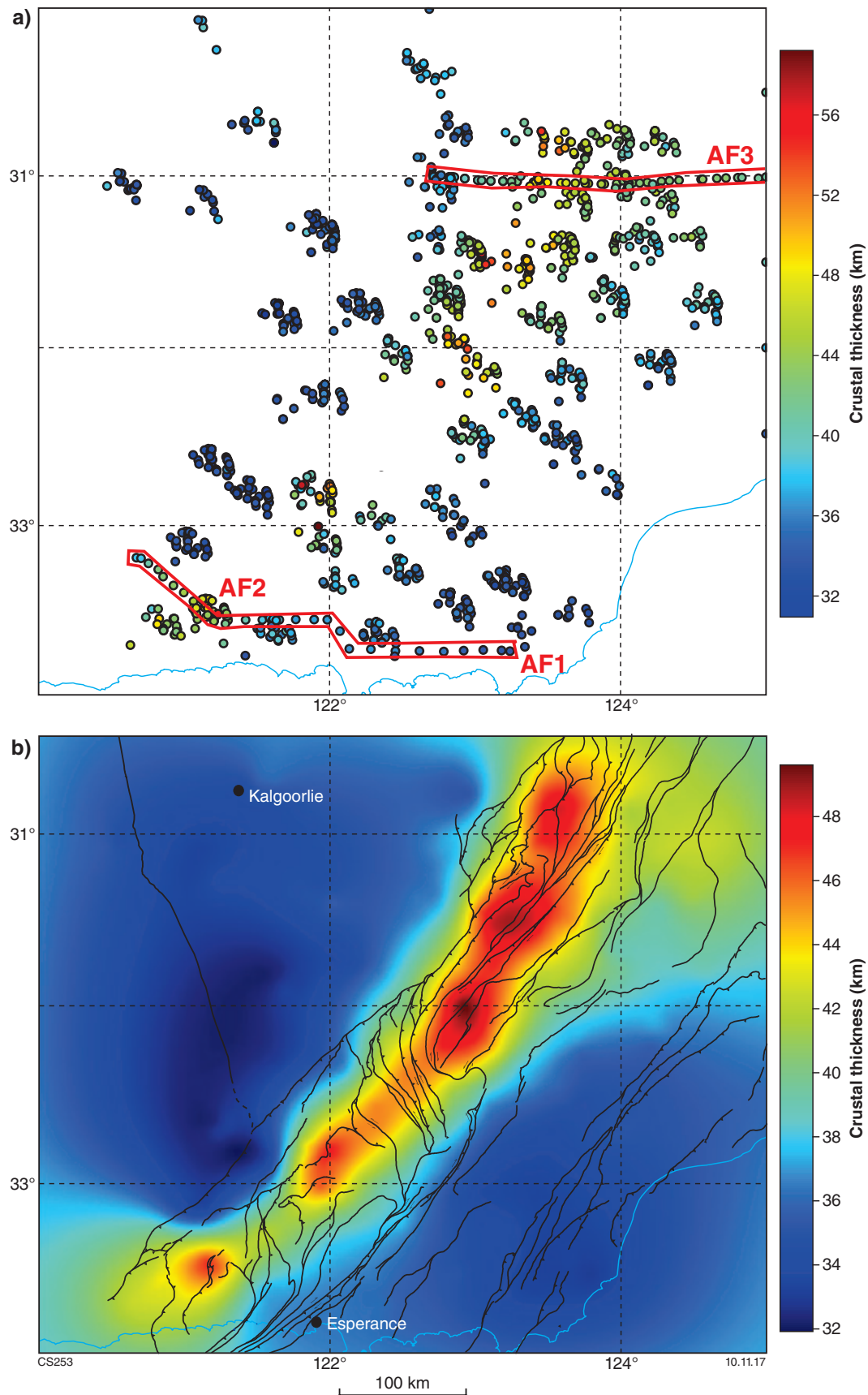


**Figure 21.** Crustal thickness map: a) Moho depth values obtained from individual receiver function traces, assuming a bulk crustal  $V_p/V_s$  ratio of 1.73. Each depth value is plotted at its Moho piercing point location, analogous to Figure 20b. Moho picks from the active seismic profiles 12GA-AF1, 12GA-AF2, and 12GA-AF3 were included, and are consistent with depths from receiver function analysis; b) crustal thickness map obtained by interpolating all the point measurements shown in panel a), which shows similar features to the H–K stacking map (Fig. 19a), but resolves the narrower southwestern part of the observed Moho trough in greater detail. The traces of shear zones, faults, and tectonic unit boundaries (from Fig. 1) are shown for reference

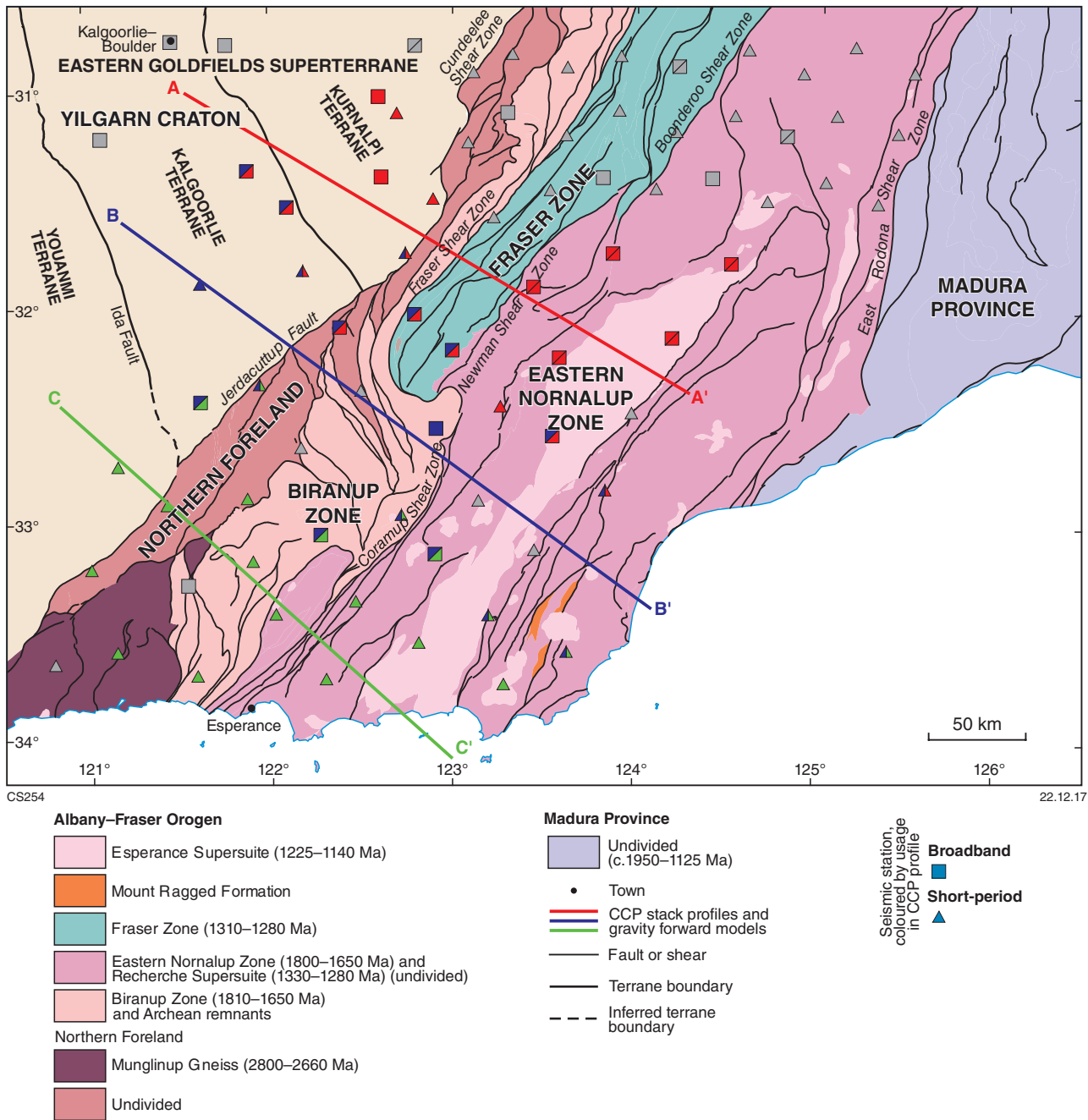


**Figure 22.** Tectonic unit map of the east AFO showing locations of three CCP profile lines oriented perpendicular to the main strike of the orogen. Stations that were used for the profile projections are shown in the same colour as the corresponding profile line; stations that were not used (either due to data issues or because they were located too far from the profile) are shown in grey

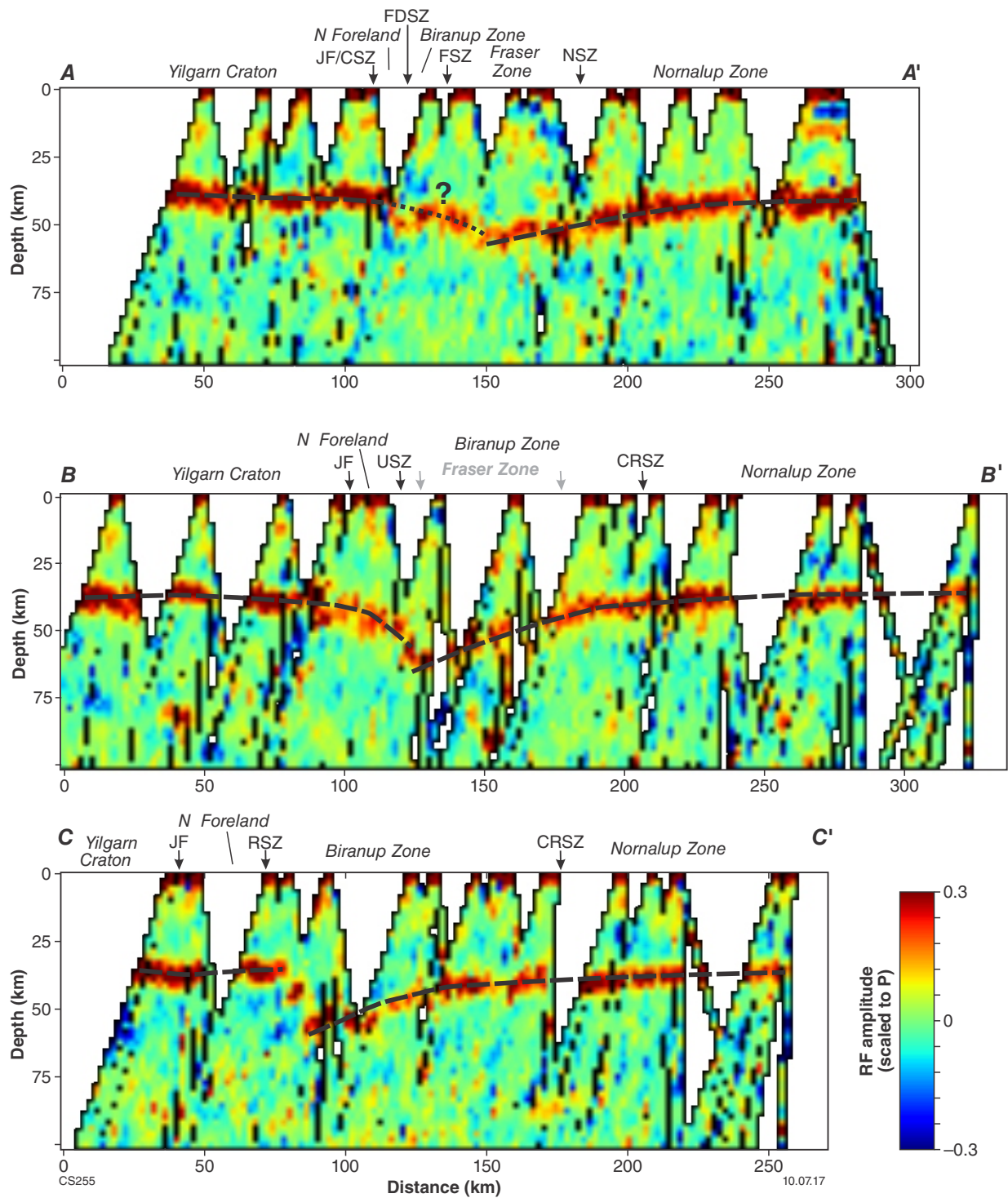


**Figure 23.** Three profiles obtained from CCP stacking of receiver functions. Profile locations and the stations used for their construction are shown in Figure 22. The Moho is identified as the most prominent phase of positive receiver function (RF) amplitudes, which imply an upward velocity decrease, denoted in shades of red and highlighted by a dashed line or, where uncertain, by a dotted line. The approximate location of major faults or shear zones separating tectonic units of the east AFO are marked with black arrows. Grey arrows or text denote features that are projected onto the profile. Abbreviations: CRSZ, Coramup Shear Zone; CSZ, Cundeelee Shear Zone; FDSZ, Frog Dam Shear Zone; FSZ, Fraser Shear Zone; JF, Jerdacuttup Fault; NSZ, Newman Shear Zone; RSZ, Red Island Shear Zone; USZ, unnamed shear zone



## Phase and group velocity maps

Median dispersion curves for the entire ALFLEX array (Fig. 24) attest to the dominance of generally very high surface-wave velocities ( $>3$  km/s) throughout most of the study area, as previously found (albeit with much lower resolution) by Saygin and Kennett (2012). This is due to the absence of extensive sedimentary successions and the presence of seismically fast basement rocks at, or very close to, the surface. The distribution of Rayleigh wave group and phase velocities (Figs 25–28) at different periods (i.e. different depth regions) shows several features that coincide remarkably well with Bouguer gravity anomalies. Moreover, there is a high degree of similarity between group and phase velocity maps for the same period, which attests to the robustness of the results. Only anomalies that are consistently visible in both group and phase velocity maps were used in the interpretations. In general, phase velocities have maximum sensitivity at slightly deeper levels than group velocities for the same period, which can also partly explain the differences between the images. Longer-period surface waves sample  $V_s$  over an extended depth range (Fig. 15), therefore pinpointing the depth of an anomaly is increasingly difficult as period lengthens.

The most prominent anomaly in the shorter-period maps is an elongate, north-northeasterly striking high-velocity region (H1 in Figs 25–28) that coincides with the position of the gravity high caused by the metamafic-dominated rocks of the Fraser Zone (orange contours in Figs 25–28). This anomaly is clearly imaged in the short-period maps at about the 2–9 s period (Figs 25, 27), and its northern part is diminished in the phase velocity map at the 10 s period. That the group velocity map at the same period still shows this northern part of the anomaly most likely indicates that the associated  $S$  wavespeed anomaly disappears at a depth of about 10 km, or deeper. From 14 s onwards, the group velocity maps can no longer resolve this anomaly (Fig. 26), which could be due to rather poor resolution at these periods. In the phase velocities, the southern part of this anomaly (H1) is present to at least the 18 s period (Fig. 28), whereas the northern part disappears at about 12 s. Anomaly L1, which is denoted by low velocities in the Eucla Basin for short periods, is much more prominent in the group velocities, where it is distinct down to the 9 s period. In the phase velocities L1 is weaker, and disappears at shorter periods. A more detailed discussion of the retrieved anomalies that are labelled in Figures 25–28 is provided below (see **Upper crustal structure**).

## Interpretation

### Craton edge geometry imaged with passive seismic methods

Passive seismic data analysis and CCP profiles have revealed a distinct along-strike variation of Moho geometry, which changes from a wide, symmetric, V-shaped ‘Moho trough’ in the northeast, to a ‘Moho step’ in the southwest, where the lower, eastern flank appears to be discontinuous with the western flank. The V-shaped Moho depression in the northern part of the study area narrows and deepens

southwestwards until the Moho step is reached along profile C–C' (Fig. 23). This change of geometry coincides with the approximate position of the Ida Fault, a major structure associated with the boundary between the Eastern Goldfields Superterrane and the Youanmi Terrane within the Yilgarn Craton (Fig. 22). In the study area, the position of this structure is uncertain because of Archean granite intrusions and Proterozoic crustal reworking, whereas to the northwest the Ida Fault is visible in aeromagnetic and seismic reflection data and surface outcrops (Swager et al., 1997; Blewett et al., 2010; Dentith et al., 2013). This terrane boundary is likely to have been a pre-existing zone of weakness coincident with an abrupt change in material strength, possibly leading to upper–lower plate coupling at the time of the Albany–Fraser Orogeny, which in turn may have led to the localization of the observed offset within the Yilgarn Craton (Fig. 23).

Although a region of thicker crust beneath the east AFO was already identified in the interpretation of the active seismic profiles 12GA-AF1, 12GA-AF2 and 12GA-AF3 (Fig. 29; Spaggiari et al., 2014c), the along-strike transition from a one-sided to a two-sided trough-like feature was not apparent due to the restricted coverage. Moreover, the seismic reflection profiles show a much gentler downwarp of the Moho, likely due to apparent dip angles because the active seismic lines were oriented east–west (along existing roads), and not perpendicular to the dominant northeast strike of the east AFO. This explanation also assumes that the strike or trend of the lower crust is similar to the upper crust, which is not necessarily the case. However, we note that the active seismic profiles correspond well with the compiled smoothed maps of crustal thickness (Fig. 30), but not with the more pronounced short-wavelength Moho topography observed in the CCP profiles (Fig. 23). Substantially thickened crust identified west of our study area from onshore–offshore active seismic data (Mjelde et al., 2013; Tassell and Goncharov, 2006) may indicate that the Moho feature we have documented continues to follow the strike of the AFO and wraps around the southern margin of the Yilgarn Craton, possibly as far west as the Darling Fault and adjacent Pinjarra Orogen.

The coincidence of the southwestern termination of the Rason Regional Gravity Low (Fig. 2) with the transition from continuous to discontinuous Moho geometry indicates that the prominent regional gravity high associated with the Fraser Zone is related to an upper crustal feature (corroborated by the velocity highs in the group and phase velocity maps; Figs 25–28), whereas the prominent parallel regional gravity low may be due to the geometry of the crust–mantle boundary. We cannot resolve the latter with the ambient noise tomography, since the periods used only sample shallower depths (Fig. 15). The presence of a region of thicker crust following the strike of the east AFO, with significantly lower density than the underlying mantle, could produce the observed linear gravity low. Its absence would then be diagnostic for the one-sided, discontinuous Moho geometry described in this study. Conspicuously, the short active seismic profile in the Tropicana area (12GA-T1; Occhipinti et al., 2014), which is located just northeast of the termination of the Rason Regional Gravity Low, shows evidence of an east-under-west configuration in the lower crust, broadly resembling the observation in the southwest of our study area.

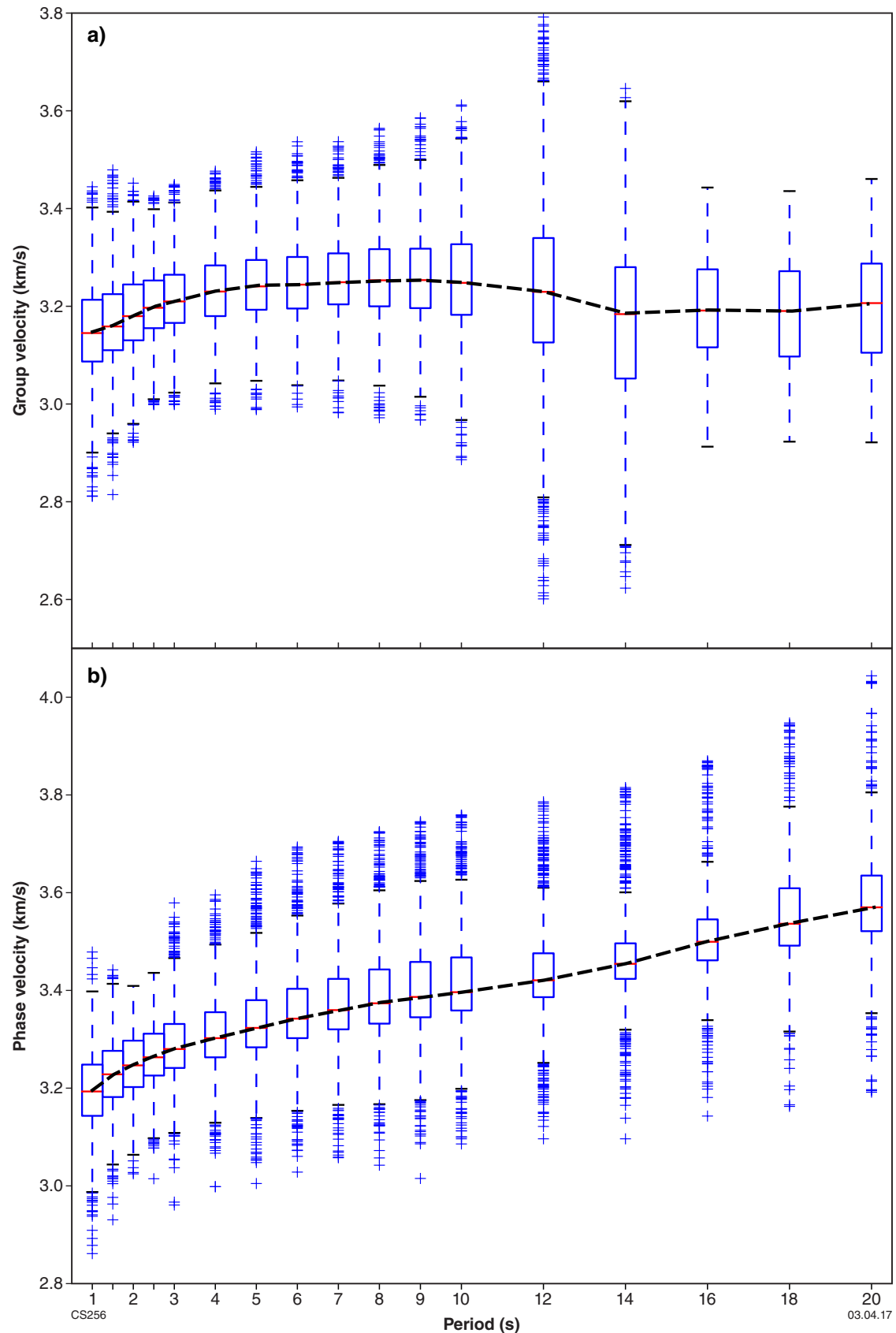


**Figure 24.** Box and whisker plots of median dispersion curves for the entire ALFREX array: a) plot of group velocities; b) plot of phase velocities. For each evaluated period, the distribution of velocity values is shown as a boxplot, where the red horizontal line represents the median value, and the blue box around it shows the inner quartile range. The 'whiskers' mark two additional inner quartile ranges. All points outside this range are considered outliers (blue plus signs). The group velocity dispersion curve is nearly flat, whereas phase velocities increase with period and are generally faster

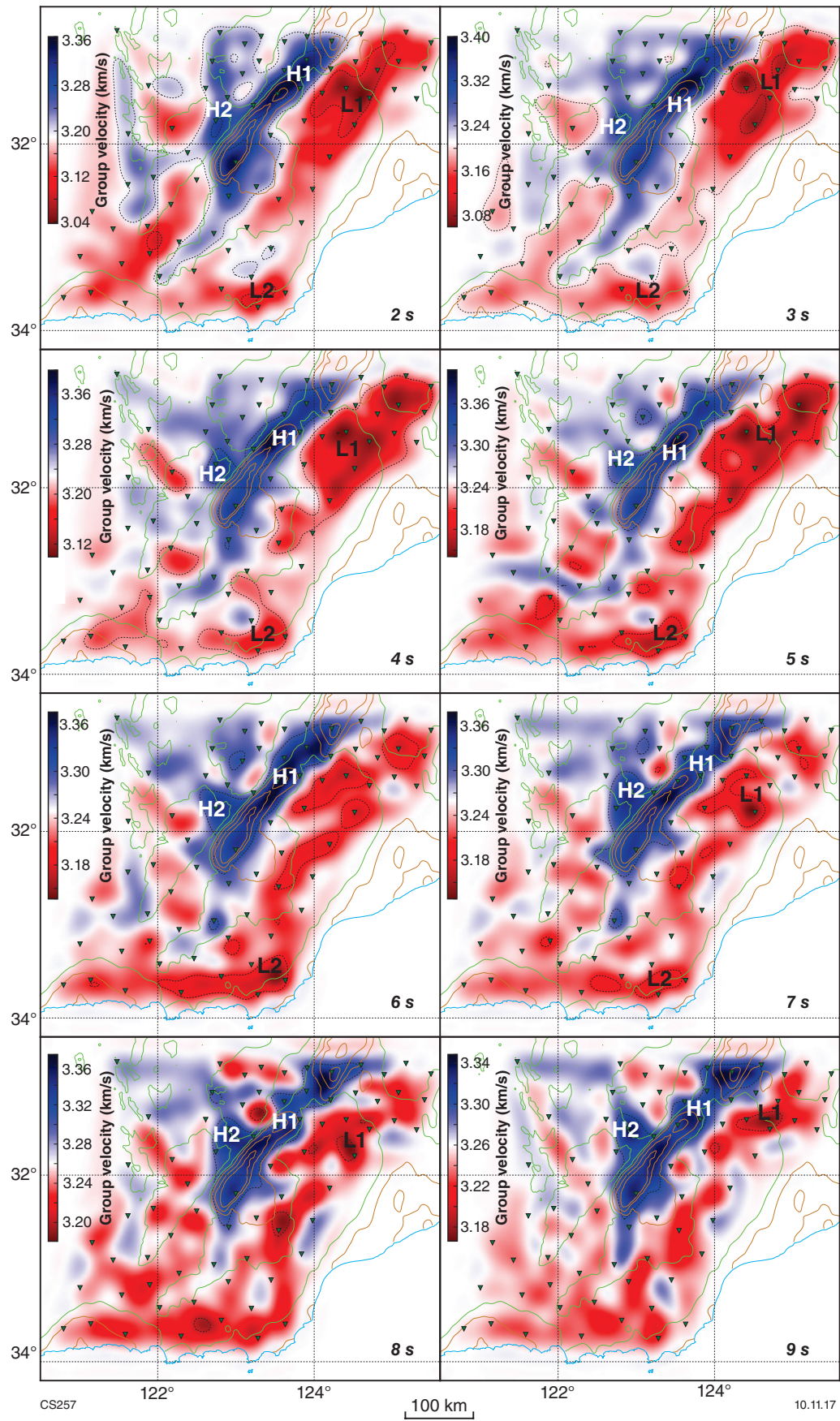


**Figure 25.** Group velocity maps for periods of 2–9 s. Bouguer gravity anomalies are marked by green (negative) and orange (positive) isolines. Inverted triangles indicate locations of ALFREX seismic stations. Velocity isolines are drawn at intervals of 0.1 km/s. White in the colour scale is the mean velocity at each period. Note that the absolute velocities and the widths of the colour scale vary between images. Velocity anomalies referred to in the text are labelled



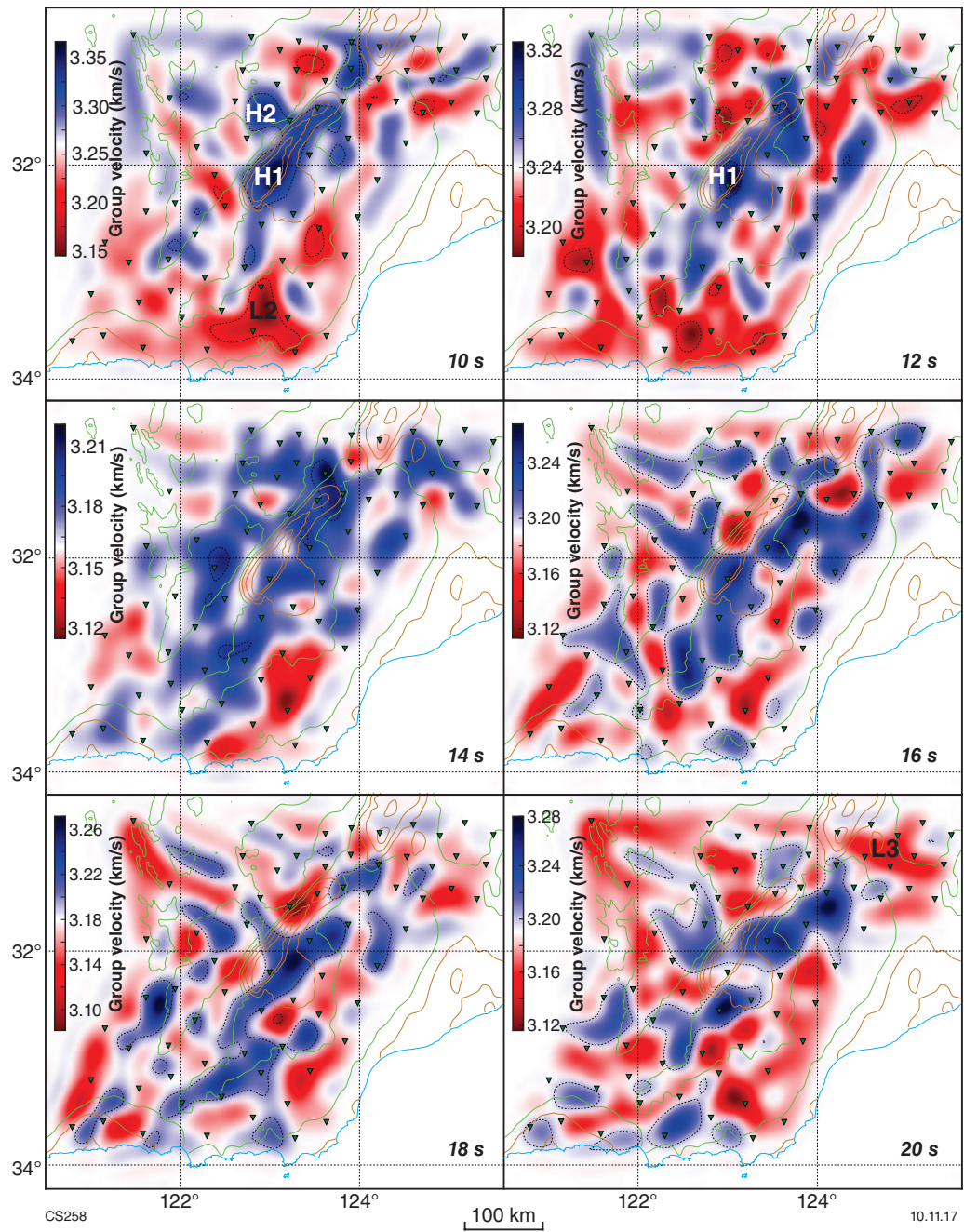


**Figure 26.** Group velocity maps for periods of 10–20 s. Note that these images are noisier and the velocity variations are smaller than those in Figure 25. For annotations refer to Figure 25



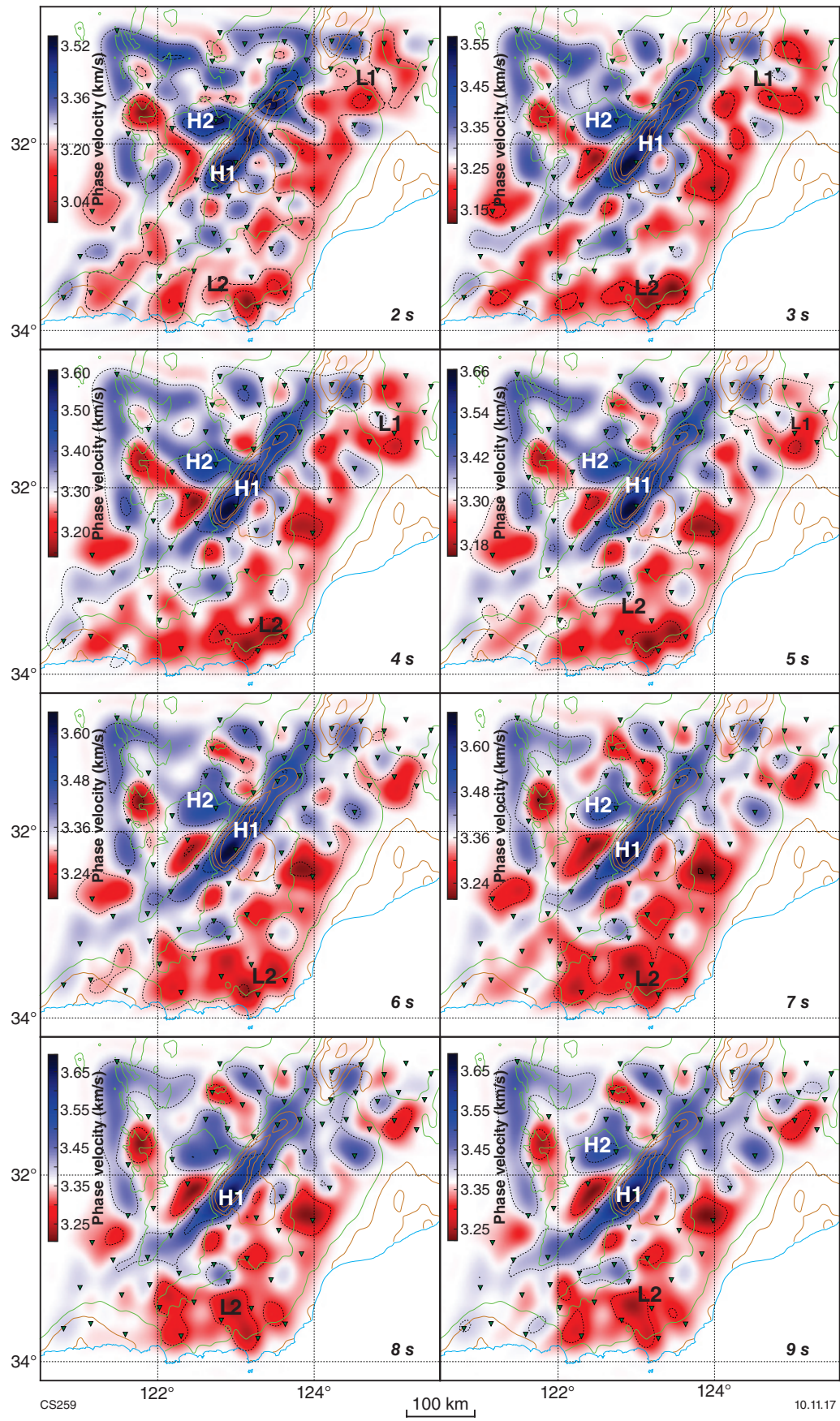


Figure 27. Phase velocity maps for periods of 2–9 s. For annotations refer to Figure 25

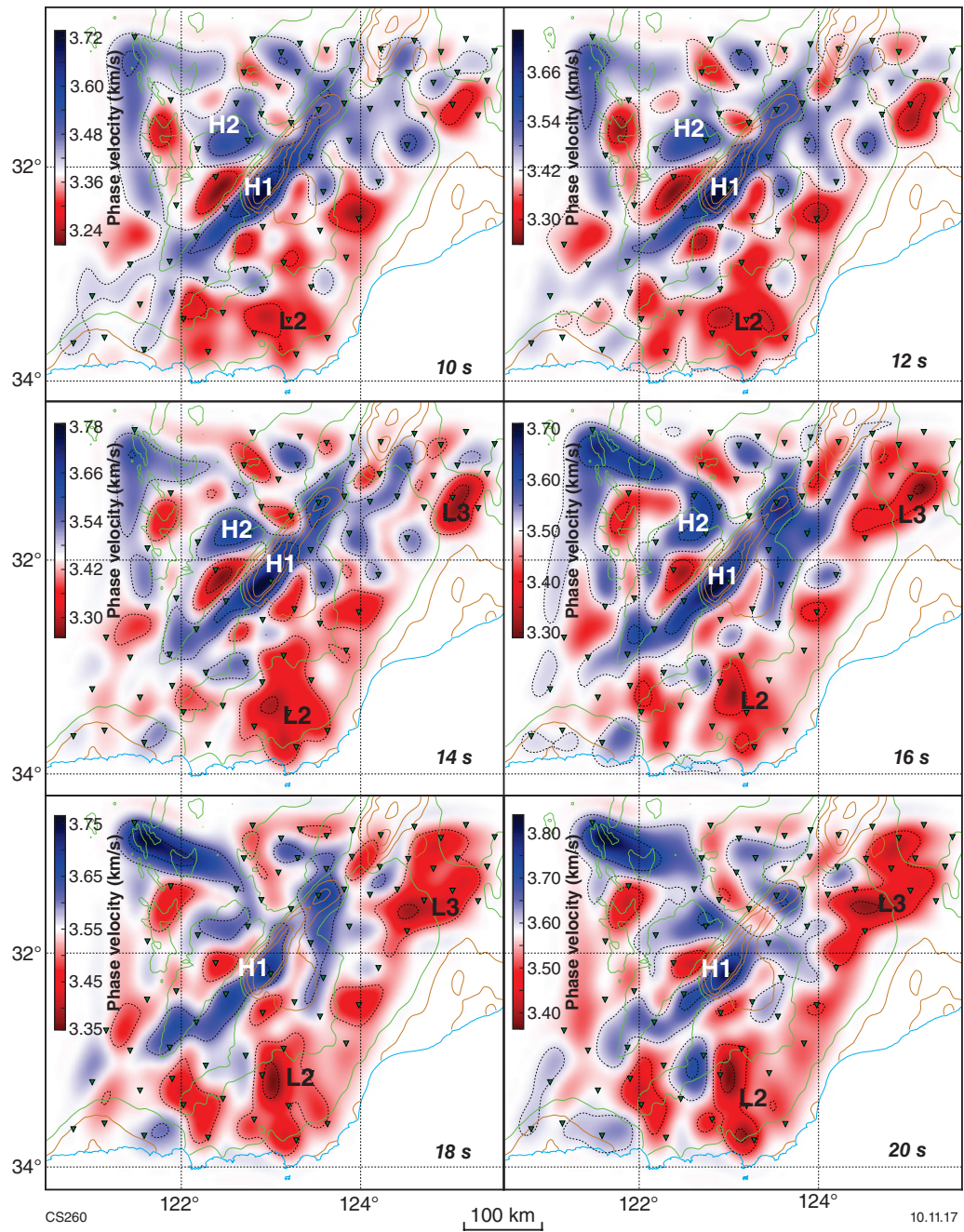


Figure 28. Phase velocity maps for periods of 10–20 s. For annotations refer to Figure 25



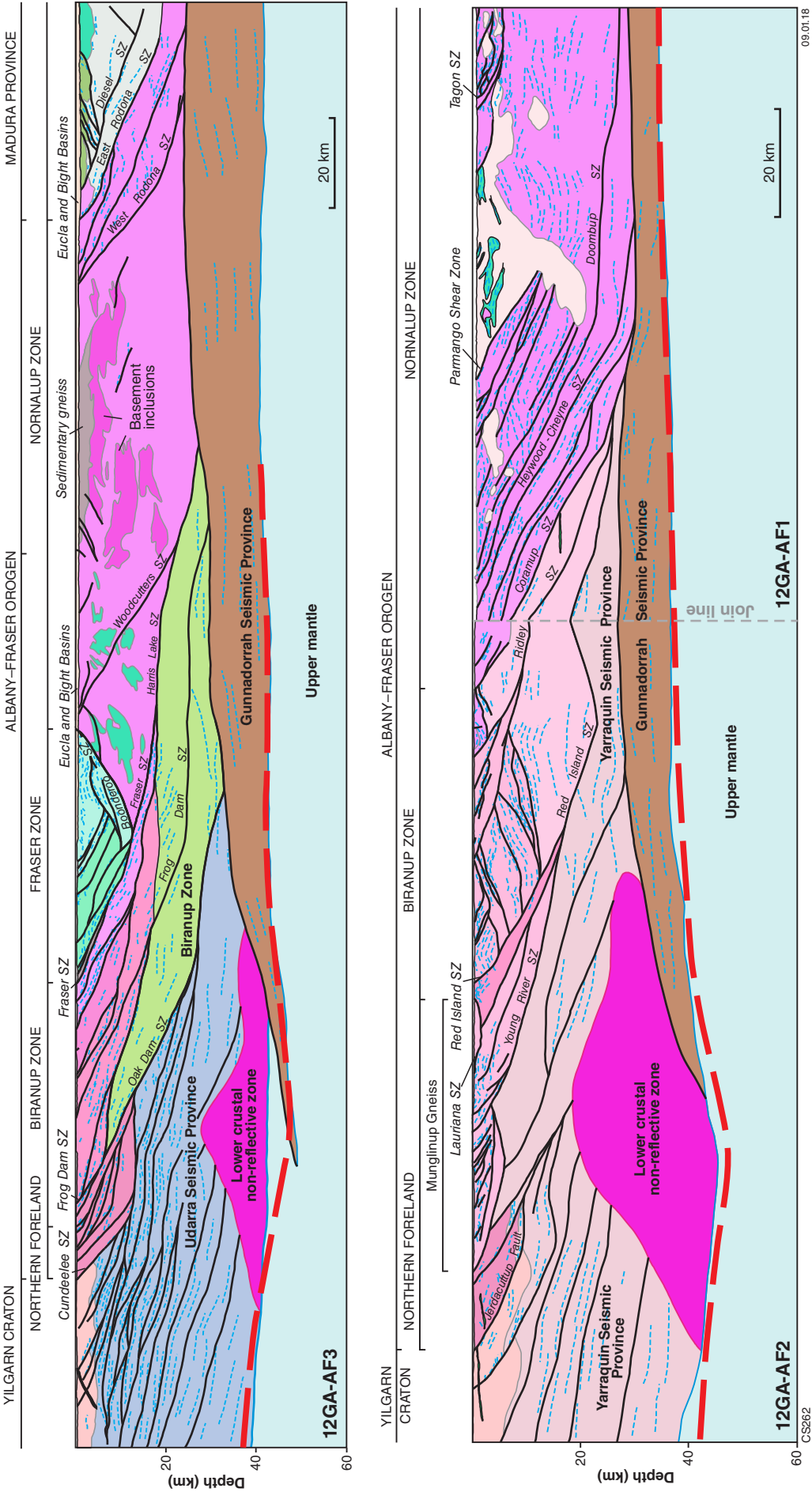
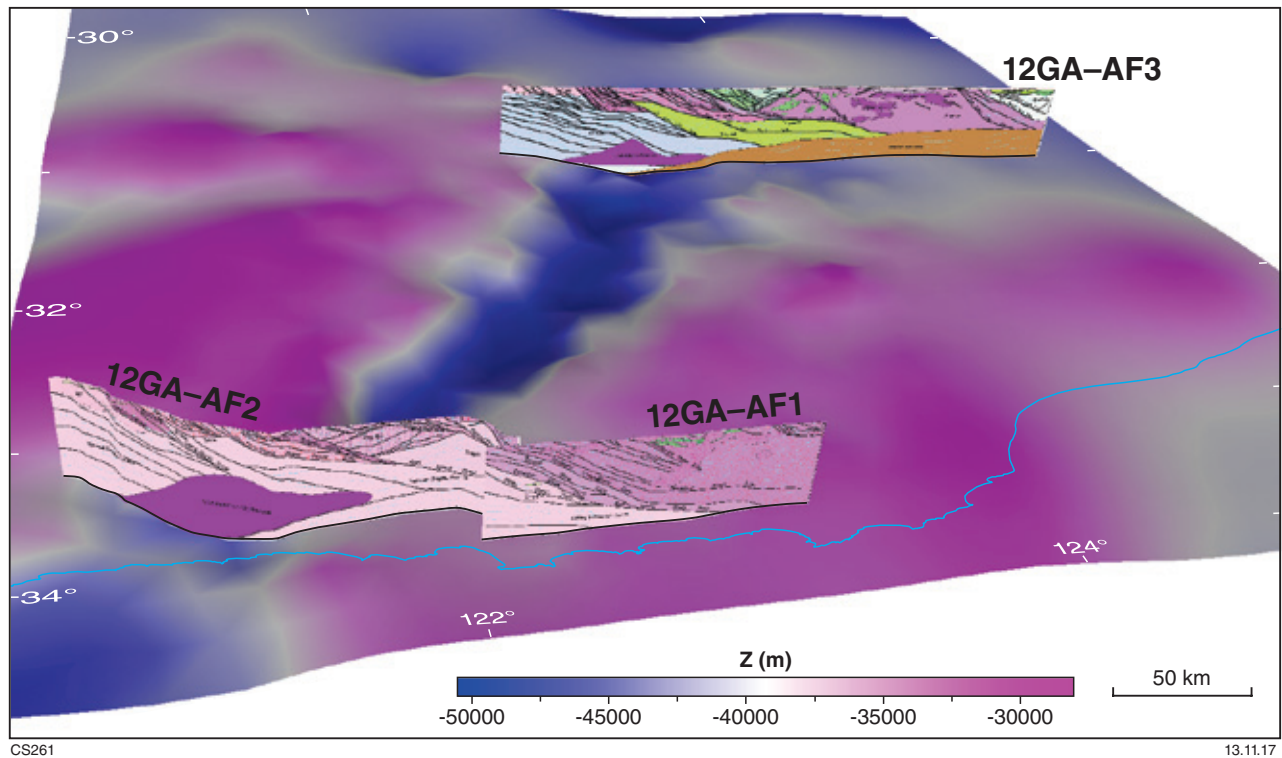


Figure 29. Moho depth from the interpolated map in Fig. 21b (red dashed line), overlain onto the interpreted active seismic profiles (from Spaggiari et al., 2014b). The general misfit is quite small. Note that the join between 12GA-AF2 and 12GA-AF1, which is situated at a bend on the seismic profile (Fig. 1), causes distorted geometries of the shear zones



**Figure 30.** Three-dimensional view showing the Moho trough from the southwest, and interpreted active seismic profiles 12GA-AF3, 12G-AF1, and 12G-AF1. The Moho surface in the image was produced from Moho picks on the active seismic profiles and from the receiver function results, placed at the actual pierce point of the incoming wave. This provides better definition of the slopes of the Moho topography

We speculate that this could imply another transition from a two-sided to a one-sided Moho geometry in the northeast, coincident with the termination of the gravity low. Additionally, the along-strike extent of the Rason Regional Gravity Low, and thus of the two-sided Moho trough, appears to correspond broadly to the along-strike extent of the Fraser Zone (see **Geometry of the Fraser Zone and its role in tectonic processes**).

The structure of the uppermost mantle beneath the east AFO may also have been important in defining where crustal features localize. In an east–west profile through a recent surface-wave tomography model at 32°N (Yoshizawa, 2014), a distinct step in the lithosphere–asthenosphere boundary is imaged at about 124°E (Kennett and Yoshizawa, 2016). Given the lateral resolution of this continent-wide model, this step could approximately coincide with the region of thickened crust, and may imply that the eastern end of the thick cratonic keel under the Yilgarn Craton, and the transition to hotter, upper mantle temperatures, could have been the reason for focused deformation in this region.

On a larger scale, the observed thickened crust in the east AFO could be part of a common pattern of increasing crustal thickness of the Yilgarn Craton towards its boundaries with surrounding Proterozoic orogens. However, this is highly speculative and, whereas crustal thickness within the Yilgarn Craton itself is well documented in regional studies (Reading et al., 2007; Yuan, 2015) and continent-wide compilations (Clitheroe

et al., 2000; Collins et al., 2003; Kennett et al., 2011), much less is known about the patterns of crustal thickness associated with the transition between the Yilgarn Craton and its adjacent orogens. The lower crustal configuration interpreted from active seismic profile 12GA-T1 showing a Moho offset and the Gunnadorrah Seismic Province dipping cratonwards beneath the Babool Seismic Province, which in turn underlies the Yamarna Terrane of the Yilgarn Craton (Occhipinti et al., 2014), is somewhat similar to that shown in the Yilgarn Craton – Officer Basin – Musgrave Province seismic profile (11GA-YO1; Neumann, 2013). In the southwestern part of the 11GA-YO1 profile, slightly thickened crust is associated with a Moho offset, and has been interpreted as a low angle, cratonward-dipping thrust fault beneath the Babool Seismic Province (Korsch et al., 2013). Although the geometry is similar to that shown in seismic profile 12GA-T1, the offset is well inboard of the craton margin edge, and has been interpreted to extend as far east as the southwestern edge of the Musgrave Province (Korsch et al., 2013). Seismic profile 11GA-YO1 shows that the Babool Seismic Province is dominated by northeast-dipping reflectors, whereas the underlying lower crust is dominated by subhorizontal reflectors, similar to those of the Gunnadorrah Seismic Province. This could be a common feature of the lower crust of craton margins and could be used to track perturbations and offsets. It also has implications for understanding the relevance of the Gunnadorrah Seismic Province to the east AFO and the adjoining Madura Province.



## Gravity forward models

To help clarify the relationship between the imaged Moho geometry and the Bouguer gravity anomalies (Fig. 2), we constructed simple 2D density models along the three CCP profile lines (A–A', B–B', C–C'; Fig. 23), and along two active seismic lines (12GA-AF1 and 12GA-AF2 combined, and 12GA-AF3; Fig. 31). We used the CCP results for the forward models because, unlike the Moho maps, the CCP profiles are representations of the acquired data that do not rely on spatial smoothing. Thus, the comparatively stronger short-wavelength Moho topography is likely to more accurately represent the real geometry than cross-sections through the interpolated maps. As discussed above, the active seismic profiles show gentler Moho topography, most likely due to apparent dip angles because the line orientations are not perpendicular to strike.

Two-dimensional gravity modelling was performed using gridded gravity observations with 2 km spacing, and measurements collected every 500 m along the active seismic profiles. SRTM topography (Shuttle Radar Topography Mission; Farr et al., 2007) was sampled every 1 km, and sections were modelled to a depth of 70 km using Oasis Montaj GM-SYS (v. 8.5, Geosoft Inc.). In order to avoid edge effects, modelled units were extended beyond the limits of the shown profiles. In order to limit the non-uniqueness of the obtained models, we started with simple models using average densities for mantle and crust, and then iteratively added features that were necessary to explain the gravity signals. Units that appear in several profiles were constrained to have a constant density between the different profiles. In principle, gravity modelling was performed iteratively by setting up a density model, calculating its gravity response, and then modifying this model to minimize the observed misfit to the observed gravity data.

To analyse the effect of a Moho geometry similar to that obtained from the CCP profiles, we initially performed a series of models that feature crust of uniform density (2.67 g/cm<sup>3</sup>) above a uniform mantle (3.2 g/cm<sup>3</sup>), using the Moho geometry constrained by active and passive seismic data (Fig. 31). Because low-density crust replaces higher-density mantle material along the region of thickened crust that has been imaged, the result is a pronounced gravity low for all profiles. Although to a first order this resembles the observed Rason Regional Gravity Low (Fig. 2), the gravity low resulting from these models exhibits larger amplitudes and is wider (or situated farther southeast) than the measured anomaly. These effects are likely due to the imprint of density variations between different crustal units.

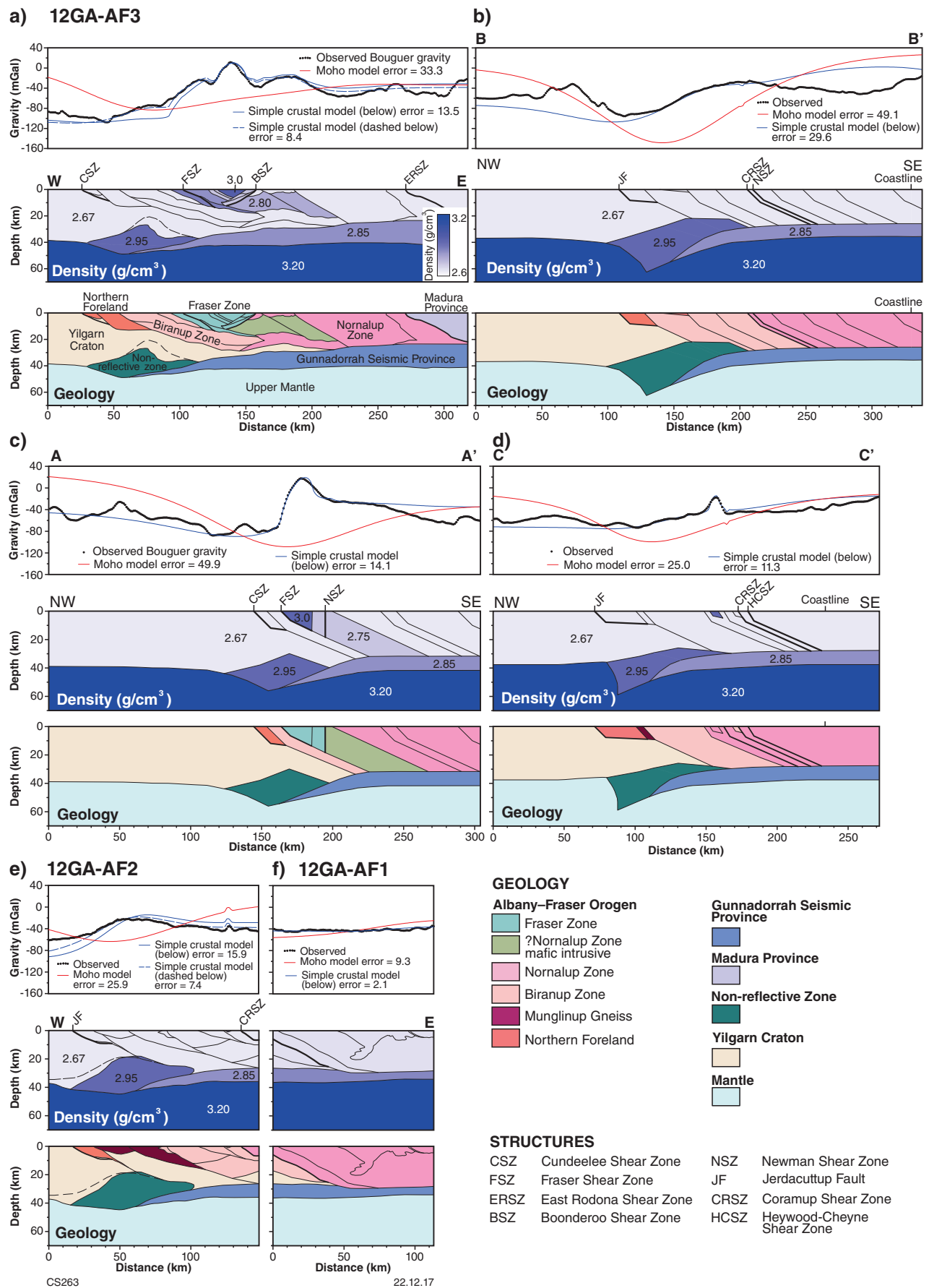
A substantially better fit can be achieved by adding a relatively small number of crustal units with different densities. The geometries of these units were taken from the interpreted bedrock geology map (Spaggiari, 2016) and the interpreted active seismic profiles (Spaggiari et al., 2014c). For profiles A–A' to C–C', we performed a simplified extrapolation of features from the active seismic lines. The two northernmost profiles (12GA-AF3 and A–A') cross the upper crustal Fraser Zone, a body dominated by dense metagabbroic rocks that are responsible for the gravity high that parallels the Rason Regional Gravity Low (Fig. 2). Inclusion of this unit in the forward model, with an assigned density of 3.0 g/cm<sup>3</sup>, reproduced the location and amplitude of the prominent gravity high.

In order to shift the gravity low produced by the Moho trough to the northwest, we added a dense crustal body (2.95 g/cm<sup>3</sup>) situated within the Moho trough to the profiles 12GA-AF3, A–A', B–B' and C–C'. This dense body is coincident with the non-reflective zones interpreted in the active seismic profiles 12GA-AF3 and 12GA-AF2 (Murdie et al., 2014; Spaggiari et al., 2014c), and may represent a mix of upper mantle and lower crustal material. In profile 12GA-AF2, which lies beyond the southwestern termination of the Rason Regional Gravity Low, this dense body was instrumental in producing the observed gravity high, despite the presence of thickened crust, which alone would invoke a gravity low. The observed gentler dip of the Moho trough along this profile, together with the denser lower crustal body, produced a satisfactory reconstruction of the gravity high.

In profiles B–B' and C–C', the body of denser lower crustal material interpreted to be associated with the non-reflective zones in active seismic profiles 12GA-AF2 and 12GA-AF3 was extended to the southeast, beyond the Northern Foreland and Biranup Zone. This geometry was not observed in the active seismic profiles, where the non-reflective zone occupied only the region of thickened crust and the Yilgarn Craton lower crust (Fig. 31). However, a more symmetric geometry can be achieved by slightly increasing the density of the Biranup Zone upper and middle crustal rocks in profiles B–B' (2.7 – 2.725 g/cm<sup>3</sup>) and C–C' (2.7 g/cm<sup>3</sup>).

Comparison of the observed gravity values on either side of the elongated anomalies corresponding to the Fraser Zone and the Rason Regional Gravity Low (Fig. 2) shows those in the east AFO are higher than those in the southeastern part of the Yilgarn Craton. The crust in the eastern part of the east AFO is not thinner than that of the southeastern Yilgarn Craton (Figs 19a, 21), which suggests a higher average density of east AFO crust. In the forward models, this higher bulk density is accounted for by the Gunnadorrah Seismic Province, a dense lower crustal body that is characterized in the active seismic profiles by moderately to strongly reflective crust and subhorizontal reflectors (Spaggiari et al., 2014c). Although the density models for profiles A–A' and B–B' do not require the presence of this unit, it was included for along-strike consistency.

**Figure 31.** (page 37) Crustal density forward models along the active seismic and CCP profiles: a) 12GA-AF3; b) B–B'; c) A–A'; d) C–C'; e) 12GA-AF2; f) 12GA-AF1. For each profile, the observed and modelled Bouguer gravity anomaly values are shown in the upper panel, the utilized density distributions in the centre panel, and the corresponding inferred geological units in the lower panel. The locations of the profiles are shown in Figures 1, 2, and 22. 'Moho model' refers to a simple model of uniform density crust (2.67 g/cm<sup>3</sup>) overlying a uniform mantle (3.2 g/cm<sup>3</sup>). Moho geometries for profiles A–A' to C–C' were taken from the CCP profiles (Fig. 23). Moho geometries for profiles 12GA-AF1–AF3 were taken from the active seismic profiles, as were lithological units, or their extrapolations (Fig. 29). Lithological units in all profiles were also taken from the active seismic profiles interpretations, or were extrapolated from these. Regions with the same geological provenance were given the same densities along strike. Nomenclature of shear zones and faults as per Figs 1, 22, and 23



In summary, the observed gravity signature of the east AFO (Fig. 31) can be reconstructed in gravity forward models by using the Moho topography provided from CCP and active seismic profiles and including three denser crustal bodies, the locations of which had already been recognized in the active profile interpretations. These are: 1) denser crustal material within the Moho trough, corresponding to the non-reflective zones in the active seismic profiles; 2) dense upper crust related to the Fraser Zone; and 3) a dense Gunnadorrah Seismic Province in the lower crust of the east AFO.

## Upper crustal structure

The preceding two sections focused on the Moho geometry and lower crustal units of the east AFO, for which the combination of receiver function analysis and gravity modelling proved to be useful tools. More detailed information about the structure of the upper crust is provided by the results of the ambient noise tomography (Figs 25–28), which are interpreted in conjunction with regional gravity anomalies (Figs 2, 30) and previous interpretations of the active seismic profiles (Spaggiari et al., 2014c). The observed surface-wave velocities do not show a systematic difference between the Yilgarn Craton and the east AFO, potentially because the east AFO crust contains large amounts of thermally and structurally reworked Archean material, particularly in the lower crust. Rather, we imaged a number of prominent anomalies that represent smaller-scale, upper crustal structures.

The most prominent high-velocity wavespeed anomaly in the study area (H1 in Figs 25, 27) is clearly associated with the Fraser Zone. The exhumed high-density metagabbroic rock assemblages in this area are, in all likelihood, responsible for both the observed increase in surface-wave velocities and the prominent gravity high. These mafic to ultramafic rocks are thus responsible for the elevated bulk crustal  $V_p/V_s$  ratios for stations located in the Fraser Zone (Fig. 19b). Since these values (1.77 – 1.8; Table 3) represent the entire crustal column beneath a seismic station, they likely underestimate  $V_p/V_s$  in Fraser Zone rocks, as these rocks make up only about one-third of the crustal column. The presence or absence of anomaly H1 in the velocity maps (Figs 25–28) allows an estimate to be made of the along-strike change of the depth extent of the Fraser Zone.

In active seismic profile 12GA-AF3, in the northernmost part of the study area, the Fraser Zone was imaged as a triangular pop-up-like structure with a maximum depth extent of about 13 km (Fig. 29; based on a conversion velocity of 6 km/s for 4.2 s two-way travel-time; Spaggiari et al., 2014c). At this locus, the clearly elevated group and phase velocities characteristic of Fraser Zone rocks are evident at periods of 2–9 s. At 10 s, they are still clearly recognizable in the group velocity map, but only faintly, if at all, in the phase velocities. This is explicable because the main sensitivity of phase velocities lies at somewhat greater depths than that of group velocities. Farther southwest, following the strike of the Fraser Zone and near its termination, a distinct high-wavespeed anomaly in both phase and group velocities at 10 s and longer remains, which indicates that Fraser Zone rocks penetrate deeper in this area, consistent with the co-located higher amplitudes of the gravity high (Fig. 2). A plot of dispersion

curves of three different example locations along the Fraser Zone (Fig. 32) corroborates this interpretation. At the northernmost location, which is situated where the Fraser Zone was intersected by active seismic line 12GA-AF3, heightened phase velocities are present down to a period of 9–10 s. Farther south, absolute velocities are higher and appear to penetrate deeper, which implies a thicker Fraser Zone and a possible along-strike difference in density and/or composition. A thicker Fraser Zone to the southwest could be geometric effect caused by differential exhumation. Although there are no known significant differences in the geological relationships in the southern and central parts of the Fraser Zone that indicate exposure of different crustal levels (Maier et al., 2016), it is feasible that the Fraser Zone is thicker in its southwestern part.

Anomaly H2 is situated to the west of the Fraser Zone gravity high, and at or just south of an intersection of a localized northwesterly trending gravity high with the otherwise continuous Rason Regional Gravity Low (Fig. 2). This local gravity high is where northwest-trending greenstone belts of the Eastern Goldfields Superterrane extend as far southeast as the Cundeelee Shear Zone (Fig. 2). The reworked portion of this crust within the east AFO most likely dips southeast beneath the shear zone (Spaggiari et al., 2014c). It is likely that the imaged area of elevated velocities at H2 represents these greenstone belts, and that their high-density rock assemblages are responsible for the observed elevated seismic wavespeeds.

The most prominent low-velocity anomaly imaged (L1) is situated in the northeastern part of the study area, where the eastern Nornalup Zone is overlain by Cretaceous carbonaceous shale and siltstone of the Bight Basin, in turn overlain by Eocene limestones of the Eucla Basin. Consistently slow group velocities are imaged down to the 9 s period (Fig. 25), which corresponds to a depth of at least 5 km, but more likely around 10 km (see sensitivity kernels in Fig. 15). This is surprising considering that drillcore data from the deeper part of the basin farther east (Spaggiari and Smithies, 2015) and a study of seismic resonance frequencies (Scheib et al., 2016) suggest that the depth to basement is only 300 m or less in the part of the Eucla Basin that falls in the study area. Thus, it is likely that the low velocities we obtained represent not only the sedimentary rocks, but also imply that the velocity of the uppermost basement rocks is also relatively slow.

Information on the lithological character and composition of this portion of the eastern Nornalup Zone is sparse. Potential field and drillcore data indicate considerable complexity, including the presence of metasedimentary rocks that have been intruded by the dominantly granitic rocks of the Recherche and Esperance Supersuites (Murdie et al., 2014; Spaggiari et al., 2014a; Spaggiari and Smithies, 2015). At longer periods, there is a transition to markedly faster velocities at 10 s, and then a return to a low-velocity anomaly towards 20 s (L3). Although this low-velocity anomaly should be regarded with some caution due to the reduced resolving capability of our tomographic inversion at the longest periods (Appendix Figs A1, A2), these observations suggest vertical transitions in the middle crust that were not previously recognized. Such transitions could, at least in part, explain the observation of strong reflectivity in localized, mostly upper crustal areas along active seismic profile 12GA-AF3. These



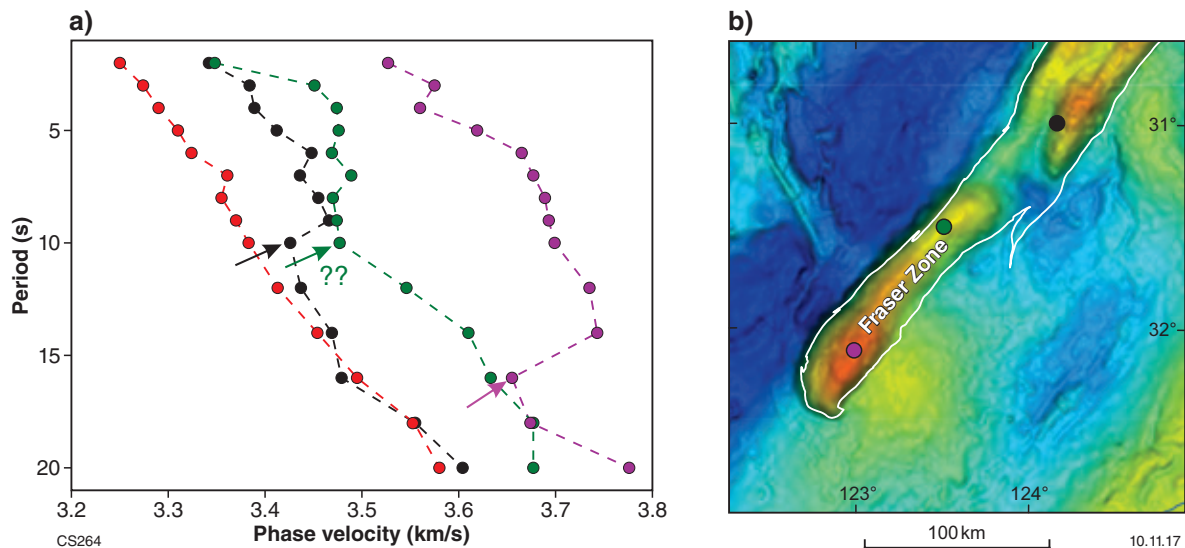


**Figure 32.** Average and selected phase velocity dispersion curves for the ALFREX array: a) Average phase velocity dispersion curve for the entire ALFREX array (red dots) and three single dispersion curves from different locations in the Fraser Zone (black, green, and purple dots). The three curves from the Fraser Zone clearly show elevated phase velocities at shallow depth, followed by a velocity decrease and then either a return to average values, or to a trend parallel to the average curve but at higher values. The points where these curves return to normal trends are marked with arrows. b) Extract of the Bouguer gravity image from Fig. 2, showing the locations of the three example phase velocities. The colours correspond to the dispersion curve colouring in panel a)

areas were interpreted to be metasedimentary rocks in the uppermost crust, underlain by basement inclusions within younger granites (Spaggiari et al., 2014c). Fe-rich and Mn-rich metasedimentary rocks have been reported from exploration drillholes in this area, which is consistent with this interpretation (Smit, 2009; Stephens, 2000). Moreover, these rocks appear to be similar to rocks intersected in drillholes at the NSD prospect farther north (Tillick, 2011) and, together with the area defined by the L1 slow group velocity anomaly, might indicate considerable lateral and perhaps depth extent of these rock packages. The presence of these upper crustal metasedimentary rocks that have been intruded by dominantly granitic rocks of the Recherche and Esperance Supersuites is also consistent with the vertical crustal transition indicated by the change in velocities (L1 to L3).

Another low-velocity anomaly was retrieved in the Cape Arid area, in the far southeastern corner of the study area (L2; Figs 25–28). The anomaly, which is present throughout nearly all periods, lies beyond the eastern end of active seismic profile 12GA-AF1, which shows a change in the seismic character of the upper and lower crust at its far eastern end (Spaggiari et al., 2014c; Waddell et al., 2015). The location of the low-velocity anomaly corresponds to the regional minimum crustal thickness imaged with receiver function data (Figs 19a, 21). Without further constraints, however, we cannot determine the origin of this enigmatic anomaly.

Whereas most of the obtained upper crustal wavespeed anomalies have an expression in the Bouguer gravity anomaly map, it is also instructive to examine the gravity anomalies that do not have an obvious expression in the velocity maps. The lack of a corresponding surface-wave velocity expression associated with the Rason

Regional Gravity Low is to be expected because that low is associated with locally thickened crust just west of the Fraser Zone. The gravity high to the southwest of the Rason Regional Gravity Low (Fig. 2) is most likely associated with high-density rocks in the lower crust (see **Gravity forward models**). Finally, the semicircular southeastward extension of the gravity high in the southern part of the Fraser Zone that has been attributed to a middle to lower crustal high-velocity body in forward models of the region (Brisbout, 2015) is not observed in our velocity maps as they cover only roughly the upper half of the crust. This supports the interpretation that it is indeed a deep feature (Brisbout, 2015).

## Inferences on tectonic processes that formed the Albany–Fraser Orogen

The observed Moho geometry beneath the east AFO has implications for understanding the evolution of the orogen. The eastern side of the Moho trough shows a continuous westward dip, at a relatively constant angle along the entire length of the region of the east AFO that was examined, whereas the geometry of the western side has been shown to be variable. There appears to be no indication of a continuation of the Moho phase to depths beyond the tip of the V in profiles A–A' and B–B' (Fig. 23), whereas a very faint continuous negative phase in profile C–C' could be interpreted as a continuing (albeit considerably fainter) eastern flank of the Moho trough. This is, however, far from compelling evidence, and could also be explained either by noise on the receiver function traces or by a faint phase of different origin. Importantly, we see no indication of a second Moho above the downgoing eastern flank of the



Moho trough in profile C–C'. There are two principal ways to interpret our observations: they might represent a fossil subduction zone, or underthrusting involving indentation of a continental crustal wedge. These two scenarios are discussed below.

## Subduction zone scenario

If we interpret the imaged Moho geometry as a relic of an ancient subduction zone, slab material should be present down dip of the termination of the Moho phase of the eastern flank (Fig. 23), even if we invoke slab breakoff after subduction cessation. In subduction zones, the strong Moho phase dipping downwards is caused by the velocity contrast between the downgoing oceanic crust and the underlying lithospheric mantle. If this crustal material has, however, been modified by exposure to and subsequent thermal and chemical modification by surrounding mantle material and high P–T conditions, this velocity contrast could have vanished and the slab would be invisible to our imaging. Examples from receiver function imaging from active oceanic (Pearce et al., 2012) or continental (Schneider et al., 2013) subduction show that downgoing crustal material is usually imaged with a pair of anomalies; a negative one representing the step from high mantle velocities in the slab to the lower crustal velocities, and a positive one at the transition between oceanic crust and the overlying mantle wedge. This pair of parallel converters shows up as a direct continuation of the lower plate Moho. Although the slabs in these studies in all likelihood extend to deeper depths, these imaged converters vanish at depths between 60 and 100 km, which has been ascribed to mineral reactions, most importantly eclogitization (Wittlinger et al., 2009; Bostock, 2013), that increase the density and seismic velocity of the downgoing crustal material until it becomes indistinguishable from the surrounding mantle. The different depths at which the phase disappears can be due to different reaction rates, or different P–T conditions.

If the structure imaged below the east AFO represents a fossil subduction zone, all features relating to the thermal structure of a subduction zone should long have been eradicated, but chemical structure, such as regions of metamorphosed material, could have been preserved through time. If such a stagnant slab had been exposed to mantle conditions for about 1.1 Ga, from which time major tectono-thermal activity in the AFO had ceased, mineral reactions such as eclogitization would have had ample time to be completed, whereas in active settings they are often retarded by ongoing subduction. This could explain the rather shallow termination of the Moho phase (Fig. 23).

The absence of a second Moho phase above the dipping Moho on the western flank (i.e. upper plate in a subduction scenario; profile C–C' in Fig. 23), as well as the lack of the positive phase above the downgoing oceanic crust Moho, could be explained with a high degree of serpentinization in the mantle wedge (e.g. Guillot et al., 2000; Bostock et al., 2002). This process, which occurs due to fluid influx into the mantle wedge from the dehydrating slab, leads to a substantial increase of  $V_p/V_s$  ratio and thus a decrease in shear wave speeds throughout the mantle wedge, which can diminish the velocity contrast between the mantle wedge and the overlying crust, as well as the underlying oceanic crust. In some cases, mantle wedge serpentinization is so pervasive that a sign-flip in the imaged upper plate Moho

has been observed (Bostock et al., 2002), indicating an increase in shear wave velocity from the mantle wedge into the overlying continental lower crust. In this scenario, the density of serpentinized mantle wedge material is still significantly higher than that of continental crust. Thus, the high-density material within the Moho trough that we retrieved from the gravity models could be interpreted as mantle wedge material, which would also explain the absence of a second Moho phase in profile C–C'.

However, this mantle wedge material should have a clear signature in the distribution of retrieved  $V_p/V_s$  ratios, which only holds true for the northern part of the study area (Fig. 19b). There, however, the elevated  $V_p/V_s$  ratios are more likely to represent the exhumed rocks of the Fraser Zone, rather deeper features. Moreover, we have not conclusively imaged a downgoing slab, and the presence of such a slab does not fit well with the geometry of the mantle keel of the adjacent Yilgarn Craton, which extends to depths of at least 200 km (e.g. Kennett et al., 2013; Yoshizawa, 2014), and which must have been present during AFO tectonism. The surface-wave tomography studies of Kennett et al. (2013) and Yoshizawa (2014) show that this keel is present throughout the Yilgarn Craton, and thus would be expected to terminate immediately west or northwest of our study area. There simply would not have been enough space to accommodate a major subduction zone, which in turn implies that any indication of a preserved slab should be farther outboard, to the southeast. Moreover, geochemical and isotope data indicate that reworked Archean crust and Paleoproterozoic intrusions extend well beyond the imaged Moho trough (Kirkland et al., 2014; Smithies et al., 2015). Furthermore, basin analysis and structural considerations, and the absence of any continental-arc or subduction-related rocks, argue against a subduction setting within the AFO, and beneath the craton margin (Smithies et al., 2015; Spaggiari and Smithies, 2015; Spaggiari et al., 2015). However, based on our images alone we cannot exclude the possibility of short-lived failed subduction that stalled and terminated soon after initiation by impingement of the slab onto the Yilgarn upper mantle keel.

## Crustal wedge indentation scenario

Alternatively, the geometry of the Moho that we imaged could be interpreted within the framework of crustal wedge indentation, sometimes referred to as 'crocodile tectonics' (Meissner, 1989). This would imply that the eastern side of the east AFO was split into an overthrust upper crustal 'flake' (Oxburgh, 1972) and an underthrust lower crustal part (the Gunnadorrah Seismic Province) in a convergent setting. For such a process, which is commonly observed at accretionary margins (Snyder and Goleby, 2016), there is no need for a downward continuation of the imaged west-dipping Moho. This scenario also fits with existing models for the tectonic evolution of the AFO.

The geometry of crustal units interpreted in the active seismic profiles (Spaggiari et al., 2014c), especially profile 12GA-AF3, is strongly indicative of such a process, where a middle crustal unit from the Yilgarn (western) side, the Udarra Seismic Province, appears to have been wedged between the Biranup Zone and the Gunnadorrah Seismic Province (Fig. 29). This Yilgarn-side tectonic wedge could have separated the upper crustal flake from the lower

crust by horizontal indentation during compression. This configuration is not located at the transition between the east AFO and the accreted oceanic arc (the Loongana Arc of the Madura Province), but lies inboard between the Yilgarn Craton and its reworked counterparts within the AFO, and hence implies stress transfer through the craton margin itself.

If crustal wedge indentation is invoked, the absence of a double Moho and the presence of high-density material within the Moho trough cannot be explained by serpentinization of mantle wedge material. These areas, which coincide with non-reflective zones in the interpreted active seismic profiles, could then represent high-density crustal or mixed-lithology rocks (e.g. continental lower crust heavily modified and/or intruded by the underlying mantle rocks). Such processes have been interpreted from geochemical and isotopic data from gabbroic and ultramafic Fraser Zone rocks, where mantle melts have acquired small volumes of crustal material that subsequently ponded in staging chambers, prior to intrusion (Maier et al., 2016). It is feasible that the non-reflective zones contain remnants from a similar or related process. The intrusion of mafic mantle rocks into lower crustal material could thus also contribute to the elevated  $V_p/V_s$  ratios observed at stations throughout the Fraser Zone, and also explain the observed high  $V_p/V_s$  ‘tail’ southwest of the termination of the Fraser Zone (Fig. 19b). If the non-reflective zones have similar high  $V_p/V_s$  ratios, their  $V_s$  values might be comparable to the surrounding crust, although rock density and thus  $V_p$  are clearly elevated. This could explain why there is no other signature (i.e. no additional imaged discontinuity) of this material in the receiver function data beyond the  $V_p/V_s$  ‘tail’ described above.

## Implications for the tectonic evolution of the Albany–Fraser Orogen

Both of the structural scenarios described above require an extended period of crustal shortening. However, prior to Stage I tectonism the AFO appears to have been predominantly in an extensional environment associated with continental rifting and basin formation (Spaggiari et al., 2015). Known exceptions to this were the Tropicana Event, during which the Tropicana Zone was thrust over the Yamarna Terrane of the Yilgarn Craton at c. 2520 Ma (Occhipinti et al., 2014, 2017), and the c. 1680 Ma Zanthus Event, which produced northwesterly trending folds in migmatitic rocks in the Biranup Zone (Kirkland et al., 2011). In the Tropicana Zone, an imbricate fan system is interpreted to have been produced as the Tropicana and Hercules Gneisses were thrust northwestward along a crustal ramp (Occhipinti et al., 2017). This ramp may be an along-strike continuation of the Moho trough imaged in this study, although that would suggest that the Moho trough is an exceptionally long-lived feature, and one that has controlled the crustal architecture of the east AFO over the duration of its evolution.

Compressional regimes known to have affected most of the AFO occurred during both Stages I (1330–1260 Ma) and II (1225–1140 Ma) of the Albany–Fraser Orogeny (Clark et al., 2000; Spaggiari et al., 2011, 2014a,c), although whether the compressional structures formed during Stage I or II, or were reactivated, is not always clear. Stage I is interpreted to have been triggered by the accretion of the Loongana oceanic arc by c. 1330 Ma, the age of the oldest granitic rocks of the Recherche Supersuite (Smithies et al., 2015; Spaggiari et al., 2015). It is therefore feasible that the crustal wedge formed either during this event, or sometime after it.

The presence or absence of the Fraser Zone correlates remarkably well with the geometry of the Moho trough. This suggests that the lower crustal geometry imaged in the northern part of the study area, where the Yilgarn-side forms the east-dipping part of the Moho trough, could have controlled the position of the Fraser Zone and facilitated its emplacement. If this is the case, the Moho trough must either pre-date or be contemporaneous with the emplacement and exhumation of the Fraser Zone (see **Geometry of the Fraser Zone and its role in tectonic processes**). Moreover, it is interesting to observe that the Moho trough marks the boundary between a region of widespread Mesoproterozoic magmatism to the east, and a region of minimal intrusive activity to the west. The Mesoproterozoic intrusions belong to the 1330–1280 Ma Recherche and 1200–1140 Ma Esperance Supersuites (Smithies et al., 2015; Spaggiari et al., 2014a), and the 1192–1125 Ma Moodini Supersuite in the adjoining Madura Province (Spaggiari and Smithies, 2015). If the westward cessation of intrusive activity is indeed due to the presence of the Moho trough, or the processes responsible for its formation, then the onset time of the Esperance and Moodini Supersuite intrusions is the latest possible time when the trough must have already been in place.

The process of crustal wedge indentation, which is our preferred interpretation for the results obtained in this study, has been invoked and imaged in several currently active orogens (e.g. Teixell, 1998; TRANSALP working group, 2002; Moore and Wiltschko, 2004). Although the models proposed for these orogens vary in detail, the general pattern of an upper plate crustal wedge splitting the lower plate crust, usually between the middle and lower crust, is common to all of them. According to Moore and Wiltschko (2004), the lower crustal sliver thus separated from the lower plate crust, together with the underlying lithospheric mantle, descends due to ongoing plate convergence allowing mineral reactions such as eclogitization to occur, before eventual delamination. Active seismic images from other craton margins around the world (e.g. Lewry et al., 1994; Bayer et al., 2002; Hajnal et al., 2005; Zhang et al., 2014) show thickened crust compared to the interior of the craton, and younger upper crust that has overthrust the craton, corresponding to the ‘flake’ in our model. However, a downward dipping lower crustal unit such as that observed in the east AFO is lacking. This could imply that orogenesis in those cases was completed by the delamination of the lower crust, due to eclogitization, and also possibly due to the inherently higher densities of Proterozoic and Phanerozoic lithospheric mantle roots (Poudjom Djomani et al., 2001).

The AFO could thus represent an incomplete craton margin orogen that retained its lower crustal sliver, possibly due to a limited amount of convergence.

The lower crustal sliver, represented by the Gunnadorrah Seismic Province in the east AFO, may have acquired its special properties (high density, possibly high  $V_p/V_s$  ratio) after its initial emplacement. Spaggiari and Smithies (2015) proposed that the Gunnadorrah Seismic Province may have been the source area for the voluminous granitic and gabbroic intrusions of the Esperance and Moodini Supersuites into the upper crust. If this were the case the Gunnadorrah Seismic Province would be dominated by mafic restites (i.e. the remaining material after these intrusions took place) and would thus be denser than normal continental lower crust.

## Geometry of the Fraser Zone and its role in tectonic processes

The position of the western part of the Fraser Zone directly above the deepest point of the Moho trough, and its absence farther south where the geometry of the Moho trough is one-sided, is notable and suggests a causal link between the two features. The current model for the emplacement of the Fraser Zone involves a southeast-dipping crustal ramp interpreted to have controlled its location and facilitated its exhumation (fig. 23 in Maier et al., 2016). Despite Fraser Zone rocks being predominantly mafic (Smithies et al., 2014), geochemical and isotopic constraints show that they are clearly not of oceanic-arc origin (Fletcher et al., 1991; Kirkland et al., 2014; Smithies et al., 2014), contrary to what was proposed in Condie and Myers (1999).

The southeast dip of the Moho trough on the Yilgarn side that is imaged in profiles A–A' and B–B' (Fig. 23) could represent the lower end of this crustal ramp. If that is the case, the southwestern termination of this ramp near the inferred trace of the Ida Fault and terrane boundary may also have controlled the southwestern extent of the Fraser Zone, since emplacement would have been more difficult or perhaps impossible in the absence of the ramp. Based on the regional Bouguer gravity map, we speculate that the same circumstances may be present at the northeastern termination of the Fraser Zone, which is outside the study area. If the Rason Regional Gravity Low is inferred as a marker for the presence of southeast-dipping Yilgarn crust and the Moho trough, then the northeastern termination of the Fraser Zone may also correspond to where the Moho trough could terminate. The short active seismic profile (12GA-T1; Occhipinti et al., 2014) just north of this area (outside our study area) shows the presence of an east-under-west geometry, which is consistent with this theory. However, more research in this area is needed to test these interpretations.

The eastern hinge point of the Moho trough migrates to the east as the trough widens to the north, within the study area (Figs 21, 23), which together could be a response to crustal sagging due to the load of the high-density Fraser Zone rocks as they were exhumed (Figs 29, 31). A positive gravity anomaly is coincident with the Fraser Zone (Fig. 2) so it is clear that full isostatic compensation of this load has not occurred. A partial compensation of the load by crustal thickening, however, may have been achieved.

## Conclusions

The recording and analysis of passive seismic data from a 70-station array deployed in the east AFO has led to production of the first detailed maps of crustal thickness,  $V_p/V_s$  ratio, and upper crustal surface-wave velocities for the region. In addition, several CCP profiles show the details of regional Moho topography.

The crustal thickness maps produced show a belt of significantly thickened crust (~10–15 km thicker than in its surroundings), forming a V-shaped Moho trough that widens northwards. CCP profiles show a geometric change from a two-sided, symmetric trough in the northeast to a one-sided, asymmetric step-like configuration in the southwest. In the northeast, the deepest point of the Moho trough is located beneath metamorphic rocks of the Fraser Zone, which have clear signatures in both the  $V_p/V_s$  and surface-wave velocity maps. Combining these results with gravity forward models shows that the regional gravity pattern, which features two northeast-trending parallel anomalies of opposite sign along most of the east AFO, can be explained by the presence of the Moho trough, the upper crustal Fraser Zone, and the presence of high-density rocks at lower crustal depths within the Moho trough itself. The high-density rocks most likely correspond to non-reflective zones that are prominent in active seismic profile interpretations.

Taken together, these results are most likely indicative of a process of horizontal wedge indentation during a compressive period, probably during the Mesoproterozoic. Due to the rather limited amount of shortening, the lower crustal sliver, which would normally be expected to delaminate after the termination of wedge indentation, has survived in the east AFO and is interpreted to correspond to the Gunnadorrah Seismic Province. The southeast-dipping, Yilgarn-side lower crust could be an expression of the ramp structure that was inferred to have facilitated the exhumation and emplacement of the Fraser Zone intrusive and metamorphic rock assemblages.

## Acknowledgements

We thank everybody who helped out on the numerous field campaigns (R Addenbrooke, A Arcidiaco, U Azad, J Byrne, S Fanning, Q Li, G Luton, J Maina, M Mustać, T Pejić, P Sandow, K Smith, J Stephenson, C Zirk). We are grateful for the use of the ANSIR instrument pool for the seismometers and recording units used in this project. This research was funded by ARC Linkage Grant LP130100413.

## References

- Aitken, ARA, Betts, PG, Young, DA, Blankenship, DD, Roberts, JL and Siegert, MJ 2016, The Australo-Antarctic Columbia to Gondwana transition: Gondwana Research, v. 29, no. 1, p. 136–152.
- Ammon, CJ 1991, The isolation of receiver effects from teleseismic P waveforms. Bulletin of the Seismological Society of America, v. 81 (6), p. 2504–2510.
- Arroucau, P, Rawlinson, N and Sambridge, M 2010, New insight into Cainozoic sedimentary basins and Palaeozoic suture zones in southeast Australia from ambient noise surface wave tomography: Geophysical Research Letters, v. 37(7), p. 1–6.



- Balfour, NJ, Salmon, M and Sambridge, M 2014, The Australian Seismometers in Schools Network: Education, Outreach, Research, and Monitoring: *Seismological Research Letters*, v. 85 (5), p. 1063–1068.
- Bayer, U, Grad, M, Pharaoh, TC, Thybo, H, Guterch, A, Banka, D, Lamarche, J, Lassen, A, Lewerenz, B, Scheck, M and Marotta, AM 2002, The southern margin of the East European Craton: New results from seismic sounding and potential fields between the North Sea and Poland: *Tectonophysics*, v. 360, p. 301–314.
- Bensen, GD, Ritzwoller, MH, Barmin, MP, Levshin, AL, Lin, FC, Moschetti, MP, Shapiro, NM and Yang, Y 2007, Processing seismic ambient noise data to obtain reliable broad-band surface wave dispersion measurements: *Geophysical Journal International*, v.169 (3), p. 1239–1260, doi:org/10.1111/j.1365-246X.2007.03374.x.
- Bensen, GD, Ritzwoller, MH and Shapiro, NM 2008, Broadband ambient noise surface wave tomography across the United States: *Journal of Geophysical Research*, v. 113 (B05306), 21p., doi:org/10.1029/2007JB005248.
- Beyreuther, M, Barsch, R, Krischer, L, Megies, T, Behr, Y and Wassermann, J 2010, ObsPy: A Python Toolbox for Seismology: *Seismological Research Letters*, v. 81(3), p. 530–533, doi:org/10.1785/gssrl.81.3.530.
- Blewett, RS, Czarnota, K, Henson, PA 2010, Structural-event framework for the eastern Yilgarn Craton, Western Australia, and its implications for orogenic gold: *Precambrian Research*, v. 183, p. 203–229.
- Bostock, MG 2013, The Moho in subduction zones: *Tectonophysics*, v. 609, p. 547–557.
- Bostock, MG, Hyndman, RD, Rondenay, S and Peacock, SM 2002, An inverted continental Moho and serpentinization of the 576 forearc mantle: *Nature*, v. 417, p. 536–538.
- Brisbourn, L 2015, Determining crustal architecture in the east Albany–Fraser Orogen from geological and geophysical data: *Geological Survey of Western Australia, Report 152*, 52p.
- Chen, Y, Niu, F, Liu, R, Huang, Z, Tkalčić, H, Sun, L and Chan, W 2010, Crustal structure beneath China from receiver function analysis: *Journal of Geophysical Research*, v. 115 (B03307), 22p., doi:org/10.1029/2009JB006386.
- Chevrot, S and Van der Hilst, R 2000, The Poisson ratio of the Australian crust: Geological and geophysical implications: *Earth and Planetary Science Letters*, v. 183 (1–2), p. 121–132, doi:org/10.1016/S0012-821X(00)00264-8.
- Clark, C, Kirkland, CL, Spaggiari, CV, Oorschot, C, Wingate, MTD and Taylor, RJ 2014, Proterozoic granulite formation driven by mafic magmatism: An example from the Fraser Range Metamorphics, Western Australia: *Precambrian Research*, v. 240, p. 1–21.
- Clark, DJ, Hensen, BJ and Kinny, PD 2000, Geochronological constraints for a two-stage history of the Albany–Fraser Orogen, Western Australia: *Precambrian Research*, v. 102, no. 3, p. 155–183.
- Clietheroe, G, Gudmundsson, O and Kennett, BLN 2000, The crustal thickness of Australia: *Journal of Geophysical Research*, v. 105, no. B6, p. 13697–13713.
- Collins, CDN, Drummond, BJ and Nicoll, MG 2003, Crustal thickness patterns in the Australian continent: *Geological Society of America Special Papers*, v. 372, p. 121–128.
- Condie, KC and Myers, JS 1999, Mesoproterozoic Fraser Complex: geochemical evidence for multiple subduction-related sources of lower crustal rocks in the Albany–Fraser Orogen, Western Australia: *Australian Journal of Earth Sciences*, v. 46, p. 875–882.
- Dentith, MC, Evans, S, Thiel, S, Gallardo, L, Joly, A and Romano, SS 2013, A magnetotelluric traverse across the southern Yilgarn Craton: *Geological Survey of Western Australia Report 121*, 43p.
- Dueker, KG and Sheehan, AF 1997, Mantle discontinuity structure from midpoint stacks of converted P to S waves across the Yellowstone hotspot track: *Journal of Geophysical Research*, v. 102(B4), p. 8313–8327, doi:org/10.1029/96JB03857.
- Eberhart-Phillips, D 1986, Three-dimensional velocity structure in northern California Coast Ranges from inversion of local earthquake arrival times: *Bulletin of the Seismological Society of America*, v. 76 (4), p. 1025–1052.
- Farr, TG, Rosen, PA, Caro, E, Crippen, R, Duren, R, Hensley, S, Koblrick, M, Paller, M, Rodriguez, E, Roth, L, Seal, D, Shaffer, S, Shimada, J, Umland, J, Werner, M, Oskin, M, Burbank, D, Alsdorf, D 2007, The Shuttle Radar Topography Mission: *Reviews of Geophysics*, v. 45 (2), RG2004, doi:org/10.1029/2005RG000183.
- Fitzsimons, ICW 2003, Proterozoic basement provinces of southern and southwestern Australia and their correlation with Antarctica: *Geological Society of London Special Publication*, v. 206, p. 93–130.
- Fletcher, IR, Myers, JS and Ahmat, AL 1991, Isotopic evidence on the age and origin of the Fraser Complex, Western Australia: a sample of Mid-Proterozoic lower crust: *Chemical Geology: Isotope Geoscience*, v. 87, p. 197–216.
- Fraser, AR and Pettifer, GR 1980, Reconnaissance gravity surveys in WA and SA, 1969–1972: *Australian Bureau of Mineral Resources, Geology and Geophysics Bulletin 196*, 60p.
- Goleby, BR, Blewett, RS, Fomin, T, Fishwick, S, Reading, AM, Henson, PA, Kennett, BLN, Champion, DC, Jones, LEA, Drummond, BJ and Nicoll, M 2006, An integrated multi-scale 3D seismic model of the Archaean Yilgarn Craton, Australia: *Tectonophysics*, v. 420, p. 75–90.
- Gorbatov, A, Saygin, E and Kennett, BLN 2013, Crustal properties from seismic station autocorrelations: *Geophysical Journal International*, v. 192 (2), p. 861–870, doi:org/10.1093/gji/ggs064.
- Guillot, S, Hattori, KH and De Sigoyer, J 2000, Mantle wedge serpentinization and exhumation of eclogites: Insights from eastern Ladakh, northwest Himalaya: *Geology*, v. 28, p. 199–202.
- Hajnal, Z, Lewry, J, White, D, Ashton, K, Clowes, R, Stauffer, M, Gyorfi, I and Takacs, E 2005, The Sask Craton and Hearne Province margin: seismic reflection studies in the western Trans-Hudson Orogen: *Canadian Journal of Earth Sciences*, v. 42, p. 403–419.
- Herrmann, RB 2013, Computer Programs in Seismology: An evolving tool for instruction and research: *Seismological Research Letters*, v. 84, p. 1081–1088.
- Kennett, BLN, Engdahl, ER and Buland, R 1995, Constraints on seismic velocities in the Earth from travel times: *Geophysical Journal International*, v. 122, p. 108–124, doi:org/10.1111/j.1365-246X.1995.tb03540.x.
- Kennett, BLN, Fichtner, A, Fishwick, S and Yoshizawa, K 2013, Australian Seismological Reference Model (AuSREM): mantle component: *Geophysical Journal International*, v. 187, p. 946–958.
- Kennett, BLN, Salmon, M, Saygin, E and AusMoho Working Group 2011, AusMoho: the variation of Moho depth in Australia: *Geophysical Journal International*, v. 187, no. 2, p. 946–958.
- Kennett, BLN, Saygin, E and Salmon, M 2015, Stacking autocorrelations to map Moho depth with high spatial resolution in southeastern Australia: *Geophysical Research Letters*, 42 (18), p. 7490–7497, doi:org/10.1002/2015GL065345.
- Kennett, BLN and Yoshizawa, K 2016, Lithospheric discontinuities beneath Australia: interaction of large-scale and fine scale structure: *Geophysical Research Abstracts*, EGU General Assembly.
- Kirkland, CL, Spaggiari, CV, Pawley, MJ, Wingate, MTD, Smithies, RH, Howard, HM, Tyler, IM, Belousova, EA and Poujol, M 2011, On the edge: U–Pb, Lu–Hf, and Sm–Nd data suggests reworking of the Yilgarn Craton margin during formation of the Albany–Fraser Orogen: *Precambrian Research*, v. 187, p. 223–247.
- Kirkland, CL, Spaggiari, CV, Smithies, RH and Wingate, MTD 2014, Cryptic progeny of craton margins: geochronology and isotope geology of the Albany–Fraser Orogen with implications for evolution of the Tropicana Zone, in Albany–Fraser Orogen seismic and magnetotelluric (MT) workshop 2014: extended abstracts compiled by CV Spaggiari and IM Tyler: *Geological Survey of Western Australia, Record 2014/6*, p. 89–101.



- Korsch, RJ, Blewett, RS, Pawley, MJ, Carr, LK, Hocking, RM, Neumann, NL, Smithies, RH, Quentin de Gromard, R, Howard, HM, Kennett, BLN, Aitken, ARA, Holzschuh, J, Duan, J, Goodwin, JA, Jones, T, Gessner, K and Gorczyk, W 2013, Geological setting and interpretation of the southwest half of deep seismic reflection line 11GA-YO1: Yamarna Terrane of the Yilgarn Craton and the western Officer Basin, in *Yilgarn Craton - Officer Basin - Musgrave Province seismic and MT workshop* edited by NL Neumann: Geoscience Australia, Symonston, Australian Capital Territory, Record 2013/28, p. 24–50.
- Langston, C 1979, Structure under Mount Rainier, Washington, inferred from teleseismic body waves: *Journal of Geophysical Research*, v. 84 (B9), 4749–4762, doi:org/10.1029/JB084iB09p04749.
- Levshin, AL, Ratnikova, L and Berger, J 1992, Peculiarities of surface-wave propagation across central Eurasia: *Bulletin of the Seismological Society of America*, v. 82 (6), p. 2464–2493, <www.bssaonline.org/cgi/content/abstract/82/6/2464>.
- Levshin, AL and Ritzwoller, MH 2001, Automated detection, extraction, and measurement of regional surface waves: Pure and applied geophysics, v. 158, (8), p. 1531–1545, doi:10.1007/PL00001233.
- Lewry, J, Hajnal, Z, Green, A, Lucas, SB, White, D, Stauffer, MR, Ashton, KE, Weber, W and Clowes, R 1994, Structure of a Paleoproterozoic continent-continent collision zone: a LITHOPROBE seismic reflection profile across the Trans-Hudson Orogen, Canada: *Tectonophysics*, v. 232, p. 143–160.
- Ligorria, J.P and Ammon, CJ 1999, Iterative deconvolution and receiver-function estimation: *Bulletin of the Seismological Society of America*, v. 89 (5), p. 1395–1400.
- Lin, FC, Moschetti, MP and Ritzwoller, MH 2008, Surface wave tomography of the western United States from ambient seismic noise: Rayleigh and Love wave phase velocity maps: *Geophysical Journal International*, v. 173 (1), p. 281–298, doi:org/10.1111/j.1365-246X.2008.03720.x.
- Lowry, DC 1970, Geology of the Western Australian part of the Eucla Basin: *Geological Survey of Western Australia, Bulletin 122*, 201p.
- Maier, WD, Smithies, RH, Spaggiari, CV, Barnes, SJ, Kirkland, CL, Kiddie, O and Roberts, MP 2016, The evolution of mafic and ultramafic rocks of the Mesoproterozoic Fraser Zone, Albany–Fraser Orogen, and implications for Ni–Cu sulfide potential of the region: *Geological Survey of Western Australia, Record 2016/8*, 49p.
- Meissner, R 1989, Rupture, creep, lamellae and crocodiles: happenings in the continental crust: *Terra Nova*, v. 1, no. 1, p. 17–28.
- Mjelde, R, Goncharov, A and Müller, RD 2013, The Moho: Boundary above upper mantle peridotites or lower crustal eclogites? A global review and new interpretations for passive margins: *Tectonophysics*, v. 609, p. 636–650, doi:org/10.1016/j.tecto.2012.03.001.
- Moore, VM and Wiltshko, DV 2004, Syncollisional delamination and tectonic wedge development in convergent orogens: *Tectonics*, v. 23, TC2005, 27p.
- Morrissey, LJ, Payne, JL, Hand, M, Clark, C, Taylor, R, Kirkland, CL and Kylander-Clark, A 2017, Linking the Windmill Islands, east Antarctica and the Albany–Fraser Orogen: Insights from U–Pb zircon geochronology and Hf isotopes: *Precambrian Research*, v. 293, p.131–149.
- Murdie, RE, Gessner, K, Occhipinti, SA, Spaggiari, CV and Brett, J 2014, Interpretation of gravity and magnetic data across the Albany–Fraser Orogen, in *Albany–Fraser Orogen seismic and magnetotelluric (MT) workshop 2014: extended abstracts* compiled by CV Spaggiari and IM Tyler: Geological Survey of Western Australia, Record 2014/6, p. 118–134.
- Myers, JS 1990, Precambrian tectonic evolution of part of Gondwana, southwestern Australia: *Geology*, v. 18, p. 537–540.
- Myers, JS 1993, Precambrian history of the West Australian Craton and adjacent orogens: *Annual Review of Earth and Planetary Sciences*, v. 21, p. 453–485.
- Myers, JS, Shaw, RD and Tyler, IM 1996, Tectonic evolution of Proterozoic Australia: *Tectonics*, v. 15, p. 1431–1446.
- Neumann, NL 2013, Yilgarn Craton – Officer Basin – Musgrave Province Seismic and MT Workshop: *Geoscience Australia, Record 2013/28*, 210p.
- Occhipinti, SA, Doyle, MG, Spaggiari, CV, Korsch, RJ, Cant, G, Martin, K, Kirkland, CL, Savage, J, Less, T, Bergin, L and Fox, L 2014, Interpretation of the deep seismic reflection line 12GA-T1: northeastern Albany–Fraser Orogen, in *Albany–Fraser Orogen seismic and magnetotelluric (MT) workshop 2014: extended abstracts* compiled by CV Spaggiari and IM Tyler: Geological Survey of Western Australia, Record 2014/6, p. 52–68.
- Occhipinti, SA, Tyler, IM, Spaggiari, CV, Korsch, R, Kirkland, CL, Smithies, RH, Martin, K and Wingate, MTD, 2017, Tropicana translated — a foreland thrust system imbricate fan setting for c. 2520 Ma orogenic gold mineralization at the northern margin of the Albany–Fraser Orogen, Western Australia, in *Characterization of Ore-Forming Systems from Geological, Geochemical and Geophysical Studies* edited by K Gessner, T Blenkinsop and P Sorjonen-Ward, Geological Society Special Publication 453, SP453.6.
- Oxburgh, ER 1972, Flake Tectonics and Continental Collision: *Nature*, v. 239, p. 202–204.
- Pearce, D, Rondenay, S, Sachpazi, M, Charalampakis, M and Royden, LH 2012, Seismic investigation of the transition from continental to oceanic subduction along the western Hellenic subduction Zone: *Journal of Geophysical Research*, v. 117, p. 1–18.
- Peterson, J 1993, Observations and modeling of seismic background noise: U.S. Geological Survey Open File Report, p. 93–322.
- Poudjom Djomani, YH, O'Reilly, SY, Griffin, WL and Morgan, P 2001, The density structure of subcontinental lithosphere through time: *Earth and Planetary Science Letters*, v. 184, no. 3, p. 605–621.
- Rawlinson, N and Sambridge, M 2004, Multiple reflection and transmission phases in complex layered media using a multistage fast marching method: *Geophysics*, v. 69 (11), p. 1338–1350, doi:org/10.1190/1.1801950.
- Rawlinson, N and Sambridge, M 2005, The fast marching method: an effective tool for tomographic imaging and tracking multiple phases in complex layered media: *Exploration Geophysics*, v. 36 (4), p. 341–350, doi:org/10.1071/EG05341.
- Reading, AM, Kennett, BLN and Dentith, MC 2003, Seismic structure of the Yilgarn Craton, Western Australia: *Australian Journal of Earth Sciences*, v. 50, p. 427–438.
- Reading, AM, Kennett, BLN and Goleby, B 2007, New constraints on the seismic structure of West Australia: evidence for terrane stabilization prior to assembly of an ancient continent: *Geology*, v. 35, p. 379–382.
- Salmon, M, Kennett, BLN and Saygin, E 2013, Australian Seismological Reference Model (AuSREM): crustal component: *Geophysical Journal International*, v. 192 (1), p. 190–206, doi:org/10.1093/gji/ggs004.
- Saygin, E and Kennett, BLN 2012, Crustal structure of Australia from ambient seismic noise tomography: *Journal of Geophysical Research*, v. 117 (B01304), 15p., doi:org/10.1029/2011JB008403.
- Scheib, A, Morris, P, Murdie, R and Delle Piane, C 2016, A passive seismic approach to estimating the thickness of sedimentary cover on the Nullarbor Plain, Western Australia: *Australian Journal of Earth Sciences*, v. 63 (5), p. 583–598, doi:org/10.1080/08120099.2016.1233455.
- Schneider, FM 2014, Imaging an intra-continental subduction in Central Asia with teleseismic receiver functions: Free University of Berlin, Berlin, PhD thesis (unpublished).
- Schneider, FM, Yuan, X, Schurr, B, Mechie, J, Sippl, C, Haberland, C, Minaev, V, Oimahmadov, I, Gadoev, M, Radjabov, N, Abdybachaev, U, Orunbaev, S and Negmatullaev, S 2013, Seismic imaging of subducting continental lower crust beneath the Pamir: *Earth and Planetary Science Letters*, v. 375, p. 101–112.
- Shapiro, NM and Campillo, M 2004, Emergence of broadband Rayleigh waves from correlations of the ambient seismic noise: *Geophysical Research Letters*, v. 31 (7), p. 8–11, doi:org/10.1029/2004GL019491.

- Shapiro, NM, Campillo, M, Stehly, L and Ritzwoller, M 2005, High-resolution surface-wave tomography from ambient seismic noise: *Science*, v. 307, p. 1615–1618, doi:org/10.1126/science.1108339.
- Sippl, C, Kennett, BLN, Tkalčić, H, Spaggiari, CV and Gessner, K 2015, New constraints on the current stress field and seismic velocity structure of the eastern Yilgarn Craton from mechanisms of local earthquakes: *Australian Journal of Earth Sciences*, v. 62 (8), p. 921–931.
- Smit, R 2009, 1st Annual Report and final surrender report, Kanandah Project, Eucla Basin, Western Australia, EL 28/1773; Buxton resources Limited: Geological Survey of Western Australia, Statutory mineral exploration report A081538 (unpublished).
- Smithies, RH, Spaggiari, CV, Kirkland, CL and Maier, WD 2014, Geochemistry and petrogenesis of igneous rocks in the Albany–Fraser Orogen, *in* Albany–Fraser Orogen seismic and magnetotelluric (MT) workshop 2014: extended abstracts *compiled by* CV Spaggiari and IM Tyler, Geological Survey of Western Australia, Record 2014/6, p. 77–88.
- Smithies, RH, Spaggiari, CV and Kirkland, CL, 2015, Building the crust of the Albany–Fraser Orogen; constraints from granite geochemistry: Geological Survey of Western Australia, Report 150, 49p.
- Snyder, DB and Goleby, BR 2016, Seismic reflection patterns associated with continental convergent margins through time: *Tectonophysics*, v. 192, p. 3–13.
- Spaggiari, CV 2016, Pre-Mesozoic 1:250 000 interpreted bedrock geology of the east Albany–Fraser Orogen: east Albany–Fraser Orogen, Geological Survey of Western Australia, Geological Exploration Package.
- Spaggiari, CV, Kirkland, CL, Smithies, RH, Occhipinti, SA and Wingate, MTD 2014a, Geological framework of the Albany–Fraser Orogen, *in* Albany–Fraser Orogen seismic and magnetotelluric (MT) workshop 2014: extended abstracts *compiled by* CV Spaggiari and IM Tyler: Geological Survey of Western Australia, Record 2014/6, p. 12–27.
- Spaggiari, CV, Kirkland, CL, Smithies, RH and Wingate, MTD 2014b, Tectonic links between Proterozoic sedimentary cycles, basin formation and magmatism in the Albany–Fraser Orogen, Western Australia: Geological Survey of Western Australia, Report 133, 63p.
- Spaggiari, CV, Kirkland, CL, Smithies, RH, Wingate, MTD, and Belousova, EA 2015, Transformation of an Archean craton margin during Proterozoic basin formation and magmatism: The Albany–Fraser Orogen, Western Australia: *Precambrian Research*, v. 266, p. 440–466.
- Spaggiari, CV, Occhipinti, SA, Korsch, RJ, Doublier, MP, Clark, DJ, Dentith, MC, Gessner, K, Doyle, MG, Tyler, IM, Kennet, BLN, Costelloe, RD, Fomin, T and Holzschuh, J 2014c, Interpretation of Albany–Fraser seismic lines 12GA-AF1, 12GA-AF2 and 12GA-AF3: implications for crustal architecture, *in* Albany–Fraser Orogen seismic and magnetotelluric (MT) workshop 2014: extended abstracts *compiled by* CV Spaggiari and IM Tyler: Geological Survey of Western Australia, Record 2014/6, p. 28–51.
- Spaggiari, CV and Smithies, RH (compilers) 2015, Eucla basement stratigraphic drilling results release workshop: extended abstracts: Geological Survey of Western Australia, Record 2015/10, 70p.
- Spaggiari, CV and Tyler, IM (compilers) 2014, Albany–Fraser Orogen seismic and magnetotelluric (MT) workshop 2014: extended abstracts: Geological Survey of Western Australia, Record 2014/6, 182p.
- Stephens, DI, 2000, Final Report for the Naretha Albany–Fraser project, Western Australia, EL 28/901–905; BHP Mineral Pty Ltd: Geological Survey of Western Australia, Statutory mineral exploration report A60607 (unpublished).
- Swager, CP, Goleby, BR, Drummond, BJ, Rattenbury, MS and Williams, PR 1997, Crustal structure of granite-greenstone terranes in the Eastern Goldfields, Yilgarn Craton, as revealed by seismic reflection profiling: *Precambrian Research*, v. 83, p. 43–56.
- Tassell, H and Goncharov, A 2006, Geophysical evidence for a deep crustal root beneath the Yilgarn Craton and Albany–Fraser Orogen, Western Australia, *in* Conference abstracts: Geological Society of Australia; Australian Earth Sciences Convention 2006, Melbourne, Victoria, 2 July 2006, 6p.
- Teixell, A 1998, Crustal structure and orogenic material budget in the west central Pyrenees: *Tectonics*, v. 17, p. 395–406.
- Tillick, D 2011, Final Report of Co-funded Government – Industry Drilling Program at the NSD Prospect, Eucla Project, August 2011; Teck Australia Pty Ltd: Geological Survey of Western Australia, Statutory mineral exploration report A091287 (unpublished), 14p.
- Tkalčić, H, Chen, Y, Liu, R, Zhibin, H, Sun, L and Chan, W 2011, Multistep modelling of teleseismic receiver functions combined with constraints from seismic tomography: Crustal structure beneath southeast China: *Geophysical Journal International*, v. 187 (1), p. 303–326, doi:org/10.1111/j.1365-246X.2011.05132.x.
- TRANSALP working group 2002, First deep seismic reflection images of the Eastern Alps reveal giant crustal wedges and transcrustal ramps: *Geophysical Research Letters* v. 29, p. 1–4.
- Vinnik, LP 1977, Detection of waves converted from P to SV in the mantle: *Physics of the Earth and Planetary Interiors*, v. 15 (1), p. 39–45, doi:org/10.1016/0031-9201(77)90008-5.
- Waddell, P-JA, Timms, NE, Spaggiari, CV, Kirkland, CL and Wingate, MTD 2015, Analysis of the Ragged Basin, Western Australia: insights into syn-orogenic basin evolution within the Albany–Fraser Orogen: *Precambrian Research*, v. 261, p. 166–187.
- Wittlinger, G, Farra, V, Hetényi, G, Vergne, J and Nábelek, J 2009, Seismic velocities in Southern Tibet lower crust: A receiver function approach for eclogite detection: *Geophysical Journal International*, v. 177, p. 1037–1049.
- Yao, H, Beghein, C and van der Hilst, R 2006, Surface wave array tomography in SE Tibet from ambient seismic noise and two-station analysis - II. Crustal and upper-mantle structure: *Geophysical Journal International*, v. 173 (1), p. 205–219, doi:org/10.1111/j.1365-246X.2007.03696.x.
- Yoshizawa, K 2014, Radially anisotropic 3-D shear wave structure of the Australian lithosphere and asthenosphere from multi-mode surface waves: *Physics of the Earth and Planetary Interiors*, v. 235, p. 33–48, doi:org/10.1016/j.pepi.2014.07.008.
- Young, MK, Rawlinson, N, Arroucau, P, Reading, AM and Tkalčić, H 2011, High-frequency ambient noise tomography of southeast Australia: New constraints on Tasmania's tectonic past: *Geophysical Research Letters*, v. 38 (13), p. 1–6, doi:org/10.1029/2011GL047971.
- Yuan, H 2015, Secular change in Archaean crust formation recorded in Western Australia: *Nature Geoscience*, v. 8, no. 10, p. 808–813.
- Zhang, S, Gao, R, Li, H, Hou, H, Wu, H, Li, Q, Yang, K, Li, C, Li, W, Zhang, J, Yang, T, Keller, GR and Liu, M 2014, Crustal structures revealed from a deep seismic reflection profile across the Solonker suture zone of the Central Asian Orogenic Belt, northern China: An integrated interpretation: *Tectonophysics*, v. 612–613, p. 26–39.
- Zhu, L and Kanamori, H 2000, Moho depth variation in southern California from teleseismic receiver functions: *Journal of Geophysical Research*, v. 105, p. 2969–2980.



## **Appendix**

**Synthetic tests and raypath coverage plots for ambient noise tomography**



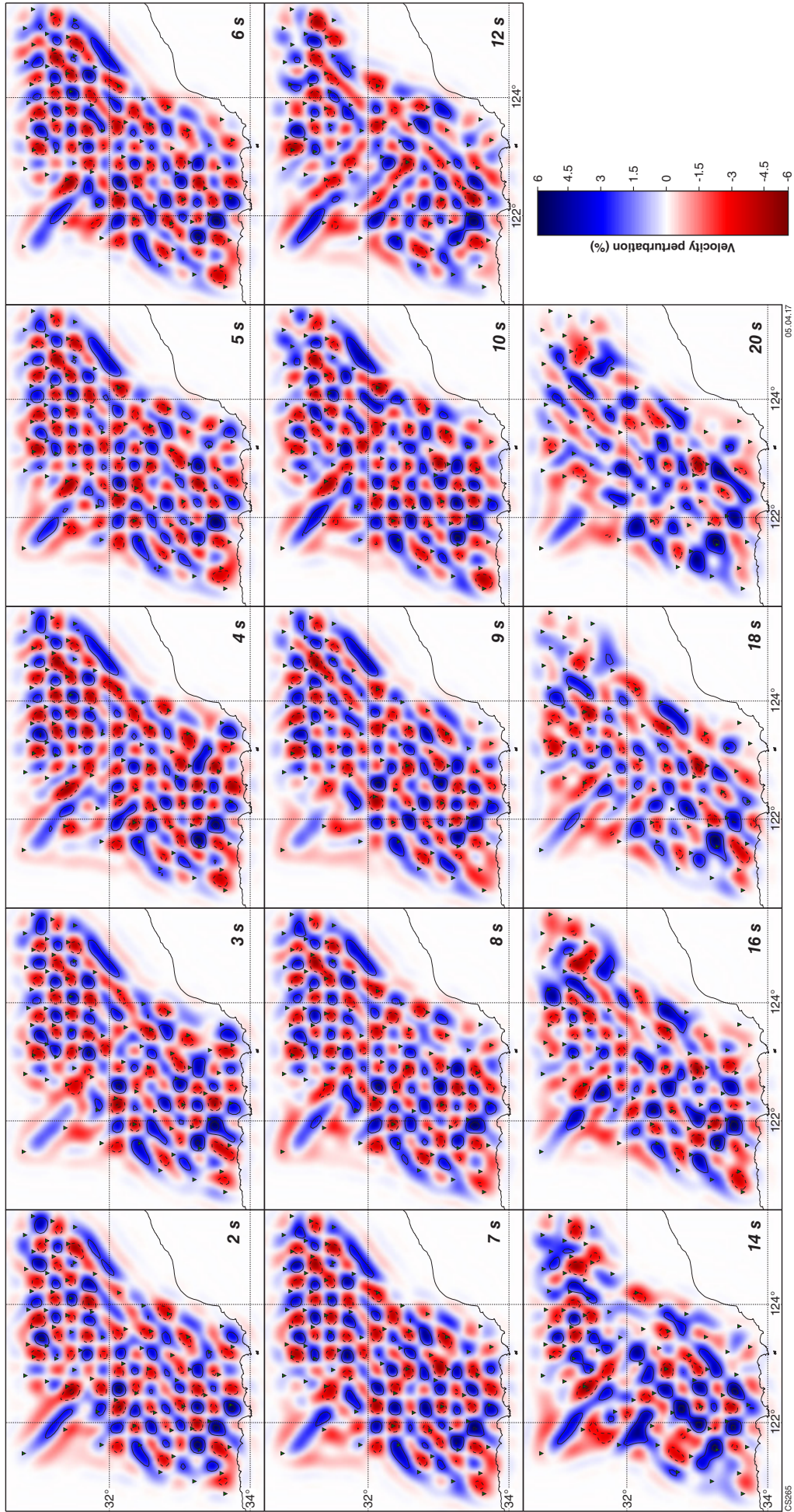


**Figure A1.** Output from synthetic checkerboard tests for group velocities, using the same event–station geometry and inversion parameters as for the real data. The input model featured alternating velocity anomalies of  $\pm 7.5\%$  at neighbouring grid vertices. Reconstructed models after inversion of synthetic travel-times are shown with Gaussian noise added (for details, refer to ‘Synthetic tests’ in the text). Contour intervals are  $\pm 2.5\%$



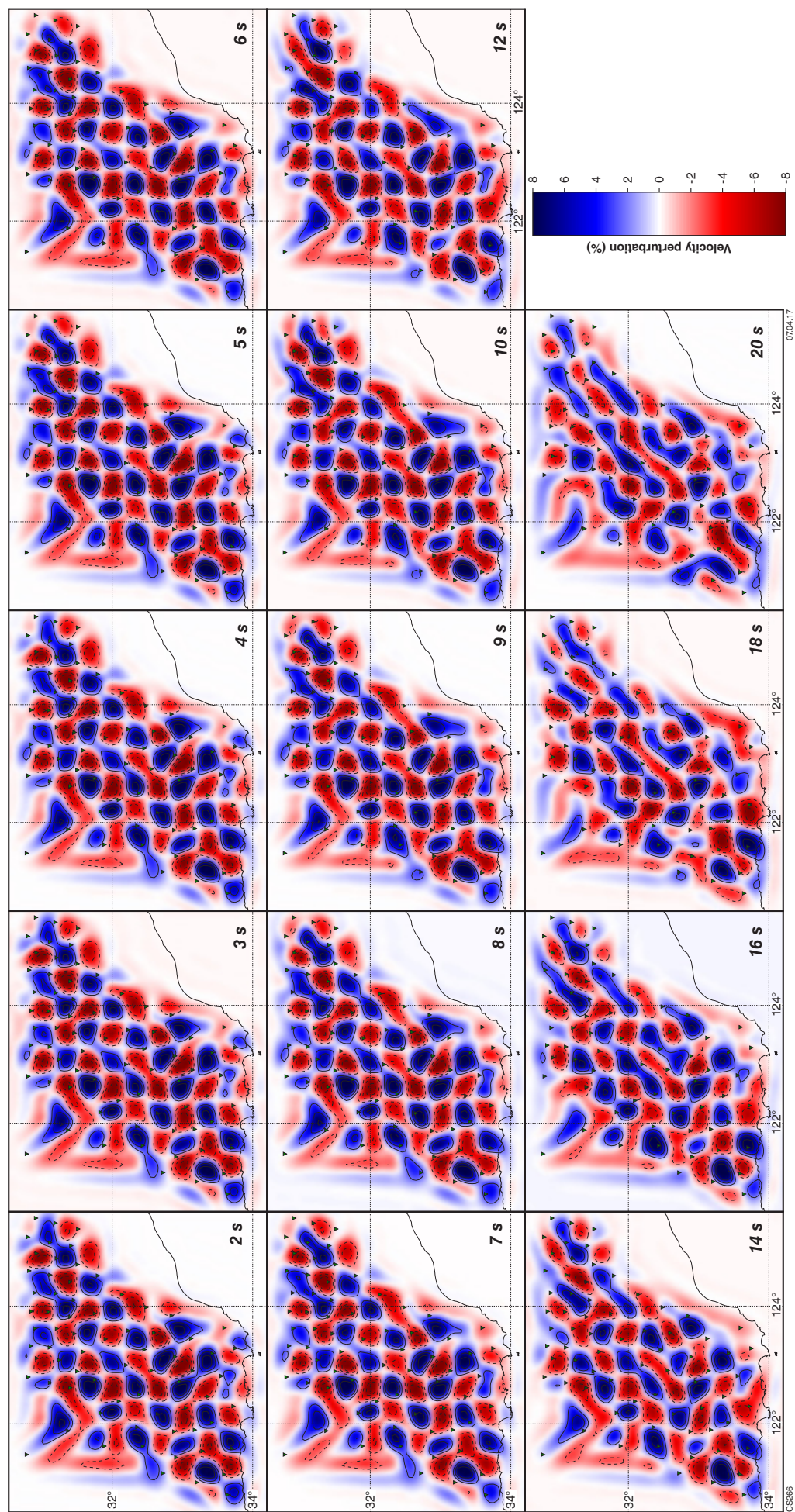
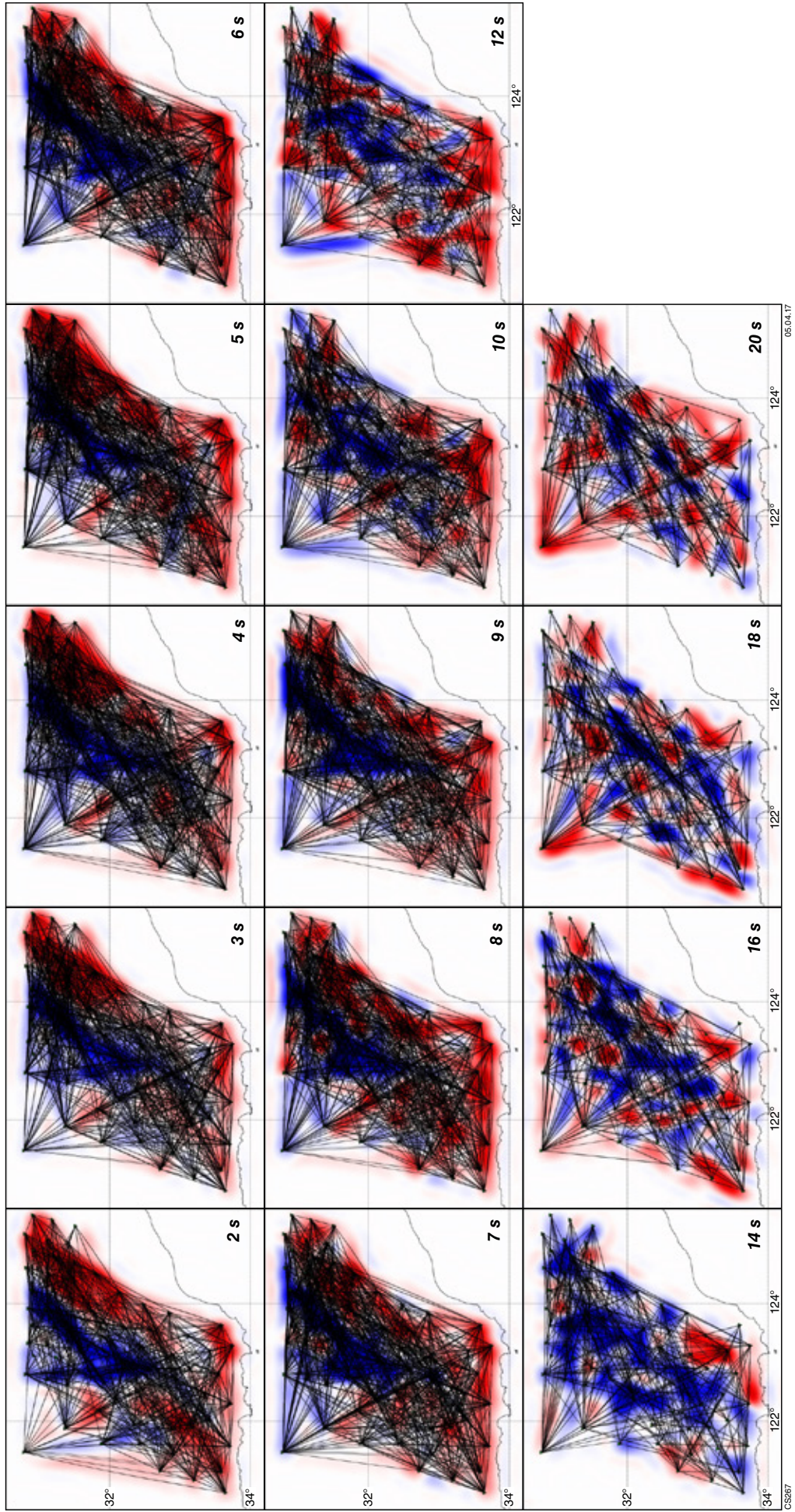


Figure A2. Output from synthetic checkerboard tests for phase velocities, using the same event–station geometry and inversion parameters as for the real data. The input model featured alternating velocity anomalies of  $\pm 7.5\%$  at neighbouring grid vertices. Reconstructed models after inversion of synthetic travel-times with Gaussian noise added (for details, refer to ‘Synthetic tests’ in the text). Contour intervals are  $\pm 2.5\%$





**Figure A3.** Raypath coverage for group velocity inversion for periods of 2–20 s. The obtained velocity models are shown in the background. Inverted green triangles represent seismic stations. Note that raypath density decreases significantly towards the longer periods (see also Fig. 16), which results in the observed diminished resolution (Fig. A1)



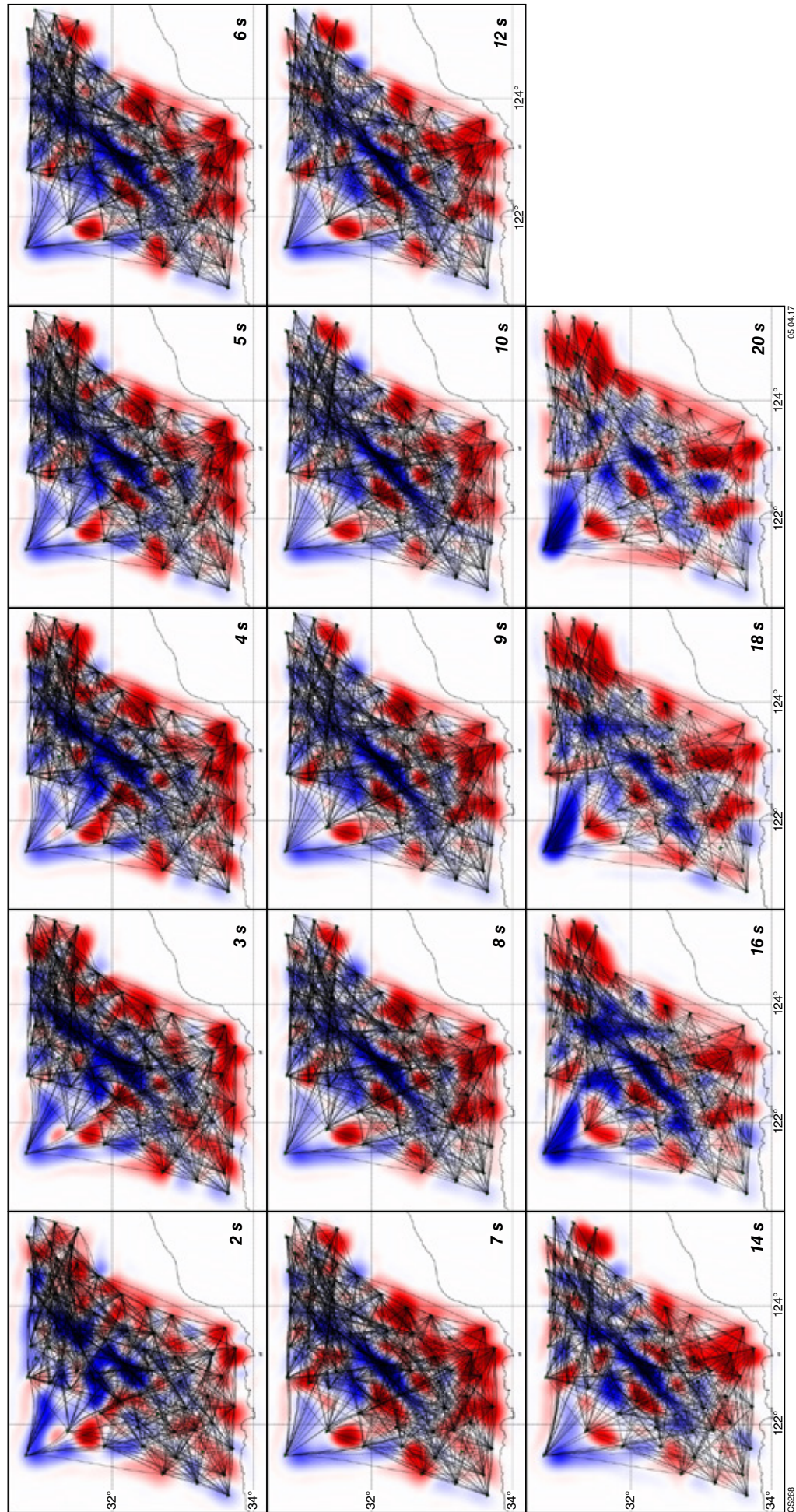
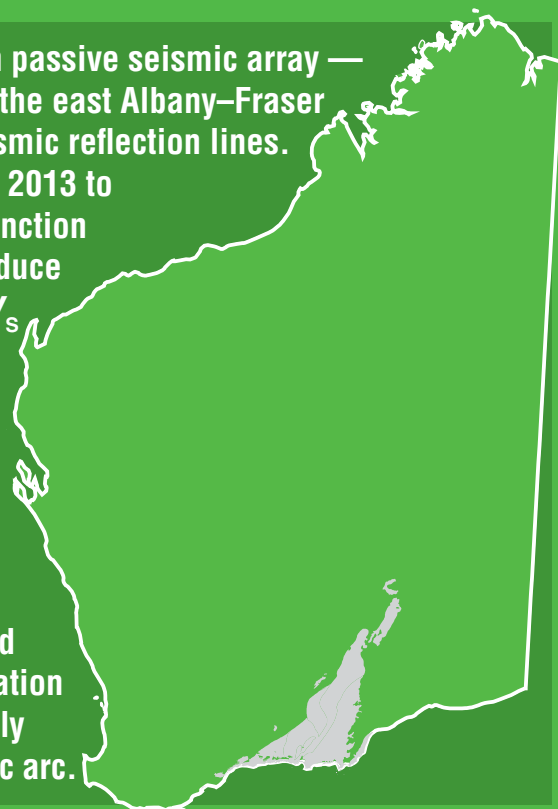


**Figure A4.** Raypath coverage for phase velocity inversion for periods of 2–20 s. The obtained velocity models are shown in the background. Inverted green triangles represent seismic stations. Note that raypath density decreases towards the longer periods (see also Fig. 16), which results in the observed diminished resolution (Fig. A2)



This Report presents the results of a 70-station passive seismic array — the ALFREX array — deployed in the region of the east Albany–Fraser Orogen previously covered by deep crustal seismic reflection lines. Passive seismic data recorded from November 2013 to January 2016 were evaluated using receiver function analysis and ambient noise tomography to produce maps of crustal thickness and bulk crustal  $V_P/V_S$  ratios, profiles of Moho geometry, and upper crustal surface-wave velocity maps. A belt of significantly thickened crust that follows the northeast trend of the east Albany–Fraser Orogen has been revealed. Gravity forward models were used to explain the presence of the Rason Regional Gravity Low and its relationship to this thickened crust. The imaged Moho structure may have resulted from indentation of a crustal wedge during compression, possibly related to the accretion of the Loongana oceanic arc.



Further details of geological products and maps produced by the Geological Survey of Western Australia are available from:

Information Centre  
Department of Mines and Petroleum  
100 Plain Street  
EAST PERTH WA 6004  
Phone: (08) 9222 3459 Fax: (08) 9222 3444  
[www.dmp.wa.gov.au/GSWApublications](http://www.dmp.wa.gov.au/GSWApublications)